High-repetition-rate Yb-doped lasers for frequency comb generation

Thomas Christian Schratwieser

Submitted for the degree of Doctor of Philosophy

Heriot-Watt University

Institute of Photonics and Quantum Sciences

12 May 2014

Abstract

The research presented in this thesis addresses the development of directly diode pumped Yb^{3+}:$KY(WO_4)_2$ and Yb:fibre lasers, operating at several-hundred-MHz repetition frequencies and investigates their suitability as the basis of high-efficiency, convenient, low-cost and moderate precision optical frequency combs.

The design, construction, and characterisation of a 1042-nm 1-GHz Yb^{3+}:$KY(WO_4)_2$ femtosecond laser is presented, achieving pulses with an average power output of 770 mW, bandwidths of 3.8 nm, and durations of 278 fs. The laser achieved an optical-to-optical conversion efficiency and slope efficiency of 61% and 69%, respectively, and the relative intensity noise was <0.1%. Spectral broadening of the output pulses in a photonic crystal fibre with a negative dispersion wavelength of 975 nm and a core diameter of 3.7 μm resulted in a supercontinuum with a bandwidth of 400 nm, which was insufficient to enable f-2f referencing.

A re-designed Yb:KYW laser was demonstrated, operating at a pulse repetition frequency of 666 MHz and producing pulses with reduced durations of 220 fs and increased bandwidths of 5 nm, while maintaining an average output power of >700 mW. Repetition-frequency locking was implemented on this laser and had the effect of reducing its relative intensity noise from 1.1% to 0.5%, with limitations on the locking stability being traced to cantilever-like vibrational modes of the mirror-mount assemblies.

A fully stabilised 1030-nm Yb:fibre frequency comb operating at a pulse repetition frequency of 375 MHz was developed. The comb spacing was referenced to a Rb-stabilised microwave synthesiser and the comb offset was stabilised by generating a supercontinuum containing a coherent component at 780.2 nm, which was heterodyned with a ^{87}Rb-stabilised external cavity diode laser to produce a radio-frequency beat used to actuate the carrier-envelope offset frequency of the Yb:fibre

laser. The two-sample frequency deviation of the locked comb was 235 kHz for an averaging time of 50 seconds, and the comb remained locked for over 60 minutes with a root mean squared deviation of 236 kHz.

For Mom and Dad, without whom I could not have started.

For Caroline, without whom I could not have finished.

Acknowledgements

This thesis is the culmination of three and a half years of work, and without the freely-given support of a great many friends and colleagues it would never have been possible. As I am given the opportunity at this point to opine regarding those who have guided me along the path I shall happily indulge.

Firstly, to say that Professor Derryck Reid helped me is to do him a disservice through understatement: I have never known of a mentor possessing more patience or intelligence. He has given me an astounding opportunity to pursue the advancement of physics, and it is a boon I can never truly repay.

I would like to thank Dr Christopher Leburn, whose boundless enthusiasm for optics and laboratory work proved to be infectious to the point of convincing me to engage in the very same. Your guidance and advice were invaluable.

To Dr Richard McCracken: thank you for listening when I was having trouble understanding a concept, for helping me when frustration due to an uncoöperative experiment got the better of me, and for the copy of *Cosmos*. I would similarly like to thank Dr Tobias Lamour for his welcoming attitude and his brilliant explanation of concepts. The time spent working together was a pleasure.

Thank you to Mark Stewart, Tony Aitken, and Peter Heron for guiding me through the design and creation of components.

To all of the other members of the Ultrafast Optics group past and present – Dr Zhaowei Zhang, Dr Jinghua Sun, Dr Carl Farrell, Dr Teresa Ferreiro, Cristtel Ramirez, and Karolis Balskus: thank you for your help, companionship, and for putting up with my sometimes inscrutable choices in music.

Lastly, thank you to my friends and family for listening to me prattle on about quantum corpuscules, and for perpetually standing by me. I love you all.

ACADEMIC REGISTRY
Research Thesis Submission

Name:	Thomas Christian Schratwieser		
School/PGI:	IPaQS		
Version: *(i.e. First, Resubmission, Final)*	Final	Degree Sought (Award **and** Subject area)	PhD Physics

Declaration

In accordance with the appropriate regulations I hereby submit my thesis and I declare that:

1) the thesis embodies the results of my own work and has been composed by myself
2) where appropriate, I have made acknowledgement of the work of others and have made reference to work carried out in collaboration with other persons
3) the thesis is the correct version of the thesis for submission and is the same version as any electronic versions submitted*.
4) my thesis for the award referred to, deposited in the Heriot-Watt University Library, should be made available for loan or photocopying and be available via the Institutional Repository, subject to such conditions as the Librarian may require
5) I understand that as a student of the University I am required to abide by the Regulations of the University and to conform to its discipline.

* *Please note that it is the responsibility of the candidate to ensure that the correct version of the thesis is submitted.*

Signature of Candidate:	TC Schratwieser	Date:	12 May 2014

Submission

Submitted By *(name in capitals):*	
Signature of Individual Submitting:	
Date Submitted:	

For Completion in the Student Service Centre (SSC)

Received in the SSC by *(name in capitals):*			
Method of Submission *(Handed in to SSC; posted through internal/external mail):*			
E-thesis Submitted ***(mandatory for final theses)***			
Signature:		Date:	

Please note this form should bound into the submitted thesis.

Updated February 2008, November 2008, February 2009, January 2011

Contents

1 Introduction **1**

1.1 Motivations and aim 1

1.2 Passive modelocking of solid-state laser systems 2

1.2.1 Mathematical treatment of passive modelocking 2

1.2.2 Semiconductor saturable absorber mirrors 6

1.3 Spectral broadening of laser spectra in a photonic crystal fibre 7

1.3.1 Mathematical description of spectral broadening by photonic crystal fibres 7

1.4 Femtosecond optical frequency comb stabilisation 11

1.5 Characterising femtosecond laser performance 13

1.5.1 Laser power 14

1.5.2 Spectral characteristics 14

1.5.3 Radio frequency measurements 15

1.5.4 Autocorrelation 15

1.5.5 Allan variance 17

1.6 Review of Ti:sapphire femtosecond optical frequency combs 18

1.7 Outline of the thesis 22

2 Design and characterisation of a solid-state 1-GHz Yb:KYW femtosecond laser **25**

2.1 Introduction 25

2.2 Material properties of Yb:KYW 25

2.2.1 Electronic properties of Yb^{3+} 25

2.2.2 Properties of KYW 27

2.2.3 Prior implementation of Yb:KYW in laser systems 30

2.3 Yb:KYW laser design 35
2.3.1 1-GHz cavity design 35
2.3.2 Optomechanical components used in construction 44
2.3.3 Modelocking elements in the 1-GHz cavity 47
2.4 Characteristics of the mode-locked 1-GHz cavity 49
2.5 Analysis of the laser stability 51
2.5.1 Noise measurement theory 51
2.5.2 Experimental work and discussion 53
2.6 Supercontinuum generation 54
2.7 Conclusions 55

3 Construction and repetition frequency stabilisation of a 666-MHz Yb:KYW femtosecond laser 57

3.1 Introduction 57
3.2 666-MHz Yb:KYW laser design 58
3.3 Characteristics of the 666-MHz cavity 59
3.4 Locking the repetition rate 61
3.4.1 Design of the locking apparatus 61
3.4.2 Integrating amplifier design 63
3.4.3 Repetition frequency locking 65
3.5 Conclusions 68

4 ^{87}Rb stabilisation of a 375-MHz Yb:fibre femtosecond frequency comb 70

4.1 Introduction 70
4.2 Review of fibre-laser frequency combs 71
4.3 Yb-doped fibre lasers 73
4.3.1 Properties of Yb:fibre 73
4.3.2 Modelocking methods 75
4.4 Yb:fibre laser design, construction, and performance 78
4.4.1 Cavity design 78

4.4.2 Characteristics of the Yb:fibre laser 80
4.5 Repetition rate stabilisation of the Yb:fibre laser 82
4.5.1 Locking loop design 82
4.5.2 Noise characteristics of the locked repetition rate 83
4.5.3 Conclusions 88
4.6 CEO stabilisation 88
4.6.1 ^{87}Rb-stabilised ECDL 89
4.6.2 Supercontinuum generation 93
4.6.3 Monochromator construction 96
4.6.4 Intracavity filter control of the carrier-envelope offset frequency 97
4.7 Noise characterisation of the fully-stabilised comb 101
4.8 Conclusions 102

5 Conclusions **104**

5.1 Experimental results and conclusions 104
5.2 Future developments for Yb^{3+}-doped laser systems 106

List of Tables

1.1 The essential results of different Ti:sapphire-based femtosecond systems and the year in which they were published. RPM indicates coupled-cavity resonant passive mode locking. IS, injection seeding. SML, synchronous mode locking. KLM, Kerr-lens modelocking. EOCD, electrooptic cavity dumping. 23

2.1 Crystallographic axes of Yb:KYW in both C2/c and I2/c space groups. 28

2.2 The Sellmeier indices of the different crystallooptic axes of Yb:KYW. 28

2.3 Summary of experiments involving Yb-doped tungstates prior to the start of the project. 36

3.1 The components, the distances between them, and necessary characteristics required for construction of the 666-MHz laser cavity. Labels refer to those seen in Figure 2.10. 60

4.1 Results of fibre comb experiments prior to start. "Fo8" refers to a figure of eight construction. 74

4.2 RMS deviation and Allan variance of Yb:fibre f_{rep} at differing observation times. 86

4.3 The characteristics of the assembled monochromator. 97

4.4 RMS deviation and Allan variance of comb-offset beat at differing observation times with the lock loop both on and off. 101

List of Figures

1.1 A schematic of the general form of a SESAM. A Bragg mirror is placed upon a substrate and atop that is a saturable absorber coated by a thin film. Pulses incident upon the absorber are shortened by virtue of the requirement of a saturation intensity of the leading edge before reflection is allowed, and the trailing edge can be truncated by the resumption of the absorption. 6

1.2 Above we see three consecutive pulses emitted by a mode-locked laser, whilst below we see the spectrum of such a system. The carrier-envelope phase shift from pulse to pulse is $\Delta\phi$ and arises from the fact that the pulse envelope travels with the group velocity and the carrier wave travels with the phase velocity. Were there no intracavity dispersion these would be equal. In the frequency domain this shift corresponds to $\omega_{CE} = \frac{\Delta\phi}{\tau}$ adding an offset to the whole of the comb. . 13

1.3 The schematic layout for an interferometric autocorrelation. The incoming light passes through a beam-splitting cube, one half is directed into the two arms of a Michelson interferometer. One arm is of variable length, but both are nearly identical. The resultant recombined beam is focussed through a lens on to a photodetector of a great enough bandgap to allow for two-photon absorption. 16

2.1 The Stark effect splitting of the $^2F_{7/2}$ and $^2F_{5/2}$ energy levels in cm^{-1} of Yb:KYW and Yb:KGW [50]. Pumping occurs from 0 cm^{-1} to 10695 cm^{-1} before non-radiative processes bring the excited level to 10187 cm^{-1} for emission between the $^2F_{5/2}$ state and the 407 $^2F_{7/2}$ state. 26

2.2 The orientation of the crystallographic axes of KYW, a, b, and c, compared to the optical axes, N_g, N_m, and N_p [52]. 29
2.3 The absorption spectra (a) and emission spectra (b) of Yb:KYW at room temperature [3]. 30
2.4 A diagram showing the inherent qualities of the Yb:KYW crystal used in this work. The crystal was 700-μm thick and Brewster-Brewster cut to allow for low insertion loss at one polarisation and with a longer path length through the material due to it being off-axis. 37
2.5 (a) Initial 4-mirror cavity design; (b) the modelled beam propagation in the designed cavity. The close matching of both the tangential and sagittal planes is seen. The mismatch at the smallest radius is due to passage through the Yb:KYW crystal, which is off-axis. Values are in mm. 38
2.6 The beam profile of the fibre-pigtailed laser diodes, determined through knife-edge measurements. The beam may look like the waist is deep within the fibre, itself, but that is because this model does not indicate the actual effect of the collimating lens, but was to find the complex beam parameter of the beam with the intent of discerning the propagation of light through the cavity. 39
2.7 (a) Layout of the pump lens, cavity mirror, and Brewster-cut Yb:KYW crystal. (b) CW propagation of one of the pump lasers through the lens (first vertical blue line), mirror (centre pair of blue vertical lines), and crystal (final pair of vertical blue lines). (c) propagation within the crystal (vertical blue lines). 40
2.8 (a) Layout of the pump lens, cavity mirror, and Brewster-cut Yb:KYW crystal. (b) CW propagation of one of the pump lasers through the lens (first vertical blue line), mirror (centre pair of blue vertical lines), and crystal (final pair of vertical blue lines). (c) propagation within the crystal (vertical blue lines). 41
2.9 The output power of pump lasers 1 (a) and 2 (b) with increasing current 42

2.10 The 1-GHz cavity design for cw operation. Laser diodes (LD) emit 981-nm light (represented by green) that passes through coupled fibres before making its way through collimating lenses (CL), half-wave plates ($\lambda/2$), focussing lenses (FL), and the cavity's folding mirrors (M1 and M2) before meeting in the crystal (X). Generated 1040 nm light is shown in red.One direction has the output coupler (OC) whilst in the other direction is a highly-reflecting end mirror. M1 has RoC = -20 mm; M2 has RoC = -30 mm; FL1 has a focal length of 30 mm; FL2 has a focal length of 40 mm. 43

2.11 A Rigrod analysis of the optimal output coupling of the Yb:KYW laser – a maximum is sought, which can be seen about 10% transmission – for 1274 mW in. This has been fitted from Equation 2.5 44

2.12 (a) is the power out of the Yb:KYW laser with the two pump diodes increasing in power one after the other, and (b) represents a simultaneous increase. 45

2.13 The copper-milled crystal mount made to gently hold the Yb:KYW crystal at Brewster's angle within the crystal. By utilising copper there was no need for extra temperature stabilisation or active cooling as there was ample volume for the amount of heat produced. 46

2.14 A close-up photo of the milled copper mount *in situ*. 46

2.15 (a) Top-down representation of the cw laser cavity of the same length as that of the mode-locked system with a folding mirror (by Christopher Leburn); (b) base plate for the system; (c) adapter to a 25 mm mount for 12.5 mm optics (off-axis to allow for more space); (d) mirror-holding arm for 6.5-mm optics; (e) holder for the pump lenses. 47

2.16 The 1-GHz cavity with all designed optomechanics assembled and mounted upon the breadboard. 48

2.17 The power transfer characteristic produced by the 1-GHz Yb:KYW laser. Mode-locked operation was achieved at powers to the right of the dashed line. The slope efficiency (solid red line) was 67%. 49

2.18 The output spectrum of the 1-GHz Yb:KYW laser centred at 1042 nm with a spectral width of 3.8 nm. 50
2.19 A fringe-resolved intensity autocorrelation of the Yb:KYW pulses. The full-width, half-maximum delay was 536 fs corresponding to 305 fs. 51
2.20 The RIN and cumulative standard deviation (the time-domain RMS noise) of the Yb:KYW laser for an 8-s observation time. The black and green lines represent data from one of the identical laser diodes while the red and blue lines represent the Yb:KYW output. 53
2.21 The predicted spectral (left) and temporal (right) broadening of the pulses from the 1-GHz Yb:KYW laser as they pass through a 3-m PCF. The extent of the broadening can be seen to form a supercontinuum from 800-1200 nm. 55
2.22 The experimentally recorded spectrum of the 1-GHz Yb:KYW laser broadened in a 3-m PCF 55

3.1 (a) Initial 4-mirror cavity design for 666 MHz; (b) the modelled beam propagation in the designed cavity. The close matching of both the tangential and sagittal planes is seen. The mismatch at the smallest radius is due to passage through the Yb:KYW crystal, which is off-axis. Values are in mm. 58
3.2 The design of the 666-MHz laser cavity, which was very similar to the 1-GHz laser in design. Laser diodes (LD) emit 981 nm light (represented by green) that passes through coupled fibres before passing through collimating lenses (CL), half-wave plates ($\lambda/2$), focussing lenses (FL), and the cavity's folding mirrors (M1 and M2) before meeting in the crystal (X) with a focussed spot size of 17 μm. At one end of the cavity the output coupler (OC) is situated; at the other end lies a semiconductor saturable absorber mirror (SESAM). 59
3.3 Spectrum of the 666-MHz cavity with a FWHM bandwidth of 5 nm. . 60

3.4 Fringe-resolved intensity autocorrelation of the 666-MHz cavity. Assuming $sech^2$ pulses the FWHM Yb:KYW laser pulse duration was 220 fs. 61

3.5 The schematic of the locked 666-MHz Yb:KYW system. A small portion of the laser light, 4%, was picked-off from the laser output and was incident on a fast photodiode. The signal passed through an amplifier and into a mixer with the output from a frequency synthesiser, which was, in turn, stabilised using the 10-MHz output from a Rb source. This then passed through a home-built amplifier (bounded by the dashed line), through an integrating amplifier, and further amplification before the signal was transmitted to the two PZTs controlling the linear position of both the GTI mirror and the SESAM. Pump diodes are not shown, for clarity. 63

3.6 Circuit diagram of the amplifier used to condition the repetition rate signal for locking. The system consisted of two inverting amplifiers, the first a fixed-gain amplifier with low-pass filtering (corner frequency of 25 kHz) and the second a variable gain amplifier. in the second of the two amplifiers the variable resistor orientated horizontally acted at the main gain whilst that orientated vertically was the DC offset. 64

3.7 The cumulative standard deviation (red) and relative intensity noise (blue) of the laser output over 320 seconds while the repetition-frequency-locking circuit was off. 65

3.8 The cumulative standard deviation (red) and relative intensity noise (blue) of the laser output over 320 seconds while the repetition-frequency-locking circuit was on. Immediate reduction of noise and error of the signal can be seen, though there are still substantial contributions to noise in the acoustic range. 66

3.9 The cantilever arms before (a) and after (b) damping. If a mass is placed at L/2 away from the ends of the cantilever this forces that point to be a node, which then means that the lowest normal mode of the system is one with a node at the free end of the cantilever, significantly reducing the amplitude. 67
3.10 The implementation of damping. A mass is circled in red. 67
3.11 The cumulative standard deviation (red) and relative intensity noise (blue) of the repetition-frequency-locked laser output over 320 seconds after damping of the cantilever mounts had been performed. There is an overall flattening of the noise profile and a removal of many of the noise spikes. The remaining noise spike could have been the resonance of the PZTs in the cavity. 68

4.1 The characteristics of absorption and emission in the Yb-doped fibre used in the experiment. Peak absorption and emission overlap, but with intracavity filtering the emission spectrum can be forced into lasing at 1040 nm. 76
4.2 An example of a SESAM mode-locked fibre laser taken from [116]. . . 77
4.3 An example of a NPE/ANDi mode-locked fibre laser taken from [117]. 78

4.4 The design of the 375-MHz Yb:fibre laser. Two fibre-pigtailed laser diodes (LD) emit pump light that passes into a polarisation combiner (PM) and through a collimator (CL). The light then passed through a pair of dichroic mirrors, which were highly transmitting at 976 nm and highly reflective at 1030 nm. The pump light then passed through a quarter-wave plate ($\lambda/4$) and into a collimator (CL2) which coupled it into the Yb:fibre (YDF) generating laser light. This generated light passed through another collimator (CL1) and through a quarter-wave and half-wave plate ($\lambda/4$ and $\lambda/2$) before interacting with a polarising beam-splitter cube (PBS). The accepted laser light then passed through an interference filter (IF), an optical isolator to ensure directionality (ISO), a curved mirror (M), and a further high reflector (HR) before arriving back at the dichroic mirror pair. 79

4.5 The optical spectrum from the mode-locked fibre laser with simultaneous interferometric autocorrelation (inset) [118]. This laser spectrum was much broader than that from the Yb:KYW laser, thereby allowing for better pulse compression. 81

4.6 A flowchart detailing the fitting procedure using a bespoke MatLab code. After making an initial guess as to the pulse's field amplitude in time the frequency-domain amplitude is calculated before replacing the guessed field intensity with the square root of the measured intensity. A GDD value is added and an inverse Fourier transform is performed on the resultant field amplitude. We now compute the interferometric autocorrelation and compare it to the measured autocorrelation. If they do not correspond, then a further GDD value is added to the calculated pulse and the loop runs again until the two are in agreement. 82

4.7 The sample GDD curves of Layertec GTIs at -250, -550, -1300, and -2000 fs^2 at wavelengths between 900 and 1060 nm. The green curve represents the characteristics of the mirrors used. 83

4.8 Left to right: Comparison of computed (blue) and measured (red) autocorrelations, the corresponding temporal pulse intensity, and the measured spectrum after the compressor for extracavity GDD of (a) -13000 fs^2; (b) -13600 fs^2; (c) -15600 fs^2; (d) -16200 fs^2; (e) -18200 fs^2; (f) -20800 fs^2; and (g) -21400 fs^2. 84

4.9 FWHM durations of the computed pulse profiles as the extracavity GDD was varied (symbols) and a cubic fit to the data (green line). Optimum compression is limited by 3^{rd}-order dispersion to ≈123 fs at a GDD of ≈ -18000 fs^2. 85

4.10 The interferometric autocorrelation from the laser after compression, corresponding to a pulse duration of 123 fs. Inset: the pulse profile [118]. This leads to a much higher peak power, but the lower pulse-repetition frequency will decrease the spacing of laser modes and the non-$sech^2$ profile would lead to problems with measurement of pulse durations. 85

4.11 The schematic of the rep-rate locked 375-MHz Yb:fibre system. 4% of the emitted light is redirected to a fast photodiode, the output of which is passed through a low-pass filter at 500 MHz and into a double-balanced mixer with the 375-MHz output from a 10-MHz Rb-stabilised frequency synthesiser. The heterodyne beat between the two is then amplified through an integrating amplifier, and the resultant signal is applied to a PZT in the cavity to change the cavity length. 86

4.12 The RMS deviation (dashed blue) and Allan variance (solid red) of the pulse repetition frequency with increasing observation times. . . . 87

4.13 The frequency fluctuations of the pulse repetition frequency relative to the mean with f_{rep} stabilisation turned on for averaging times of 50 s over a period of 83 minutes (100 samples). The RMS deviation was 12.4 mHz. 88

4.14 The design of the rubidium-locked external cavity diode laser. Light exits a laser diode operating at 780.2 nm and interacts with a diffraction grating in Littrow configuration. The 1^{st}-order light reenters the laser diode while the 0^{th}-order light passes through an optical isolator and a half-wave plate before reaching a 99:1 beamsplitter. 99% of the light passes through and is collimated into a SMF. The other 1% traverses a Rb-gas cell, through a 50:50 beamsplitter, and on to a photodiode. The signal from the photodiode has a DC-voltage applied to it and enters a double-balanced mixer with a 7.46 kHz signal from a frequency synthesiser, which is simultaneously sending the same signal to a summing amplifier. The combined RF signal exits the mixer, passes through a 153 Hz LPF, into an integrating amplifier, and subsequently into the same summing amplifier as before. A ramp signal and DC voltage are also applied to the summing amplifier, the output of which drives the PZT on the diffraction grating. 91

4.15 The absorption spectrum of Rb-gas. On the left-hand side are the contributions from ^{87}Rb and on the right hand side are those from ^{85}Rb. 92

4.16 The predicted spectral (left) and temporal (right) broadening of the pulses from the 375-MHz Yb:fibre laser as they pass through a 1.5-m PCF. The extent of the broadening can be seen to form a supercontinuum from 700-1450 nm. 94

4.17 The optical spectrum from the mode-locked fibre laser after passing through a 1.5-m PCF. The vertical blue line shows a peak at 696 nm and the red shows one at its harmonic: 1392 nm. [118]. 94

4.18 To improve the SNR of the direct comparison between comb modes near 780.2 nm and the ECDL reference a common-path arrangement through a PCF was built. Light from the Yb:fibre and SMF output of the ECDL were combined and collimated into a PCF, from which the light was directed onto a diffraction grating, through a lens to further spatially separate the modes, and onto an avalanche photodiode (APD). 95

4.19 (a)Yb:fibre laser spectrum after dispersion management; (b) supercontinuum generated by passage of Yb:fibre light through 1.5-m PCF; (c) spectrum of Rb-locked ECDL; (d) combined spectra of Yb:fibre laser and ECDL after combination in PCF showing no change to ECDL wavelength; (e) Combined and spectrally-filtered spectra of Yb:fibre laser and ECDL at the focal plane of the monochromator. All intensity scales are normalised and linear. 96

4.20 The heterodyne signal recorded with Yb:fibre laser rep-rate locked but without f_{CEO} stabilisation. The signal at 375 MHz is f_{rep} and those are 99 MHz and 276 MHz are the beats between the ECDL and spectrally-nearby Yb:fibre modes. Inset is the Fourier transform of the time-domain data sampled over 4.1 μs. 98

4.21 The beams from both the Yb:fibre laser and ECDL are made collinear, passed through a the PCF, and directed into the monochromator. The diffracted light is then imaged on to the active area of an avalanche photodetector. The signal is filtered and amplified before passing into an analogue-to-digital converter, into a PC for error control, and through a digital-to-analogue converter as output. It then passed through a summing amplifier with a DC-offset before passing through a further amplifier and driving the galvanometer motor. 99

4.22 A flowchart detailing the steps taken by the beat-control program implemented through MatLab. An acquired waveform had a Fourier transform performed, the frequency at which the peak of the RF spectrum resides was measured (P), and further compared against a pre-defined setpoint (SP) to create an error signal (E). The time since the beginning of control was then recorded (t) and a following derivation of the loop time (tloop) performed. The error signal was then conditioned according to PID control: a proportional term, an integral term (summing up the error terms since the beginning of the loop), and a derivative term (showing the change in error signal between loops) were combined into a final output voltage applied to the galvanometer motor controlling the intracavity filter. 100

4.23 The long-term stability of the CEO-beat signal in terms of frequency fluctuations with regard to its mean. f_{rep} was locked for both, and the comb-offset control was either off (blue) or on (green). The periodicity of the unlocked signal is likely to be caused by the temperature changes in the lab associated with the air-conditioning cycle. 101

4.24 The RMS deviation (blue) and Allan variance (red) of the comb-offset beat signal with stabilisation both off (open markers) and on (filled markers). The unlocked minimum at centre is a result of the rapid-scale jitter of the control method. All data were recorded as Yb:fibre laser was repetition-rate stabilised. 102

Publications

Journal articles

T. C. Schratwieser, C. G. Leburn, and D. T. Reid, "Highly efficient 1 GHz repetition-frequency femtosecond Yb^{3+}:$KY(WO_4)_2$laser," *Optics Letters*, vol. 37, pp. 1133-1135, Mar. 2012.

T. C. Schratwieser, K. Balskus, R. A. McCracken, C. Farrell, C. G. Leburn, Z. Zhang, T. P. Lamour, T. I. Ferreiro, A. Marandi, A. S. Arnold, and D. T. Reid, "^{87}Rb-stabilized 375-MHz Yb-fiber femtosecond frequency comb," *Optics Express*, vol. 22, pp. 10494-10499, May 2014.

Conference proceedings

T. C. Schratwieser, C. G. Leburn, and D. T. Reid, "Highly-efficient 1-GHz-repetition-frequency femtosecond Yb^{3+}:$KY(WO_4)_2$ laser for super-continuum generation," Presented at Ultrafast Phenomena 2012, Lausanne, Switzerland.

T. C. Schratwieser, C. G. Leburn, and D. T. Reid, "Highly-Efficient 1-GHz Repetition-Frequency Femtosecond Yb:KYW Laser for Supercontinuum Generation. Presented at Photon 12, Durham, United Kingdom.

1. Introduction

1.1. Motivations and aim

Femtosecond optical frequency combs have carved a very important place for themselves as high-precision laser sources for metrology and stable optical referencing [1]. These systems regularly have precisions on the order of 10^{-17} or 10^{-18}, but this is greater than that needed for many applications that stand to benefit from excellent accuracy. Furthermore, many of these comb systems are stabilised by external GPS references, which exhibit operational instabilities on the order of 10^{-11} for reasonable averaging times [2], a level well-suited for precise spectroscopy as well as length, time, and frequency measurement. High-pulse-repetition-frequency lasers are of a particular interest due to the improved resolution of these systems for spectroscopy due to an increased power per comb mode.

Yb^{3+}-doped gain media have proved to be interesting candidates for the creation of a new generation of optical frequency combs: using Yb^{3+}:$KY(WO_4)_2$ it is possible to build highly-efficient systems because of the inherent low quantum defect [3], and Yb^{3+}:fibre systems exhibit excellent stability and show promise for high-power systems which allow for a large number of applications, among them waveguide inscription and spectroscopy [4]. It is with these characteristics in mind that work to test the viability of Yb^{3+}-doped gain media for frequency comb generation was undertaken.

The work presented in this thesis was motivated by the desire to create high-pulse-repetition-frequency Yb^{3+}-doped laser sources possessed of short pulse durations in the interests of spectral broadening to generate a stable, locked, and referenced comb with an eye to future applications *in-situ* where a facility-based comb would be unsuitable due to its high cost and environmental sensitivity. Two Yb^{3+}:$KY(WO_4)_2$ systems were built, one operating at a pulse repetition frequency

of 1 GHz and the other at 666 MHz, and a Yb^{3+}:fibre system was investigated as a platform for stable femtosecond optical frequency comb creation.

1.2. Passive modelocking of solid-state laser systems

Passive modelocking techniques underpin most modern sources of ultrashort laser pulses [5–8] mainly due to the high efficiency of diode-pumped solid-state lasers and the effectiveness of saturable absorbers made with mature semiconductor growth techniques. This has also led to a surpassing of earlier limitations placed on solid-state lasers, which traditionally had to use flashlamps or active Q-switching to achieve prepulsing before pulse shortening via a saturable absorber could begin [9].

For the purpose of developing a mathematical understanding of passive modelocking we assume that there exists in the cavity a saturable absorber residing in the same plane as that of the gain medium. We then proceed to derive the variation in the pulse intensity and shape as it passes through this combined plane. In order for the pulse to be created the initial losses of the saturable absorber and intracavity losses must be greater than or equal to the gain at threshold, so that the pulse may see a net loss at the leading edge. The pulse must then have sufficient energy to saturate the absorber to transparency to drop below the initial gain level during the incursion of the leading edge whilst still having the power to saturate the laser gain material to reduce gain to that below the absorbency of the saturable absorber during the trailing edge.

In order for this to be a steady-state situation the gain must increase and absorption decrease to initial values during the round trip required to bring the laser pulse back to our absorption/gain plane; a difficult balance to achieve.

1.2.1. Mathematical treatment of passive modelocking

The intracavity pulse can be described as the field amplitude, as seen in Siegman's *Lasers* [10].

$$\epsilon(t) = Re\left[\tilde{E}(t)e^{i\omega_0 t}\right] \tag{1.1}$$

having a Fourier transform $\tilde{E}(\omega)$, meaning that $\tilde{E}(t)$ is the envelope of the pulse

(removing ω_0). We also describe $\tilde{E}(t)$ such that

$$I(t) = |\tilde{E}(t)|^2, \tag{1.2}$$

which is the instantaneous intensity travelling through the cavity.

Thus it is assumed that the transfer function for the round trip of the pulse can be approximated as

$$\tilde{E}'(\omega) = \tilde{E}(\omega) \times e^{-a_0 - i\frac{a_1}{\omega_c}(\omega-\omega_0) - \frac{1}{\omega_c^2}(\omega-\omega_0)^2} \tag{1.3}$$

in which a_0 is the cavity round trip loss coefficient. The second term, $-i\frac{a_1}{\omega_c}(\omega-\omega_c)$, is the linear dispersion or time-delay above and beyond τ. The final term, $\frac{1}{\omega_c^2}(\omega-\omega_0)^2$, is an approximation for bandwidth-limiting effects in the cavity and is not really tied to any one process but simply the cumulative effects of bandwidth limitation.

If the major limitation of the bandwidth of the laser is due to the gain material this final term simplifies to $-(4\alpha_m p_m/\Delta\omega_a^2) \times (\omega - \omega_a)^2$ wherein ω_a is the central angular frequency of the atomic gain profile and $\alpha_m p_m$ is the round-trip voltage gain coefficient. If the atomic linewidth, $\Delta\omega_a$ is very wide, then the final term can represent an etalon effect within the cavity and the final term may, instead, represent the peak transmission's variation.

Whatever the cause of these effects we can expect them to be small, and so Equation 1.3 simplifies accordingly:

$$\tilde{E}'\omega \approx \tilde{E}(\omega) \times \left[1 - a_0 - i\frac{a_1}{\omega_c}(\omega - \omega_0) - \frac{1}{\omega_c^2}(\omega - \omega_0)^2\right]. \tag{1.4}$$

We can replace $i\omega$ in the frequency domain with differentiation with respect to time through the Fourier transform. Additionally $-\omega^2$ becomes d^2/dt^2. We can further simplify the round trip change of the envelope to give:

$$\tilde{E}'(t) \approx \left[1 - a_0 - \frac{a_1}{\omega_c}\frac{d}{dt} + \frac{1}{\omega_c^2}\frac{d^2}{dt^2}\right]\tilde{E}(t), \tag{1.5}$$

which shows that the change in bandwidth is a second-order derivative, broadening the pulse in time.

As the saturable absorber in the cavity leads to time-dependent gain and loss, the gain, $g(t)$ is congruent to $\alpha_m(t)p_m$, where α_m is the laser gain and p_m is the path length through the gain medium. The loss from the saturable absorber is similarly structured ($q(t) \equiv \alpha_a(t)p_a$). If the contributions are less than a 20% change of the round trip, thereby small enough that the value of the exponential equation is near the value of the exponent, then these may be added to Equation 1.5 as

$$\tilde{E}'(t) = \left[1 + g(t) - q(t) - a_0 - \frac{a_1}{\omega_c}\frac{d}{dt} + \frac{1}{\omega_c^2}\frac{d^2}{dt^2}\right]\tilde{E}(t), \tag{1.6}$$

the net change in a single round trip.

In order to achieve a steady-state solution for cw mode-locked pulses the net change in the pulse envelope is thought of as a small time shift ($\partial T \ll \tau_p$, the pulse duration). In real terms this is indicating that the round-trip time of the pulse in the cavity may be different from the actual round-trip time of the cavity, but on the order of much less than a pulsewidth itself, due to contributions from the time-varying gain, $g(t)$, and time-varying loss, $q(t)$. This leads us to a steady-state solution that can be represented as follows:

$$\tilde{E}'(t) \approx \tilde{E}(t) + \frac{d\tilde{E}}{dt} \times \partial T, \tag{1.7}$$

and the steady-state is a solution of

$$\frac{1}{\omega_c^2}\frac{d^2\tilde{E}}{dt^2} - \left(\frac{a_1}{\omega_c} + \partial T\right)\frac{d\tilde{E}}{dt} + [g(t) - q(t) - a_0]\tilde{E}(t) = 0. \tag{1.8}$$

Here, $g(t)$ and $q(t)$ are produced by population differences $\Delta N_m(t)$ and $\Delta N_a(t)$, respectively, which follow the rate equations

$$\frac{dq(t)}{dt} = \frac{1}{T_1}\left[\frac{I(t)}{I_{sat}}q(t) - [q_1(t) - q_0]\right] \tag{1.9}$$

and

$$\frac{dg(t)}{dt} = \frac{1}{T_1}\left[\frac{I(t)}{I_{sat}}g(t) - [g_1(t) - g_0]\right] \tag{1.10}$$

where I_{sat} is the saturation intensity and the recovery time is T_1 to reach the original terms (g_0 and q_0). Depending on the speed of the saturable absorber we have one of two solutions. The first, for a fast absorber with a low saturation the loss is first-order:

$$q(t) \approx q_0 \left[1 - \frac{I(t)}{I_{sat}}\right] \tag{1.11}$$

if $\frac{I}{I_{sat}} \ll 1$. If, on the other hand, the absorber has a long recovery time, we get a solution of the form

$$\int_{q_0}^{q} \frac{1}{q}\frac{dq}{dt} = -\frac{1}{T_1 I_{sat}} \int_{\infty}^{t} I(t)dt \equiv -\frac{U(t)}{U_{sat}} \tag{1.12}$$

which, if the pulse energy U_p is expanded, generates

$$q(t) = q_0 e^{\frac{-U(t)}{U_{sat}}} \approx q_0 \left[1 - \frac{U_t}{U_{sat}} + \frac{1}{2}\left(\frac{U(t)}{U_{sat}}\right)^2\right]. \tag{1.13}$$

The equations for fast and slow saturable absorption in Equations 1.11, 1.12, and 1.13 are the same as those for fast and slow laser gain, and the solutions to the cavity equation (Equation 1.8) are those of a hyperbolic secant in terms of field either field amplitude or intensity

$$\tilde{E}(t) = E_0 \text{sech}\left(\frac{t}{\tau_p}\right) \tag{1.14}$$

and

$$I(t) = I_0 \text{sech}^2\left(\frac{t}{\tau_p}\right). \tag{1.15}$$

It should be noted that τ_p is not the full-width half-maximum pulsewidth for the hyperbolic secant squared, which can be obtained as $\tau_{FWHM} \approx 1.76 \times \tau_p$.

This description of a hyperbolic secant squared profile indicates soliton pulses, and will inform the descriptions of the pulse widths presented later on in characterisation of the constructed lasers.

1.2.2. Semiconductor saturable absorber mirrors

The method of passive modelocking used in this work was by saturable absorption though the implementation of a semiconductor saturable absorber mirror (SESAM). The pulses result from phase locking of supported laser modes in the cavity. A general SESAM, as demonstrated in Figure 1.1 consists of a Bragg mirror on a semiconductor substrate and is capped by a quantum well absorber coated by a thin film to select the incident wavelengths of light. The absorber becomes saturated by great intensities and becomes transparent, the built-up intensity of light propagating through the cavity is then free to reflect off of the Bragg reflector embedded in the material and again pass through the absorber before resuming its circulation.

Pulse shortening occurs as well in these devices. The leading edge of a pulse sees absorption greater than it can provide, and thus the reflection of the pulse can only begin after a certain amount of the pulse has already been absorbed by the SESAM. The trailing edge, similarly, can also be truncated should the device's recovery time be too short through the recovery of the SESAM's absorptive properties.

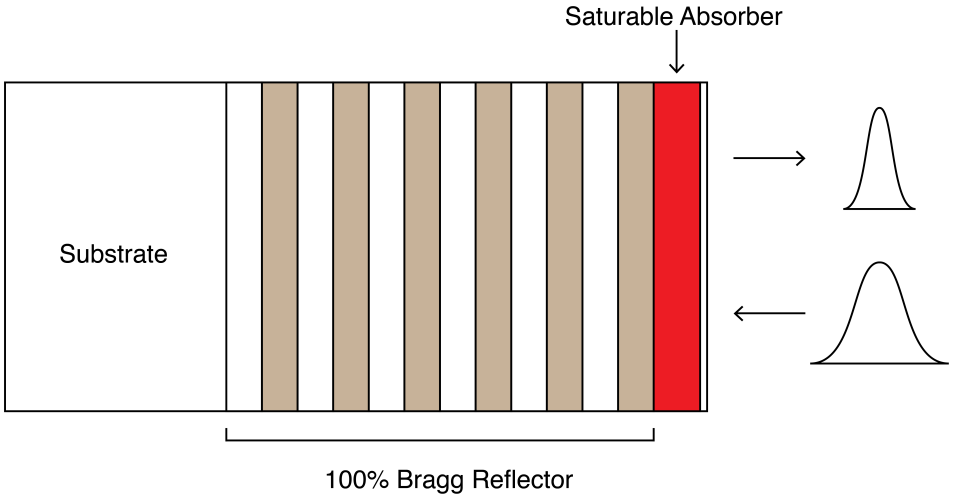

Figure 1.1: A schematic of the general form of a SESAM. A Bragg mirror is placed upon a substrate and atop that is a saturable absorber coated by a thin film. Pulses incident upon the absorber are shortened by virtue of the requirement of a saturation intensity of the leading edge before reflection is allowed, and the trailing edge can be truncated by the resumption of the absorption.

The material characteristics most important to understanding the use of a SESAM are the modulation depth, relaxation time, and saturation fluence. Modulation

depth indicates how great the change in reflectance of the device is, and increases as the relaxation time of the SESAM increases. The relaxation time should be longer than the pulse duration of the mode-locked laser to ensure greatest transmission of intensity. The saturation fluence is aptly named as it is the fluence at which the absorber is saturated and becomes transparent. The saturation fluence should be low so as to avoid damage to the absorber. To decrease saturation fluence the absorber must be thin, to increase saturation fluence more quantum wells must be added in more absorption layers to decrease the danger of destroying any single absorber at a time.

1.3. Spectral broadening of laser spectra in a photonic crystal fibre

Since early experiments on the nonlinear attributes of bulk laser gain media and fibre waveguides in the 1970s, when the first white-light supercontinua were generated for spectroscopic purposes, work on creating low-loss fibres and work towards the improvement of laser source power and pulse duration led to photonic crystal fibres (PCF) becoming the de-facto method for supercontinuum generation (important enough to be one of the technologies enabling the research of John Hall and Theodor Hänsch, who were awarded the 2005 Nobel Prize in Physics). They are also used extensively in comb generation within this work.

For this reason I include here a mathematical description of the spectral broadening in fibres by John Dudley and Roy Taylor [11].

1.3.1. Mathematical description of spectral broadening by photonic crystal fibres

We must first model a non-linear pulse to discuss its propagation through a medium: in order to do that Maxwell's equations must be amended with the nonlinear polarisation. These equations have been shown in both the time- and the frequency-domain – though the time-domain is preferred largely due to its direct analogy to a generalised nonlinear Schrödinger equation (GNLSE).

If the electric field (linearly polarised along $\mathbf{x}$) is defined as

$$\mathbf{E}(\mathbf{r},t) = \frac{1}{2}\mathbf{x}\left[E(x,y,z,t)e^{-i\omega_0 t} + c.c.\right], \tag{1.16}$$

then the Fourier transform in the frequency domain is

$$\tilde{E}(x,y,z,t) = F(x,y,\omega)\tilde{A}(z,\omega-\omega_0)e^{i\beta_0 z} \tag{1.17}$$

where $\tilde{A}(z,\omega)$ is the complex spectral envelope. ω_0 and β_0 are a selected angular reference frequency and wavenumber of that frequency, respectively. $F(x,y,\omega)$ is the transverse modal distribution. As $F(x,y,\omega)$ is non-dimensional the electric field, $E(x,y,z,t)$ must be scaled by a factor of $\sqrt{\frac{1}{2}\epsilon_0 cn}$ (where ϵ_0 is the vacuum permittivity, c is the speed of light, and n is the refractive index [12]). We then describe the time-domain pulse envelope using:

$$A(z,t) = \mathscr{F}^{-1}\left\{\tilde{A}(z,\omega-\omega_0)\right\} = \frac{1}{2\pi}\int_{-\infty}^{\infty}\tilde{A}(z,\omega-\omega_0)e^{-i(\omega-\omega_0)t}d\omega \tag{1.18}$$

by normalising the amplitude so $|A(z,t)|^2$ provides instantaneous power in Watts and $\mathscr{F}^{-1}$ is the inverse Fourier transform.

Now, by including the change of T, such that $T = t - \beta_1 z$, to transform the frame to one comoving at the group velocity of the pulse envelope, β_1^{-1}, we are able to find the GNLSE for $A(z,t)$:

$$\begin{aligned}\frac{\partial A}{\partial z} + \frac{\alpha}{2}2 - \sum_{k\geq 2}\frac{i^{k+1}}{k!}\beta_k\frac{\partial^k A}{\partial T^k} &= i\gamma\left(1 + i\tau_{shock}\frac{\partial}{\partial T}\right)\\ &\times\left(A(z,T)\int_{-\infty}^{\infty}R(T')|A(z,T-T')|^2 dT_1\right).\end{aligned} \tag{1.19}$$

The left-hand side of the equation deals with linear propagation effects in the fibre: α is the linear power attenuation and β_k represents all the β terms, which represent the dispersion coefficients associated with expansion of the propagation constant, $\beta(\omega)$, by Taylor series about ω_0. $\tilde{A}(z,\omega)$, the complex spectral envelope, can be multiplied through by the dispersion operator, $\tilde{\beta}(\omega)$, which is

$$\tilde{\beta}(\omega) = \beta(\omega) - (\omega-\omega_0)\beta_1 - \beta_0. \tag{1.20}$$

The right-hand side of Equation 1.19 is representative of non-linear effects where γ, the non-linear coefficient, is

$$\gamma = \frac{\omega_0 n_2(\omega_0)}{cA_{eff}(\omega_0)}. \tag{1.21}$$

In the nonlinear coefficient $n_2(\omega_0)$ is the non-linear refractive index and $A_{eff}(\omega_0)$ is the mode effective area (defined well in work by Lægsgaard [13]), both dependent on the reference frequency. Due to this dependence, ω_0 should be the centre frequency of the pulse to maintain the frequency-independent approximation. $R(t)$, then, is the Raman response function

$$R(t) = (1-\mathcal{F}_R)\delta(t) + \mathcal{F}_R h_R(t) = (1-\mathcal{F}_R)\delta(t) + \mathcal{F}_R \frac{\tau_1^2+\tau_2^2}{\tau_1\tau_2^2} e^{\frac{-t}{\tau_2}} \sin(\tfrac{t}{\tau_1})\Theta(t) \tag{1.22}$$

where $\mathcal{F}_R = 0.18$ is the fractional contribution of the delayed Raman response, $\tau_1 = 12.2$ fs, and $\tau_2 = 32$ fs. The variables $\Theta(t)$ and $\delta(t)$ are the Heaviside step function and Dirac delta function, respectively.

The polarisation from the Raman response is both parallel and orthogonal, though the orthogonal component is near-zero and, thus, is ignored. The time-dependent term on the right-hand side of Equation 1.19 is to describe the dispersion of the nonlinearity, usually in reference to optical shock formation (and the origin for τ_{shock}), and as propagation in fibre bears more nonlinearity than just that from optical shock the term τ_{shock} can be tailored to fulfil that function. An improvement on the time-domain method of including dispersion, however, is to work in the frequency domain:

$$\frac{\partial \tilde{A}'}{\partial z} = i\bar{\gamma}(\omega) e^{-\hat{L}(\omega)z} \mathscr{F}\left\{ \bar{A}(z,T) \int_{-\infty}^{\infty} R(T') |\bar{A}(z,T-T')|^2 dT' \right\} \tag{1.23}$$

and a, now frequency-dependent, nonlinear coefficient

$$\bar{\gamma}(\omega) = \frac{n_2 n_0 \omega}{c n_{eff}(\omega) A_{eff}^{\frac{1}{4}}(\omega)}, \tag{1.24}$$

which is of different units than those described earlier. The new spectral envelope is described as

$$\bar{A}(z,T) = \mathscr{F}^{-1}\left\{\frac{\tilde{A}(z,\omega)}{A_{eff}^{\frac{1}{4}}(\omega)}\right\}. \tag{1.25}$$

A change of variables is also a requirement due to the shift to the frequency-domain picture:

$$\tilde{A}'(z,\omega) = \tilde{A}(z,\omega)e^{-\hat{L}(\omega)z} \tag{1.26}$$

where $\hat{L}(\omega)$ is the linear operator, which, expanded, is:

$$\hat{L}(\omega) = i(\beta(\omega) - \beta(\omega_0) - \beta_1(\omega_0)[\omega - \omega_0]) - \frac{\alpha(\omega)}{2}. \tag{1.27}$$

In the preceding equations n_{eff} is the frequency-dependent effective index of the mode and n_0 is the linear refractive index used to determine n_2, the nonlinear refractive index. Frequency change is now obvious in this formulation, and this result means that we can now obtain:

$$\begin{aligned}\frac{\partial \tilde{C}}{\partial z} - i\tilde{\beta}(\omega)\tilde{C}(z,\omega) = i\frac{n_2 n_0 \omega}{c n_{eff}(\omega)\sqrt{A_{eff}(\omega)A_{eff}(\omega)}}\cdots \\ \mathscr{F}\left\{C(z.t)\int_{-\infty}^{\infty} R(T')|C(z,T-T')|^2 dT'\right\}\end{aligned} \tag{1.28}$$

using

$$\mathscr{F}\{C(z,t)\} = \tilde{C}(z,\omega) = \left[\frac{A_{eff}(\omega)}{A_{eff}(\omega_0)}\right]^{-\frac{1}{4}}\tilde{A}(z,\omega). \tag{1.29}$$

So we can now define a frequency-dependent nonlinear coefficient

$$\gamma(\omega) = \frac{n_2 n_0 \omega_0}{c n_{eff}(\omega)\sqrt{A_{eff}(\omega)A_{eff}(\omega_0)}}, \tag{1.30}$$

such that we may rewrite Equation 1.28 as:

$$\frac{\partial \tilde{C}}{\partial z} - i[\beta(\omega) - \beta(\omega_0)[\omega - \omega_0]]\tilde{C}(z,\omega) + \frac{\alpha(\omega)}{2}\tilde{C}(z,\omega)i\gamma(\omega)\left[1 + \frac{\omega - \omega_0}{\omega_0}\right]\ldots \\ \mathscr{F}\left\{C(z,t)\int_{-\infty}^{\infty} R(T')|C(z,T-T')|^2 dT'\right\}. \tag{1.31}$$

This is a useful form because of several reasons. First, the nonlinear coefficient, $\gamma(\omega)$ goes to its standard variation when neither n_{eff} nor A_{eff} are frequency-dependent. Second, if the frequency dependencies are ignored, if $\beta(\omega)$ is expanded as a Taylor series, and Equation 1.31 is inverse-Fourier transformed we go back to the original time-domain form seen in Equation 1.19.

These equations presented can be, and have been, used to accurately model the pulse dynamics in waveguides and fibre supercontinuum generation [14]. They are applied later in this thesis in the context of supercontinuum generated experimentally from Yb:KYW and Yb:fibre femtosecond lasers.

1.4. Femtosecond optical frequency comb stabilisation

There is a final treatment common to all systems developed herein that must be expounded: that of the conceptual basis of femtosecond optical frequency combs and their characteristics leading to our ability to stabilise and reference them, turning them into the accurate standards to which we are accustomed. I will use a treatment provided in *Ultrafast Nonlinear Optics* [15].

In the frequency domain we think of a train of pulses as a superposition of many longitudinal, intracavity modes, and it is these modes that create the Dirac delta function approximations that make up a comb. By phase-locking other lasers to these modes through heterodyne beating we can select these modes. The comb modes are also uniform in their spacing, such that the interval between them is a function of the pulse round-trip time, τ, in that

$$f_{rep} = \frac{1}{\tau}. \tag{1.32}$$

we see that a change in f_{rep} is due to a change in τ, and the shorter the round-trip

time the greater our repetition frequency.

The optical frequencies of the comb, described as f_n, are expressed as:

$$f_n = nf_{rep} + f_{CEO}, \tag{1.33}$$

though in this treatment we will, instead, be using the angular frequencies of the terms, leading to the expression

$$\omega_n = n\omega_r + \omega_{CE} \tag{1.34}$$

and because a periodic structure in the time domain is also periodic in frequency space the modes are separated by $\omega_r = \frac{2\pi}{\tau}$. In this case n is the mode number and is usually $\approx 10^5 \ldots 10^7$ with a zeroth-order mode that is arbitrarily chosen to allow the carrier-envelope offset ω_{CE} to lie between 0 and ω_r. This arises from the difference between the intracavity phase and group velocities, and offsets the comb modes by a constant value from 0 Hz.

If we assume that the pulses are perfectly time-shifted clones of one another and look at the electric field $E(t) = E(t - \tau)$, a Fourier transform yields a periodic structure in the spectrum with a separation of the modes equal to ω_r and no comb offset whatsoever. This is not what we find in a real case, though. Because of intracavity dispersion due to the pulse travelling through media, and not simply vacuum, the group and phase velocities are not equal, and this leads to the carrier wave of the pulse to shift with regards to the envelope, which can be seen in Figure 1.2. Consecutive pulses exiting the laser show a carrier-envelope phase shift of $\Delta\phi$.

For this analysis we can think of the pulse train as an optical carrier wave with phase velocity ω_c and with the pulse envelope function $A(t)$ as a modulation, travelling at the group velocity. Periodicity is retained by constraining $A(t)$ such that $A(t) = A(t - \tau)$. We can then express the pulse envelope in the frequency domain as a Fourier series:

$$E(t) = A(t)e^{-i\omega_c t} + c.c. = \sum_q A_q e^{-i(\omega_c + q\omega_r)t} + c.c., \tag{1.35}$$

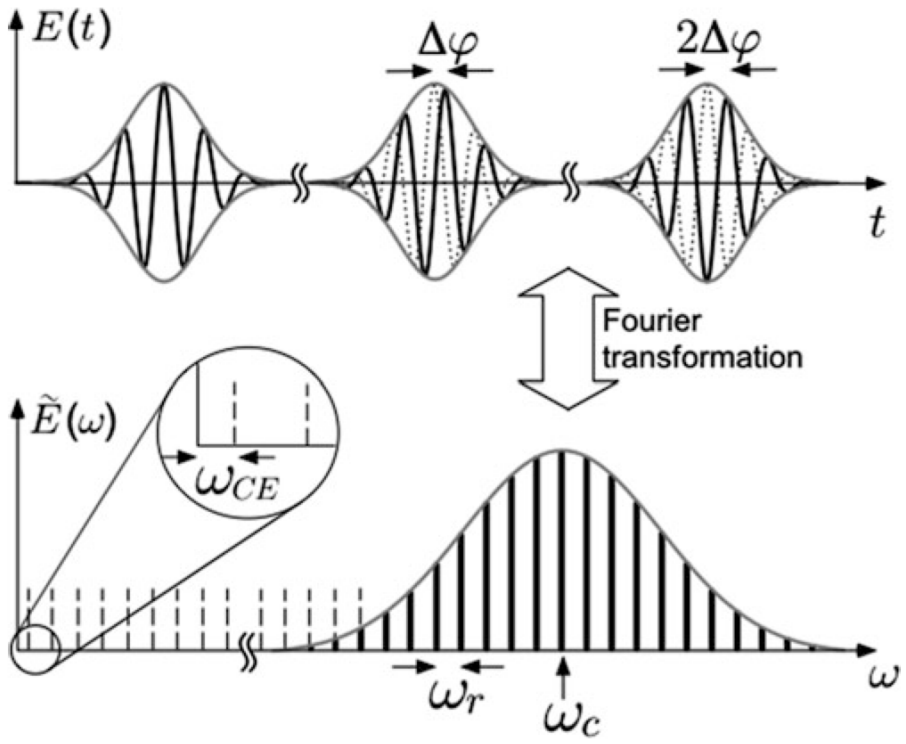

Figure 1.2: Above we see three consecutive pulses emitted by a mode-locked laser, whilst below we see the spectrum of such a system. The carrier-envelope phase shift from pulse to pulse is $\Delta\phi$ and arises from the fact that the pulse envelope travels with the group velocity and the carrier wave travels with the phase velocity. Were there no intracavity dispersion these would be equal. In the frequency domain this shift corresponds to $\omega_{CE} = \frac{\Delta\phi}{\tau}$ adding an offset to the whole of the comb. From [15].

where A_q are the Fourier components of $A(t)$. This represents a frequency comb with spacing ω_r and shifted from the ideal case. If the laser pulse is chirped we can create a complex $A(t)$ to account for this. Furthermore, as no system will be noise-free we must further alter Equation 1.35 to be a convolution of the carrier wave and pulse envelope spectra. If the carrier wave has a narrow linewidth and the pulse repetition frequency noise is low enough, thereby maintaining the comb structure, we can separate the individual modes. To stabilise the pulse repetition frequency we need only a small bandwidth of control ($\approx$ 100Hz) due to the upper-state lifetime of the specific gain material chosen while the carrier-envelope offset moves much more quickly and, thus, requires a much greater bandwidth.

1.5. Characterising femtosecond laser performance

It is not simply enough to design and build a comb: the system must have measurable characteristics to divine whether it is of suitable accuracy or not. In this section

I will cover the basics of what we expect from the laser power, the spectrum of a comb system, measurements of the radio-frequency components, and the basis of interferometric autocorrelation.

1.5.1. Laser power

Beyond the simple gratifying act of constructing a laser with a high average power, much in ultrafast optics, and certainly comb generation, hinges on the power characteristics of the laser source. Without high peak powers it is difficult, if not impossible, to sufficiently broaden the laser spectrum to a suitable bandwidth to allow for supercontinuum generation.

The peak power of a femtosecond pulse is dependent on the pulse shape, but if we assume sech^2 pulses (shown to be a common pulse shape in mode-locked lasers by Equation 1.14) we say that the peak power P_p is described as:

$$P_p \approx 0.88 \frac{E_p}{\tau_p} \tag{1.36}$$

where $E_p = \frac{E_{average}}{f_{rep}}$ is the pulse energy and τ_p is the FWHM pulse duration. If the pulse bears a Gaussian shape the conversion factor is ≈ 0.94, instead.

For approximate calculations this conversion factor can be entirely ignored, however, and the peak power can be simply though of as the pulse energy over the pulse repetition frequency.

1.5.2. Spectral characteristics

As one of the major features of a femtosecond optical frequency comb is its spectrum it is best to briefly touch upon spectral characterisation at this point. The bandwidth, or linewidth of a pulse is, if the laser is transform limited, a function of the pulse shape. This can be transmitted and broadened through four-wave mixing in nonlinear media. The definition used herein is the full width of the spectrum at half maximum and can be understood, as a relation between frequency and wavelength, as

$$\Delta\nu = \frac{c}{\lambda^2}\Delta\lambda. \tag{1.37}$$

Combined with a measurement of the pulse FWHM duration, the spectral bandwidth may be used to calculate a "duration-bandwidth product", $\Delta\nu\Delta\tau$, which takes a specific minimum value for a given pulse shape, and can therefore be used to diagnose the presence of chirp on a pulse. For $\mathrm{sech}^2(t)$ pulses, the minimum value is $\Delta\nu\Delta\tau = 0.315$, and for Gaussian pulses the value is 0.441.

1.5.3. Radio frequency measurements

The other present characteristics of the femtosecond optical frequency comb are the earlier-defined f_{rep} and f_{CEO}, the pulse repetition frequency and carrier-envelope offset frequency, respectively. The direct, and stable, control of the former is far more important to overall stability of the laser. As was seen earlier

$$f_n = nf_{rep} + f_{CEO}, \tag{1.38}$$

therefore the change in repetition rate of the laser multiplies out with the mode number (often multiplied by 10^7) and the carrier-envelope offset is only an additive term, regardless of the mode number.

The deviation of these frequencies is expressed in the time domain as a timing jitter.

1.5.4. Autocorrelation

In order to gain information about the duration of an ultrashort pulse – as well as any information regarding pulse chirp – fast photodiodes cannot be used below about 10 ps: a different method must be utilised: that of an autocorrelation. In this section I will be using the mathematics outlined in *Ultrafast Nonlinear Optics* [15] and by the references therein.

Autocorrelation is a method of superimposing copies of a laser pulse at various points of their envelope in order to assess the duration and phase information, but only if it is assumed that the pulse is describable by a function. If a Michelson interferometer with a variable arm length difference is constructed (a schematic of which is represented in Figure 1.3) the pulse of light self-interferes in the coupled cavity at varying points on its envelope. The photodetector placed after beam

recombination is one with a broad enough bandgap in order to avoid the necessity of using a nonlinear crystal.

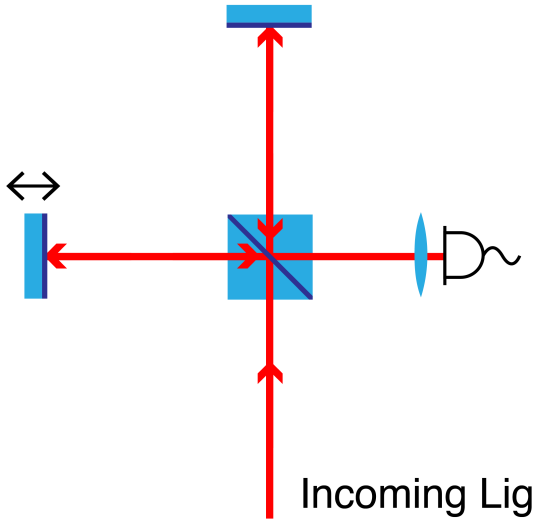

Figure 1.3: The schematic layout for an interferometric autocorrelation. The incoming light passes through a beam-splitting cube, one half is directed into the two arms of a Michelson interferometer. One arm is of variable length, but both are nearly identical. The resultant recombined beam is focussed through a lens on to a photodetector of a great enough bandgap to allow for two-photon absorption.

We record the average power of the two-photon signal

$$I_{ac}(\tau) = \int_{\infty}^{\infty} (E(t) + E(t+\tau))^4 dt \tag{1.39}$$

which gives an oscillation in delay with a frequency of c/λ. When the two pulses are perfectly constructively interfering ($\tau = 0$) the autocorrelation has 8 times the level at $\tau \to \pm\infty$. These systems are easy to construct, and, as they provide phase information, it is possible to diagnose chirp from such traces.

There are other methods, such as FROG [16] – in which the spectral information for thousands of delay settings are recorded – and SPIDER [17] – comparing two temporally-separated copies of a pulse with a third, highly-chirped clone. Both are very useful for pulses nearing the attosecond regime, but I will not go into detail regarding their operation here as they were not used in this thesis work.

1.5.5. Allan variance

When measuring the stability of an optical frequency reference it becomes necessary to measure its noise characteristics. The standard deviation is a useful diagnostic tool to discern the noise sources contributing to the instability of a laser source, but over long observation times the noise contributions lead to a logarithmic divergence and it was this in mind that David Allan of the National Bureau of Standards (NBS), now the National Institute of Standards and Technology (NIST), devised a two-point deviation method now known as Allan variance. In the interests of completeness I include his mathematical formulation. [18]

Beginning with an average angular frequency $\Omega_\tau(t)$ across the time interval τ is thought of as

$$\Omega_\tau(t) = \frac{1}{\tau}\left[\phi(t+\tau) - \phi(t)\right], \tag{1.40}$$

where ϕ is the phase angle represented in radians. If the variance of the frequency fluctuations is the square of the standard deviation σ, and the time average (denoted by $\langle\rangle$) of a function is

$$\langle f(t)\rangle = \lim_{T\to\infty}\frac{1}{T}\int_{T/2}^{T/2} f(t)dt, \tag{1.41}$$

the square of the standard deviation, and thus the variance, is

$$\sigma^2 = \langle\Omega_\tau(t)^2\rangle - \langle\Omega_\tau(t)\rangle^2. \tag{1.42}$$

The second term of Equation 1.42 can be set to zero, being the square of a time-averaged frequency, so $\Omega_\tau(t)$ is the frequency deviation from average, and $\phi(t)$ is the phase deviation. Substituting Equation 1.40 into Equation 1.42 nets

$$\sigma^2 = \frac{1}{\tau^2}\left[\langle\phi(t+\tau)^2\rangle - 2\langle\phi(t+\tau)\cdot\phi(t)\rangle + \langle\phi^2(t)\rangle\right] \tag{1.43}$$

where the time average $\phi(t+\tau)\cdot\phi(t)$ is the autocovariance – the measurement of how much the phase changes simultaneously as a time-shifted version of itself –

which can be substituted as $R_\phi(\tau)$. As the time-shifted phase should not affect the autocovariance, the square of the standard deviation becomes

$$\sigma^2 = \frac{2}{\tau^2}\left[R_\phi(0) - R_\phi(\tau)\right]. \tag{1.44}$$

This is the general case for an infinite series of acquisitions. Acquisitions are never infinite, however, so we must think of the squared standard deviation as a function of the number of acquisitions, N, the acquisition time, τ, and the total time of acquisition, T. The square of the frequency fluctuations becomes

$$\sigma^2(N,T,\tau) = \frac{1}{N-1} \left\{ \sum_{n=0}^{N-1} \left[\frac{\phi(nT+\tau) - \phi(nT)}{\tau} \right]^2 - \frac{1}{N} \left[\sum_{n=0}^{N-1} \frac{\phi(nT+\tau) - \phi(nT)}{\tau} \right]^2 \right\}. \tag{1.45}$$

This is the underpinning of the Allan variance. For a true Allan variance the "dead time" between acquisitions must be reduced to zero, but as the measurements made bore some dead time between them what was used was a "two-point variance".

1.6. Review of Ti:sapphire femtosecond optical frequency combs

Pulsed and continuous-wave Ti:sapphire lasers were first experimentally realised in the mid-eighties by Moulton *et al* (Schwarz Electro-optics) and Albers *et al* (Institut für Angewandte Physik in Hamburg), respectively [19, 20]. The crystal was found to bear an 80% quantum defect at room temperature as well as a broad tuning range ($\approx$ 700 to 1000 nm), properties that made it very attractive for spectroscopic applications. Early efforts in generating pulsed light through injection control by Brockman *et al* at the NASA Langley Research Centre in Virginia using a dye laser operating at 727 nm proved that injection-controlled Ti:sapphire lasers were capable of efficient wavelength generation without intracavity filtering [21]. Keller *et al* at Bell Labs in New Jersey demonstrated a passively mode-locked Ti:sapphire laser system using, instead of an internal saturable absorber element that would prove prone to damage at the high intracavity pulse powers endemic of the system, an

external cavity holding a quantum well within. The system showed tuning over a 50-nm bandwidth and the ability for harmonic generation. The pulse durations at this point were 2.1 ps [22].

Moving into the 1990s, Spence *et al* at the University of St Andrews generated 60 fs pulses from the first self mode-locked Ti:sapphire laser system, the self-modelocking method was eventually recognised as Kerr-lens modelocking (KLM). Utilising the intensity-dependent self-focussing of nonlinear media (a $\chi^{(3)}$ effect) one is able to create laser cavities that preferentially support high intensities, thereby encouraging only pulsed operation. The system generated 300 mW of average output power over a FWHM spectrum of 14 nm [23]. In the same year Spielmann *et al* at the Technische Universität Wien presented the generation of 70-fs pulses through simultaneous modelocking with an Nd:YLF laser [24], and Spence *et al* managed to further improve their Kerr-lens mode-locked system to be self-starting through the inclusion of an acoustooptic modulator (AOM) [25].

The term KLM came to be through a conference paper by Spinelli *et al*, and was expounded in a methods paper by Brabec *et al* simply titled *Kerr lens mode locking* [26].

Asaki *et al* at Washington State University presented work on a KLM laser achieving 11-fs pulses in 1993 [27], and the competition to achieve the shortest pulses possible continued from there. Pinto *et al* (Naval Research Labs, Washington, DC) realised higher average powers than had previously been possible due to improvements in crystal growth and doping techniques [28], and Stingl *et al* (Technische Universität Wien) achieved 8-fs pulses through mirror dispersion-control (using what are now referred to as Gires-Tournois interferometers, or GTIs) of a Ti:sapphire laser [29].

This is not to say that research on other mode-locking methods had stopped, though. Gibson *et al* at the University of Connecticut used Electrooptic cavity dumping to generate 20-fs pulses at a pulse repetition frequency of 1 kHz with exceptional peak pulse powers above 10 MW [30].

Kerr-lens modelocking did largely take over at this point, though: the promise of

self-starting, stable modelocking with pulse durations on the scale of femtoseconds was too much to ignore. Cho *et al* at the Massachusetts Institute of Technology generated 16.5-fs pulses from a 15-MHz repetition-rate KL mode-locked laser, leading to a system with very high peak powers: a very useful attribute for nonlinear experiments due to the high intensity achieved [31].

Further work by Udem *et al* at the Max-Planck-Institut in Garching in 1999 took the form of two papers: one enumerating the absolute optical frequency measurement of the caesium D_1 line through spectrally bridging the gap between the former and the fourth harmonic of a methane-stabilised He-Ne laser [32]; the second describing the method used for heterodyne action with unknown optical frequencies for measurement [33]. These two papers signalled the start of the serious use of Ti:sapphire femtosecond optical frequency combs for absolute optical frequency measurement.

In 2000 Diddams *et al* at the Joint Institute for Laboratory Astrophysics (JILA) at the University of Colorado began the practice of spectrally broadening the light from a KL mode-locked Ti:sapphire laser through self-phase modulation by coupling into an optical fibre. Their method achieved an almost 400-nm spectrum at a 90-MHz pulse repetition frequency [34]. This method, as well as the measurement of the carrier-envelope offset, was presented in an article in *Science* debuting their technique for $f - 2f$ detection of f_{CEO} [35]. $f - 2f$ detection is a method for the control of the carrier-envelope offset referenced in Figure 1.2. By frequency-doubling the lower-energy light of the comb at one end and collinearising it with its naturally-occurring second harmonic at the other end there is a heterodyne beat of f_{CEO}, which allows for its control.

Holzwarth *et al* at the Max-Planck-Institut presented their work on an optical-frequency synthesiser using the same methods later that year [36].

Work then progressed on improving the noise characteristics and phase coherence of these laser systems. Fortier *et al* at JILA demonstrated the construction of phase-coherence control of f_{CEO} to 150 s [37, 38]. Matos *et al* then presented an octave-spanning frequency comb directly from a Ti:sapphire laser, completely omitting the

fibre broadening by use of double-chirped mirror pairs and BaF_2 wedges to control intracavity dispersion. This brought with it improvements in long-term stability and simplicity [39].

In 2005 John Hall and Theodor Hänsch won one half of the Nobel Prize in Physics "for their contributions to the development of laser-based precision spectroscopy, including the optical frequency comb technique" [1,40], the other half being awarded to Roy Glauber for his early work on the quantum theory of optical coherence.

In 2006 Fortier *et al*, now at Los Alamos, presented work on kHz-resolution spectroscopy of atoms using the frequency comb technique, demonstrating the potential for high-resolution absolute-frequency spectroscopy [40]. Experiments on providing high-power, low repetition-rate Ti:sapphire sources also continued. Matsushima *et al* presented their work on a 40-W Ti:sapphire ring amplifier at 10 kHz to replace earlier YAG sources for excited photoelection spectroscopy (EUPS) [41].

One major limitation of Ti:sapphire as a frequency comb source, however, is its residence firmly in the visible spectrum ($f - 2f$ commonly being 532-1064 nm), and so, in 2007, Sun *et al* at Heriot-Watt University presented their work on comb creation between two coresonant optical parametric oscillators (OPOs) [42] and coherent synthesis of a Ti:sapphire femtosecond optical frequency comb with an OPO to extend the useable range of Ti:sapphire frequency combs from 0.4 μm to 2.4 μm [43].

A second limitation of Ti:sapphire comb systems was the long cavity lengths necessary for the short pulse durations: the longer cavity lengths led to low pulse repetition frequencies, therefore the comb mode spacing was narrow. In order to improve the resolution of these systems high-repetition-rate lasers needed to be built. Bartels *et al* at Gigaoptics GmbH created a spectrally-resolved optical frequency comb using a 5-GHz laser [44]. Noguiera *et al* presented their 2.12-GHz system the following year with pulses compressed to 5.9 fs using multiphoton intrapulse interference phase scanning (MIIPS), a method of simultaneously measuring and corrects the phase of the pulses using an adaptive pulse shaper: greatly reducing the higher-order dispersion of the pulse and allowing for shorter pulses than would

otherwise be possible [45].

Bartels *et al* took the push for high repetition rates even further with a 10-GHz mode-locked Ti:sapphire system emitting 42-fs pulses. By referencing this system to rubidium vapour they were able to measure the carrier-envelope offset of the comb [46]. The following year Roth *et al* at Strathclyde University exhibited a directly diode-pumped Ti:sapphire laser, implying a future for portable systems. Using a GaN diode they were able to extract 19 mW of cw power [47]. Further work led to a passively mode-locked form with 114-fs pulses operating at 127 MHz and emitting 13 mW [48].

Since their realisation Ti:sapphire lasers have passed through many different iterations, from early injection-seeded lasers to the passively mode-locked KLM systems the lasers have become more and more advanced and more useful for a variety of applications. Despite this, Ti:sapphire systems still have some limitations: the bandwidth is unsuited for infrared spectroscopy and suitable laser diodes for highly-efficient direct diode pumping have not yet been developed (thereby increasing the size of powerful systems considerably, even at high repetition rates), thus a new dopant and host were needed to fill this void. Yb^{3+}:$KY(WO_4)_2$ and Yb^{3+}:fibre, with their central emission near 1 μm and an absorption peak near 980 nm – a wavelength with many commercially-available laser diodes – therefore represented compelling gain materials for further study.

A collection of these essential results can be seen in Table 1.1.

1.7. Outline of the thesis

The remainder of this thesis presents the design, construction, and results from multiple Yb^{3+}-doped laser sources and the pursuit of performance suitable for frequency comb generation. Several systems were developed in trying to reach this goal: a 1-GHz Yb^{3+}:$KY(WO_4)_2$ SESAM-mode-locked laser, a 666-MHz Yb^{3+}:$KY(WO_4)_2$ SESAM-mode-locked laser, and a 375-MHz Yb^{3+}:fibre laser originally constructed by Carl Farrell, with the final proving to be the most suitable for frequency comb generation. The pulse repetition frequency was stabilised, and, by spectrally broadening the output of the Yb:fibre laser with a PCF, the carrier-envelope offset was

Reference	Year	P_{out}	τ_p	Mod. effect	λ	f_{rep}
[19]	1986	150 mW	N/A	Pump	N/A	N/A
[20]	1986	N/A	N/A	N/A	715-825 nm	N/A
[21]	1986	N/A	N/A	Pump	727 nm	N/A
[22]	1990	90 mW	5 ps	RPM	860 nm	250 MHz
[23]	1991	300 mW	60 fs	KLM	873-887 nm	N/A
[24]	1991	200 mW	72 fs	SML	750-760 nm	76 MHz
[25]	1991	600 mW	60 fs	KLM	836-846 nm	86 MHz
[27]	1993	500 mW	11 fs	KLM	749-811 nm	N/A
[28]	1994	3.5 W	N/A	N/A	N/A	N/A
[29]	1995	60-100 mW	8 fs	KLM	775-880 nm	80 MHz
[30]	1996	150 mW	20 fs	EOCD	770-830 nm	1 kHz
[31]	1999	0.7 mW	16.7 fs	KLM	780-822 nm	15 MHz
[34]	2000	120 mW	N/A	KLM	778-1064 nm	90 MHz
[37]	2002	N/A	10 fs	KLM	532-1064 nm	N/A
[39]	2004	N/A	N/A	KLM	532-1064 nm	150 MHz
[41]	2006	40 W	58 fs	KLM	N/A	10 kHz
[43]	2007	$>$ 2mW	50 fs	KLM	1.2-1.37 μm	200 MHz
[44]	2007	1.15 W	24 fs	KLM	532-1064 nm	5 GHz
[45]	2008	0.95 W	5.9 fs	KLM	650-1040 nm	2.12 GHz
[46]	2008	$>$ 1 W	42 fs	KLM	783-793 nm	10 GHz
[47]	2009	19 mW	N/A	N/A	795 nm	N/A
[48]	2011	13 mW	114 fs	KLM	838-845 nm	127 MHz

Table 1.1: The essential results of different Ti:sapphire-based femtosecond systems and the year in which they were published. RPM indicates coupled-cavity resonant passive mode locking. IS, injection seeding. SML, synchronous mode locking. KLM, Kerr-lens modelocking. EOCD, electrooptic cavity dumping.

stabilised and referenced to an ^{87}Rb-locked external cavity diode laser (ECDL). Noise measurements were performed and the system was shown to be reliably locked.

In the present chapter I have outlined many of the theoretical concepts that are necessary to explain and interpret the operation of the systems which will be described later, as well as laying the groundwork for the design and construction of these mode-locked laser sources.

Chapter 2 details the design, construction, and characterisation of a 1-GHz Yb^{3+}:$KY(WO_4)_2$ femtosecond laser. The properties of the Yb^{3+} ion and the $KY(WO_4)_2$ host material are elucidated and a review of Yb^{3+}:$KY(WO_4)_2$ femtosecond systems is presented. The characteristics of the constituent parts of the laser are also presented. The laser's power, spectrum, pulse duration, and noise characteristics are discussed, along with spectral broadening results and analysis.

Chapter 3 presents a redesigned Yb:KYW laser including approaches to lengthen the cavity, and thus lower the pulse repetition frequency of the system to 666 MHz, in order to achieve higher peak pulse powers and a broader spectrum. The pulse repetition frequency of the laser was locked – the design of the system presented – and noise measurements performed. The relevant data are presented as well as the rationale to move towards a Yb^{3+}:fibre system.

Chapter 4 describes the move to the 375-MHz Yb^{3+}:fibre laser. A review of Er^{3+}- and Yb^{3+}-doped fibre systems is presented and the design of the system is shown. The laser's characteristics are enumerated and the implementation of the pulse repetition frequency locking is detailed. Experiments in spectral broadening are presented, and a description of the ^{87}Rb-locked ECDL is included. The work to reference the Yb^{3+}:fibre laser to our ECDL-reference and relevant data are presented.

Chapter 5 covers the main conclusions from the presented work and presents a discussion on the viability of Yb^{3+}-doped lasers for future supercontinuum generation. Improvements to the current state of the work and future experiments are proposed.

2. Design and characterisation of a solid-state 1-GHz Yb:KYW femtosecond laser

2.1. Introduction

In this chapter I present the work to design and build a 1-GHz Yb^{3+}:$KY(WO_4)_2$ (Yb:KYW) femtosecond laser, as well as the further efforts to produce a stable femtosecond optical frequency comb from that system. I start by covering the properties of both Ytterbium and the tungstates ($KY(WO_4)_2$ mainly, but also $KGd(WO_4)_2$ in contrast) to show their usefulness in the system before moving on to the design of the laser cavity and constituent optomechanics. From that point I discuss the construction and characterisation of the laser, itself.

Once the laser had been built the system was characterised to determine the pulse duration, repetition rate, power output, and spectrum. These measurements are presented, as well as an analysis and discussion of the suitability of the system for high-accuracy measurement informed by relative intensity noise (RIN) measurements of the laser output.

2.2. Material properties of Yb:KYW

Ytterbium-doped tungstates have achieved great success in recent years – mainly due to their efficiency, simple heat transfer, and ease of matching of the pump wavelength to the absorption band of ytterbium. From a family of double tungstates (containing two tungstate terms) of the form $A^I T^{III}(WO_4)_2$ – A is a monovalent alkali-metal cation and T is trivalent metal or rare-earth cation – KYW's crystal structure is similar to the well-known Scheelite ($CaWO_4$) [49].

2.2.1. Electronic properties of Yb^{3+}

The trivalent ytterbium ion is a quasi-three-level gain medium – meaning it is four-level, but exhibits qualities similar to a three-level medium – wherein the lower laser energy level and ground state are very close to one another. This means that

there is a population inhabiting the lower laser level at thermal equilibrium and the gain medium only becomes transparent when a threshold population inversion is achieved; otherwise there will be significant reabsorption losses.

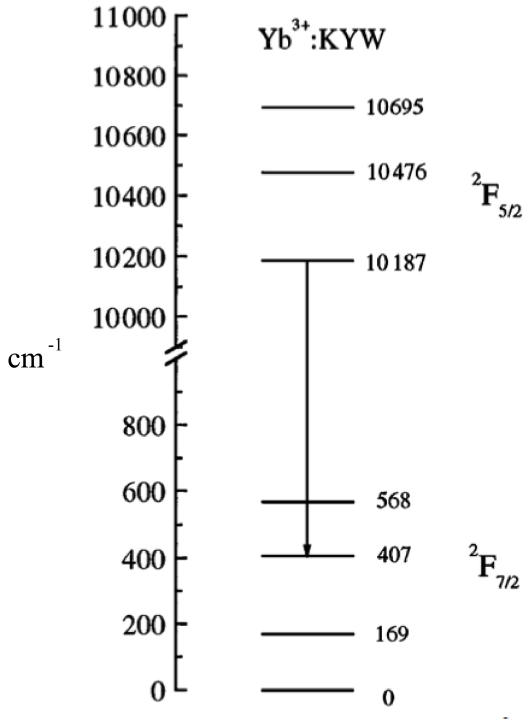

Figure 2.1: The Stark effect splitting of the ${}^2F_{7/2}$ and ${}^2F_{5/2}$ energy levels in cm^{-1} of Yb:KYW and Yb:KGW [50]. Pumping occurs from 0 cm^{-1} to 10695 cm^{-1} before non-radiative processes bring the excited level to 10187 cm^{-1} for emission between the ${}^2F_{5/2}$ state and the 407 ${}^2F_{7/2}$ state.

The Yb^{3+} ion had been under-utilised before diode-pumped solid-state lasers because it has only one excited $4F$ manifold near 1μm where the next level is $5D$ at a much higher energy. The $4F$ manifolds are finely split due to the Stark effect resulting in four levels at the ${}^2F_{7/2}$ level, and three levels at the excited ${}^2F_{5/2}$ state. The energies of these levels vary slightly with host material, and in the cases of Yb-doped KYW and KGW can be seen in Figure 2.1. The absence of higher states in Yb^{3+} makes broadband pumping inefficient, and so the full exploitation of Yb^{3+} was delayed until suitable pump diodes became available [51]. This lack of higher states, though, does have beneficial effects: it removes absorption of the excited state and also significantly represses upconversion.

The absorption of Yb^{3+} has peaks about 941 and 980 nm, corresponding to the excitation from the 0 cm^{-1} ${}^2F_{7/2}$ state to the 10695 cm^{-1} and 10187 cm^{-1} ${}^2F_{5/2}$

states, and its emission has a major peak at about 1030 nm, so $\frac{\nu_{signal}}{\nu_{pump}} = 0.951$, leading to a quantum defect, q, of 9.84×10^{-21} J. The quantum defect is defined as $q = \frac{hc}{\lambda_{pump}} - \frac{hc}{\lambda_{signal}}$, and is inversely related to the upper bound of efficiency. The small quantum defect also means that heat management in Yb:KYW and Yb:KGW is trivial, and extensive cooling is avoided.

In the host KYW, Yb^{3+} ions have a luminescence decay time of 0.85 ms at 295 K, indicating a long upper-state lifetime [3]. As illustrated later, this long upper-state lifetime provides damping of high-frequency noise from the pump source.

2.2.2. Properties of KYW

$KY(WO_4)_2$, or KYW, is an optically-transparent crystal with no apparent colour in the visible range, and when doped with Yb^{3+}, which replaces the Y^{3+} ions in the host material at a site with C2 point symmetry [50], glows with a very faint green or blue fluorescence when pumped due to upconversion processes. The UV cut-off frequency is 315 nm, and the transparency extends to 5400 nm [52]. Early attempts to fully characterise Yb:KYW for laser operation were done using a stoichiometric version of the crystal [53] wherein the Y^{3+} had been completely replaced with Yb^{3+} ions.

2.2.2.1. Crystallographic properties

There are two polymorphic versions of KYW: one, the α crystal, has a phase-transition temperature of 1025° C; the second version, the β modification, is not stable at room temperature, and will henceforth be ignored in favour of the α crystal. KYW is a monoclinic crystal – two of the characteristic angles within the Bravais lattice are 90° – and the atomic packing places it in both the C2/c and I2/c Federov groups with the parameters of the unit cell as seen in Table 2.1 [49, 52].

Both have the exact same crystal structure using differing coordinates, but as the C2/c group has been recommended as the standard by the International Crystallographic Union, and much prior work was completed using the C2/c group, it shall be the default employed in this work.

C2/c	$a = 10.64$ Å	$b = 10.35$ Å	$c = 7.54$ Å	$\beta = 130.50°$
I2/c	$a = 8.05$ Å	$b = 10.35$ Å	$c = 7.54$ Å	$\beta = 94°$

Table 2.1: Crystallographic axes of Yb:KYW in both C2/c and I2/c space groups.

2.2.2.2. Mechanical properties

KYW crystals can only be grown using a flux method – by dissolving the constituent ingredients into a solution, or flux, and allowing for crystal growth, either spontaneously or through seeding – because the α-KYW crystal bears a phase transition at 1010° C (which is below its melting point of 1050° C), and loses WO_3 above 1150° C [54, 55]. In many cases these crystals are grown using the top-seeded solution growth slow-cooling method (TSSG) [52, 56, 57]. Those grown along the (0 1 0) crystal plane exhibit a rectangular shape and good transparency throughout the volume, though even a "slight mis-orientation... [has] a pronounced effect on crystal quality" [56].

KYW crystals have a thermal conductivity – taken as the mean of the conductivity of the three crystallographic axes – of 3.3 W m^{-1} K^{-1}.The crystals register as 4.5-5 on Mohs' hardness scale, and, whilst they lack any distinct cleavage planes, are brittle and should be handled with care [49].

2.2.2.3. Crystallooptic properties

As can be seen in Figure 2.2, the principal crystallooptic axis, N_p, is parallel to the crystallographic b axis.

The crystallooptic axis with the greatest refractive index is N_g, at 18.5° clockwise of the crystallographic c axis. Work by Mateos *et al* [52] determined the Sellmeier coefficients for the different axes to be:

Sellmeier Index	A	B	C (μm)	D (μm^2)
N_g	3.55544	0.46438	0.15213	-0.03408
N_m	3.57271	0.30991	0.17484	-0.03401
N_p	3.50441	0.24431	0.18268	-0.03022

Table 2.2: The Sellmeier indices of the different crystallooptic axes of Yb:KYW.

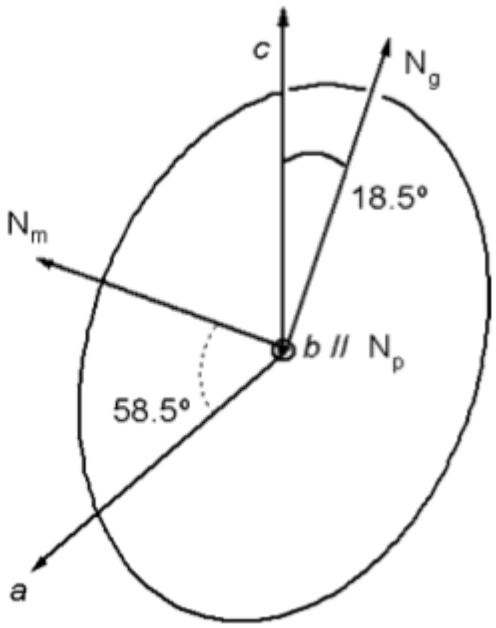

Figure 2.2: The orientation of the crystallographic axes of KYW, a, b, and c, compared to the optical axes, N_g, N_m, and N_p [52].

$$n^2(\lambda) = A + \frac{B\lambda^2}{\lambda^2 - C} + \frac{D\lambda^2}{\lambda^2}. \tag{2.1}$$

where the Sellmeier indices are listed in Table 2.2. From this we find the refractive indices to be in relation to each other according to $N_g > N_m > N_p$.

The absorption and emission of Yb:KYW differs depending on the direction of light propagation and electric-field polarisation. Kuleshov *et al* characterised the absorption and emission spectra of Yb:KYW along the different crystallographic axes, as can be seen in Figure 2.3. As their work shows, the absorption peak is at about 981.2 nm for all axes and emission is broad and centred about 1025 nm. The greatest absorption and emission occur in their work when the electric field is parallel to the a axis, though occasionally the b axis is the desired crystalline axis because of a broader emission spectrum [58].

In comparison to the better-known Ti:sapphire Yb:KYW has some advantages, mainly in its low quantum defect and higher nonlinear index. KYW also compares favourably with other host materials. Work had previously been performed in Yb:YAG, which allows for high power output near the emission of 1030 nm, but with difficulty of obtaining short pulse durations. Glasses have also been used in

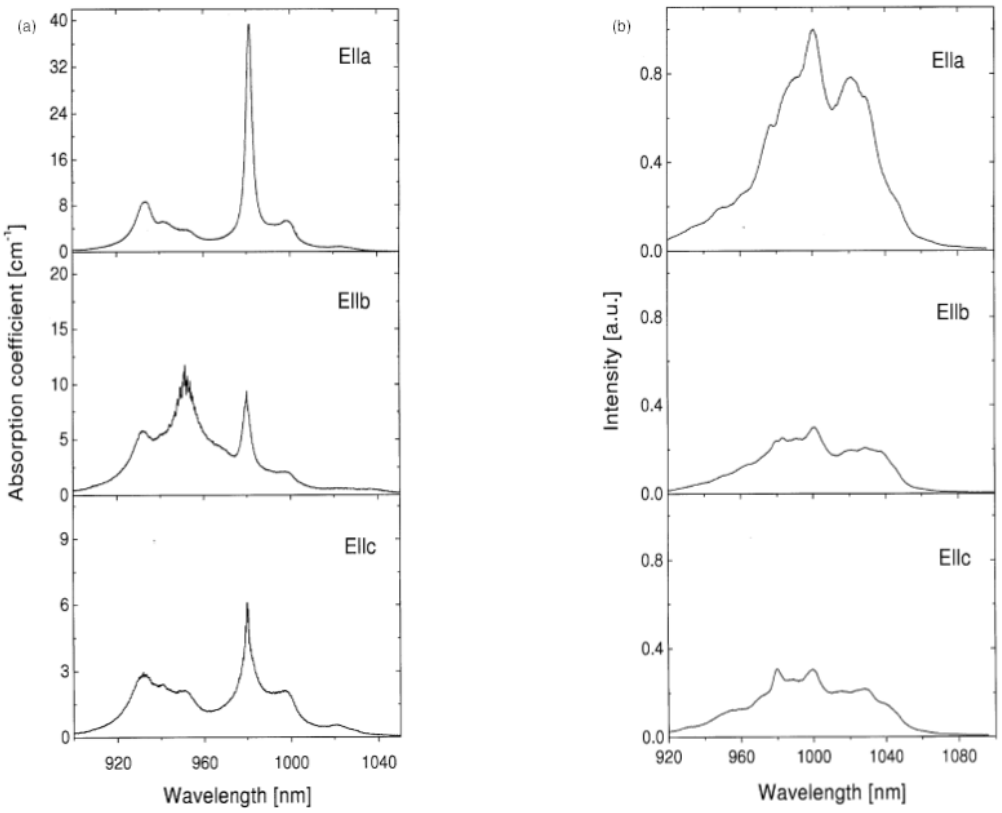

Figure 2.3: The absorption spectra (a) and emission spectra (b) of Yb:KYW at room temperature [3].

the past, but the poor thermal conductivity of glass acts as a deterrent save for in optical fibres.

2.2.3. Prior implementation of Yb:KYW in laser systems

In 1997 Kuleshov *et al* at the International Laser Center in Belarus demonstrated the first documented CW emission of Yb^{3+}:$KY(WO_4)_2$ and Yb^{3+}:$KGd(WO_4)_2$ using Ti:sapphire and diode-laser pump sources [3]. Yb^{3+} had been used as a dopant in YAG, apatite crystals, fluorophosphate glasses, and $BaCaBO_3F$ previously [3, 59], and this research was an investigation into the suitability of the monoclinic double tungstates as host crystals for Yb^{3+} due to their their suitability as hosts for other rare-earth ions, and these experiments utilised crystals with a 5 at% doping. Their work also estimated a stimulated emission cross section of 3×10^{-20} cm^2 for Yb^{3+} at 1025 nm. The group continued their efforts in probing the characteristics of these crystals in a later paper based on the use of a pulsed Ti:sapphire laser as the pump source [50], resulting in a demonstrated slope efficiency of 86.9% and a strong absorption coefficient (nearly 40 cm^{-1}).

Further exploration of the effects of diode pumping by the same group [59] reached slope efficiencies of 53% between 1026 and 1044 nm, and, through changing the concentration of Yb^{3+} in the host crystals (1 at%, 5 at%, 10 at%, and 20 at% were all tested) an eventual 66% slope efficiency. They rightly pointed out the potential of these lasers for low-peak-power ultrafast systems.

Not long after this, the first self-starting mode-locked laser systems using Yb:KYW were demonstrated by Liu *et al* at the University of Michigan. Unlike earlier work performed by Kuleshov and Lagatsky, this system was pumped with the electric field parallel to the *b* axis because of its greater emission spectrum. The authors also chose to operate at the broader 952-nm absorption peak due to issues of transmission and reflectance at the pump and signal wavelengths due to limitations of the cavity optics at the time – problems that have since been surmounted as these systems gain popularity. They were eventually able to obtain 71-fs pulses through Kerr-lens mode locking.

Kerr lensing was believed to be possible because Yb:KYW's measured nonlinear refractive index, n_2, is 8.7×10^{-16} cm^2/W, whereas Ti:sapphire's is only 3.1×10^{-16} cm^2/W, nearly three times less. As the efficiency of Kerr lensing increases with n_2, success was anticipated, though the nonlinear refractive index changes with incident intensity. A hard aperture was used to prevent multipulsing.

The following year, Klopp *et al* at the Max Born Institute in Berlin demonstrated another Kerr-lens mode-locked diode-pumped Yb:KYW laser with pulses in the 100-fs range [60] whilst Brunner *et al* at the Swiss Federal Institute of Technology (ETH) in Zürich achieved longer pulses of 240 fs with a thin-disk laser and an average power of 22 W [61]. Grabtchikov *et al* at the Stepanov Institute of Physics in Belarus realised the first Yb:KYW-based microchip laser in both CW and Q-switched operation using a slab of Cr^{4+}:YAG plate as a passive Q switch [62]. Their results showed Raman self-frequency conversion with 2 mW of average Stokes power.

Strides in improving the efficiency of these femtosecond lasers were made by Lagatsky *et al* at St Andrews University in 2003: using a narrow-stripe laser diode they were able to achieve 123-fs pulses at an average power of 107 mW for 308 mW

of incident power leading to an optical-to-optical conversion efficiency of 38% (and an electrical-to-optical conversion efficiency of 14%) [63] through nearly diffraction-limited pumping and SESAM modelocking. They later accomplished 50% optical-to-optical efficiency [64].

Paunescu *et al* at the Institute for Optics and Quantum Electronics in Jena produced another diode-pumped femtosecond laser in the interests of comparing the performance of KGW to the already established KYW to judge their suitability for ultrafast laser operation for the POLARIS system (Petawatt Optical Laser Amplifier for Radiation Intensive ExperimentS). Their setup was a 5 at%-doped Yb:KGW crystal cut for b-axis propagation of the electric field and SESAM-generated modelocking. Their modelocking was stable, but was also double pulsing. They achieved 174-fs pulses with low efficiency, but still high average output power which made their Yb:KGW system suited for the task of seeding the POLARIS amplifiers [65].

The ongoing characterisation of Yb-doped monoclinic double tungstates was progressed by Aznar *et al* at the Rovira i Virgili University in Spain, who continued to grow and test Yb:KYW and Yb:KGW to obtain a high optical quality through the use of a KYW substrate [66].

In another direction, Killi *et al* at the Max Planck Institute in Heidelberg were engaging in research to produce cavity-dumped lasers utilising Yb:KYW as the gain material. As these sources are "between oscillators and amplifier systems" in terms of pulse energy and repetition rate [67] they are considered ideal for applications in microstructuring, laser surgery, tissue manipulation, and others. Using a β-barium borate (so designated as it is the β crystalline configuration) Pockels cell and post-cavity compression they were able to achieve 21-fs pulses with peak powers of 13 MW at 1 MHz.

In 2006, Hildebrandt *et al* in Göxe, Germany, were working on wavelength tuning Yb:KYW lasers for the purpose of minimising the quantum defect. They were able to achieve a tuning range of 64 nm and an output power of 10.7 W with CW operation. They were also able to demonstrate a quantum defect of 0.6%: further improving efficiency and reducing thermal cooling requirements [68]. Lagatsky *et al* went

on to try new modelocking methods – a PbS quantum-dot-doped glass saturable absorber – and achieved 2.6-ps pulses at 99 MHz and with an average output power of 250 mW. A conversion efficiency of 26% was determined [69]. Meanwhile, Jacquemet *et al* at the Central University in Orsay Cedex, France, tested intracavity second-harmonic generation. Their work achieved simultaneous generation of 55 mW of light at 501.7 nm and 550 mW at 1003.4 nm – a 6% conversion efficiency – and identified the main technological limitations behind this performance. It was the shortest wavelength of light generated by Yb:KYW at that point [70] and presented a workable replacement for the notoriously fickle Ar^+-ion lasers.

Further work towards increasing the constantly growing capabilities of Yb:KYW lasers was performed in 2007. Jacobsson *et al* at the Royal Institute of Technology in Stockholm demonstrated a widely-tuneable Yb:KYW laser using an intracavity volume Bragg grating. They were able to tune between 997 nm and 1050 nm smoothly with a bandwidth of < 0.1 nm and a maximum output power of 4.7 W [71]. Kalisky *et al* at the Nuclear Research Centre in Israel compared the Q-switched performance of Yb-doped tungstate and garnet lasers. Using Cr^{4+}:YAG as a saturable absorber they were able to show high-pulse-power with a short duration allowing for the eventual and future construction of a Yb:YAG and Yb:KYW microlaser [72]. Passive modelocking of Yb:KYW lasers was being investigated by Palmer *et al* at Leibniz University in Hannover, though in this case it was on thin-disk oscillators. By cavity dumping using BBO the authors were able to achieve 3-μJ pulses with durations of 680 fs: similar in their energies to large, power-hungry Yb:YAG oscillators [73]. Lagatsky *et al* were spending time on Yb:KYW oscillators utilising low-loss quantum-dot saturable absorbers for modelocking with less than 0.2% loss at a modulation depth of around 2.3% [74].

Whilst most of these systems thus far were focussed on obtaining mode-locked pulses, Meyer *et al* were the first to present a carrier-envelope offset-frequency-stabilised Yb:KYW laser [75]. Through Kerr-lens mode locking the authors were able to obtain 290-fs pulses at 160 MHz. These pulses were then amplified and compressed to 80 fs before being coupled into a microstructure fibre to broaden the

signal to a full octave, allowing for f-$2f$ comparison by heterodyne processing.

Yamazoe *et al* pursued greater repetition rates. By making a very simple and small cavity they were able to generate 162-fs pulses at 2.8 GHz with an average energy of 680 mW, but an optical-to-optical efficiency of 34% [76], much less than that presented here. Seger *et al*, on the other hand, were continuing the work of Jacobsson in building a tuneable Yb:KYW laser. This time, dispersion management was included into the Bragg grating. By chirping the grating their pulses were shorter than before, but the tuning range was narrower, and the average power lower [77].

Wasylczyk *et al* at the University of Warsaw worked on Yb lasers with higher repetition rates. One of their experiments centred around a 1-GHz, ring cavity Yb:KYW laser that produced pulses of approximately 200-fs duration and with an optical-to-optical conversion of 24% [78] whilst another was a z-fold cavity with pulses of 315 fs, a repetition rate of 82 MHz, and a conversion efficiency of 33% [79]. Both of their systems utilised soft-aperture KLM.

At CLEO/QELS in 2010 Pekarek *et al* presented their work on the first SESAM-mode-locked oscillator at 1 GHz, using Yb:KGW. Their pulses had a duration of 317 fs and the average output power of the system was 120 mW for a pump power of nearly 2 W [80]. At the same conference Siegel *et al*, of High Q Laser Innovation GmbH, presented their work on a relatively high repetition rate cavity-dumped laser using a β-barium borate Pockels cell. Their work was able to achieve 264-fs pulses at 4.58 MHz [81].

Yamazoe *et al* were continuing their work on physically small, high-repetition rate Yb:KYW oscillators. They were able to construct a 2.8 GHz, SESAM-mode-locked system with 162-fs pulses and an average output power of 680 mW in a simple linear-hemispherical cavity in which the light passed through the curved mirror. Their optical-to-optical conversion efficiency of approximately 28% [82], which, while mode-locked, was of a lower efficiency than their work in [76].

Further work on high-power systems was performed by Kim *et al* at the SOI-Korea Centre and by Pekarek *et al*. The former produced a 200-fs, 85.5 MHz,

SESAM-mode-locked Yb:KYW oscillator with an average output power of 3.5 W (20 W incident) [83] whilst the latter, through harmonic modelocking brought about by tighter focussing on the SESAM, were able to create a 4 GHz laser with average output power of 900 mW and a pulse duration of 290 fs [5]. A summary of the work can be found in Table 2.3.

It was with these systems in mind that the construction of a uniquely high-repetition-frequency and high-efficiency Yb:KYW laser was investigated.

2.3. Yb:KYW laser design

The first system to be designed and built was a 1-GHz cavity in the interests of creating a system that could allow for femtosecond optical frequency comb generation with a high level of inherent separation between comb modes, thus ensuring a high degree of accuracy in future experimental applications. Our 10-at.%-doped Yb^{3+}:$KY(WO_4)_2$ crystal was Brewster-cut to improve intracavity efficiency and was 720-μm thick, as seen in Figure 2.4. The shorter length reduces the need for high beam quality from the pump sources and ensures that some pump light is left unabsorbed: three-level and quasi-three-level gain materials require the entire volume to be strongly pumped to avoid reabsorption of the laser wavelength. The theoretical pump absorption of the system was calculated to be 79.8%.

The crystal was orientated for propagation along the b crystallographic and N_p optical axes to ensure the polarisation would remain linear and parallel to the crystallooptic N_m axis in which the largest absorption cross-section resides.

2.3.1. 1-GHz cavity design

The initial design was a simple four-mirror cavity modelled using LCAV, a program capable of analytically optimising laser resonators using ABCD matrices, in order to find a design that would have excellent tangential and saggital beam plane stability-zone overlap and a tight intra-cavity focus. The cavity was designed to be approximately 15 cm in length to ensure the 1-GHz repetition rate that was desired. Figure 2.5 shows a cavity schematic and illustrates the predicted beam propagation in the cavity and the subsequent behaviour of the beam at each intracavity interface.

Ref.	Year	Doping (at%)	P_{in}	P_{out}	Input/Output Efficiency	Pulse Width	Repetition Rate
[3]	1997	5 at%	940 mW	500 mW	4.3%	N/A	N/A
[50]	1997	5 at%	1000 mW	43 mW	4.3%	N/A	N/A
[59]	1999	5 at%	650 mW	60 mW	9.2%	N/A	N/A
[84]	2000	5 at%	240 mW	93 mW	38.8%	N/A	N/A
[58]	2001	10 at%	430 mW	227 mW	52.8%	107 fs	110 MHz
[60]	2002	5 at%	1100 mW	100 mW	9.1%	101 fs	95 MHz
[62]	2002	10 at%	550 mW	26 mW	4.7%	2 ns	49 MHz
[61]	2002	5 at%	100 W	22 W	22%	240 fs	24.6 MHz
[63]	2003	10 at%	350 mW	107 mW	30.6%	123 fs	114 MHz
[66]	2004	N/A	275 mW	40 mW	14.5%	N/A	N/A
[65]	2004	5 at%	3.35 W	126 mW	3.8%	174 fs	108 MHz
[64]	2004	10 at%	430 mW	227 mW	52.8%	107 fs	294 MHz
[67]	2005	N/A	18 W	N/A	N/A	380 fs	1 MHz
[85]	2005	10 at%	970 mW	360 mW	37.1%	114 fs	86.4 MHz
[69]	2005	10 at%	950 mW	250 mW	26%	2.6 ps	99 MHz
[86]	2006	5 at%	19.1 W	3.6 W	18.8%	N/A	N/A
[68]	2006	10 at%	22 W	10.7 W	48.6%	N/A	N/A
[87]	2006	1.5 at%	200 W	10 W	5%	290 fs	45 MHz
[70]	2006	10 at%	3.2 W	550 mW	17.2%	N/A	N/A
[72]	2007	10 at%	12 W	70 mW	0.6%	N/A	8 kHz
[71]	2007	5 at%	19.3 W	4.7 W	24.4%	N/A	N/A
[73]	2007	10 at%	50 W	2.5 W	5%	370 fs	16 MHz
[74]	2007	10 at%	3 W	500 mW	16.7%	114 fs	106 MHz
[88]	2008	10 at%	3.5 W	500 mW	16.7%	114 fs	107 MHz
[75]	2008	10 at%	1.2 W	120 mW	10%	176 fs	86.4 MHz
[76]	2009	10 at%	2 W	680 mW	34%	162 fs	2.8 MHz
[78]	2009	10 at%	485 mW	115 mW	23.7%	200 fs	650 MHz
[79]	2009	10 at%	530 mW	174 mW	33%	315 fs	82 MHz
[77]	2009	5 at%	18.5 W	3.3 W	17.8%	N/A	590 MHz
[81]	2010	5 at%	25 W	2.7 W	10.8%	234 fs	22.9 MHz
[80]	2010	5 at%	1.7 W	120 mW	7%	317 fs	1 GHz
[82]	2010	5 at%	2.5 W	680 mW	27.2%	162 fs	2.8 GHz
[83]	2010	5 at%	20 W	3.5 W	17.5%	200 fs	85.5 MHz
[5]	2010	5 at%	5.5 W	1.1 W	20%	281 fs	1 GHz

Table 2.3: Summary of experiments involving Yb-doped tungstates prior to the start of the project.

As the crystal was Brewster-cut, and therefore an off-axis optic, the cavity design had to compensate for the introduced astigmatism to ensure the minimal beam waist. An asymmetric, astigmatically-compensated z-fold cavity was chosen. The mirrors were made with coatings to be highly-reflecting (HR) between the wavelengths of 1020 and 1100 nm. At the desired peak wavelength, 1040 nm, the optical

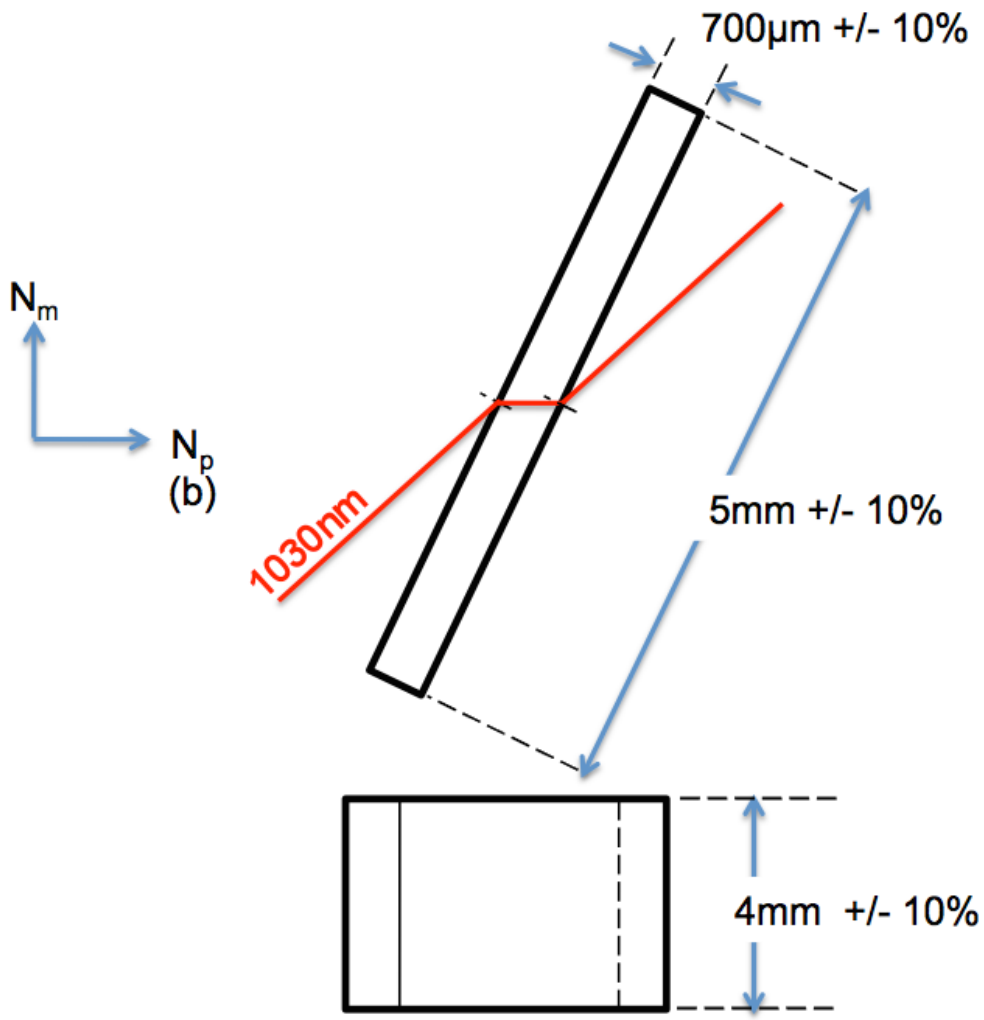

Figure 2.4: A diagram showing the inherent qualities of the Yb:KYW crystal used in this work. The crystal was 700-μm thick and Brewster-Brewster cut to allow for low insertion loss at one polarisation and with a longer path length through the material due to it being off-axis.

transmission loss of these mirrors was less than 0.06%. At the pump wavelength the AR properties allowed for a transmission greater than 95%.

The initial design was that of a standing-wave cavity with a high reflector plane mirror at one end (i). The light propagated 70 mm to another, concave, high reflector with a radius of curvature (RoC) of -30mm (ii). This mirror had a half angle of 5° from the original path. From there the light travelled 19.4 mm before passing through the Yb:KYW crystal (x) – at a Brewster's angle of 63.4° – and continued for a further 11.2 mm where would hit the third mirror (iii): another concave high reflector with RoC= −20mm. This third mirror had a half angle of 4°. From there the light travelled 50 mm to a plane output coupler (iv).

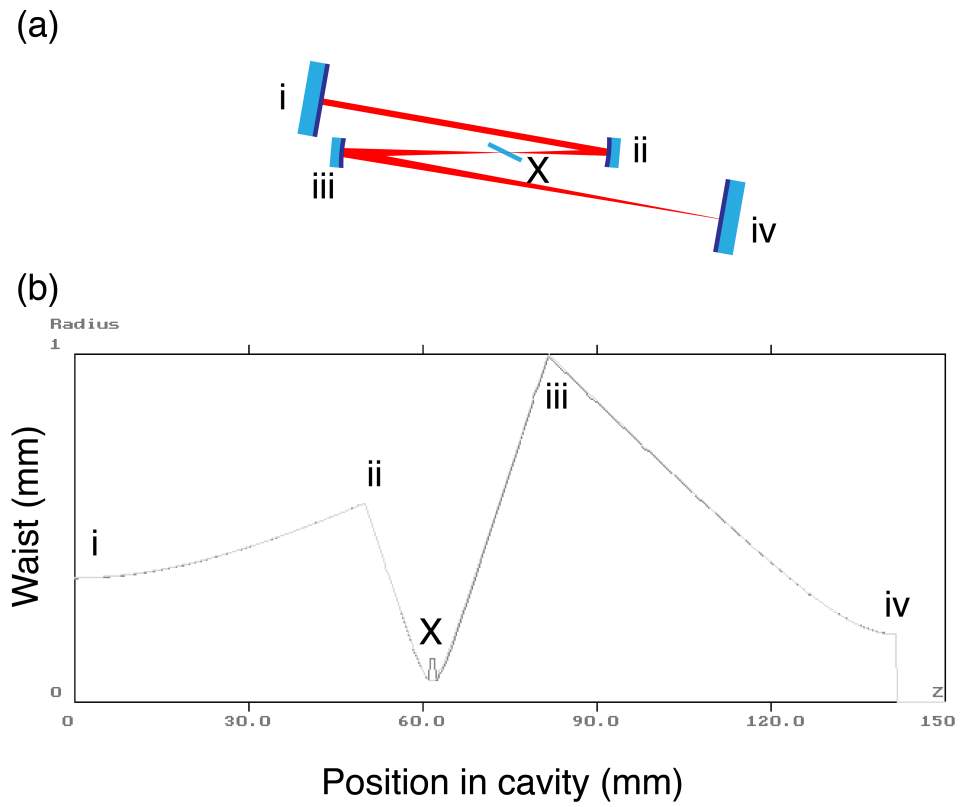

Figure 2.5: (a) Initial 4-mirror cavity design; (b) the modelled beam propagation in the designed cavity. The close matching of both the tangential and sagittal planes is seen. The mismatch at the smallest radius is due to passage through the Yb:KYW crystal, which is off-axis. Values are in mm.

The output arm was designed for collimation allowing a nearly collimated beam to pass through the output coupler, while the mode-locking arm focussed the beam down at one end of the cavity to allow the placement of a semiconductor saturable absorber mirror (SESAM) there for self-starting modelocking.

The crystal was simultaneously pumped by two commercially-available polarisation-maintaining fibre-pigtailed laser diodes manufactured by 3S Photonics (1999 CHP). These diodes both operated at the peak absorption wavelength of Yb:KYW of 981 nm. The diode lasers were wavelength-stabilised using fibre-Bragg-gratings and were spliced to high-birefringence polarisation-maintaining fibre patchcords connectorised at their ends with FC/APC terminators to reduce back-reflection. The average powers produced were 674 and 679 mW; both lasers had a -3dB spectral bandwidth less than 1 nm. Each laser was collimated using a ThorLabs F220APC-1064 FC/APC collimator, with a focal length of 18.24 mm and a collimated beam

diameter of 2.0 mm.

To determine the focal lengths of the lenses necessary to properly couple the light effectively into the laser crystal with a beam diameter of 20 μm, needed for modematching with the intracavity beam as determined through LCAV, a knife-edge measurement was performed and a beam profile was created according to the $1/e^2$ intensity, shown in Figure 2.6. From these measurements the complex beam parameter was determined to be

$$q = 1.0350 \times 10^3 + i1.8158 \times 10^2 \text{m}. \tag{2.2}$$

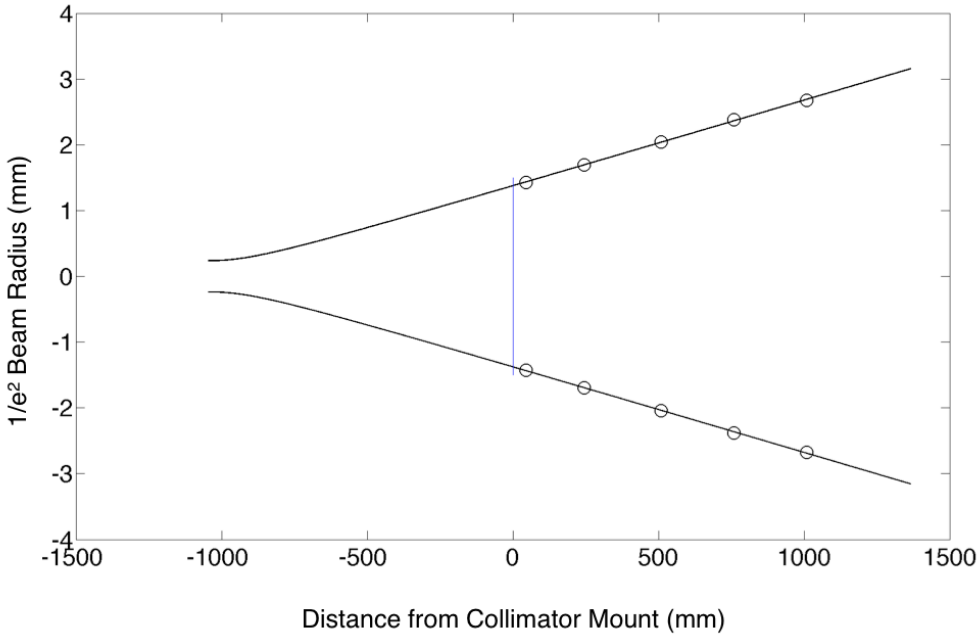

Figure 2.6: The beam profile of the fibre-pigtailed laser diodes, determined through knife-edge measurements. The beam may look like the waist is deep within the fibre, itself, but that is because this model does not indicate the actual effect of the collimating lens, but was to find the complex beam parameter of the beam with the intent of discerning the propagation of light through the cavity.

Using this information the next step was to model the propagation through lenses and the folding mirrors to find the optimal focal lengths so as to have one focussing arm whilst still maintaining population inversion in the laser crystal through a spot size less than 20 μm. Due to the two folding mirrors being of differing RoC and varying distances to the crystal, two different models had to be made to mathematically model the beams using ABCD matrices, and can be seen in Figures 2.7

and 2.8.

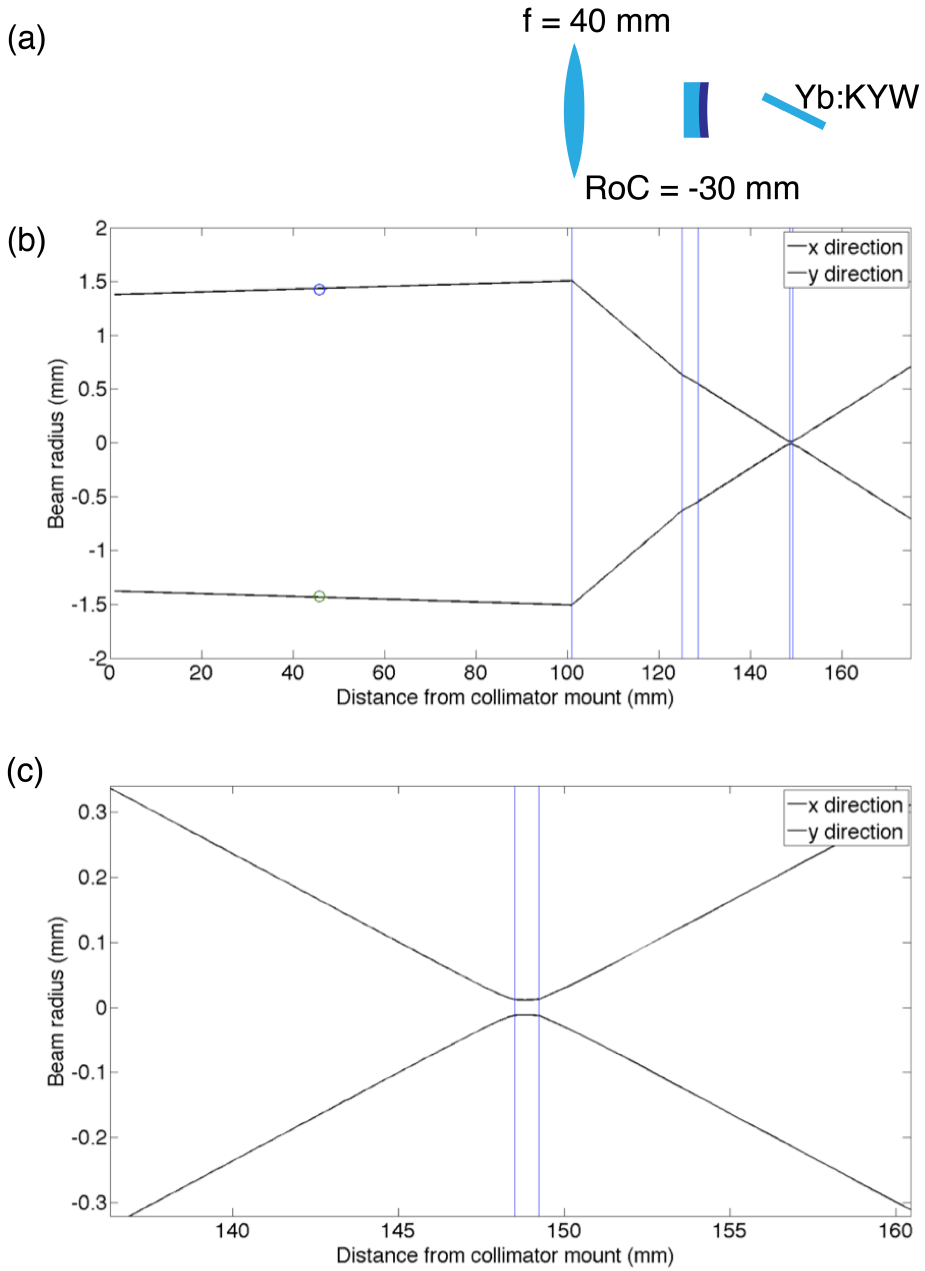

Figure 2.7: (a) Layout of the pump lens, cavity mirror, and Brewster-cut Yb:KYW crystal. (b) CW propagation of one of the pump lasers through the lens (first vertical blue line), mirror (centre pair of blue vertical lines), and crystal (final pair of vertical blue lines). (c) propagation within the crystal (vertical blue lines).

Using the models the correct pump lenses were identified, and found to have focal lengths of 40 mm for pumping through the RoC $= -30$ mm mirror and 30 mm for pumping through the RoC $= -20$ mm mirror.

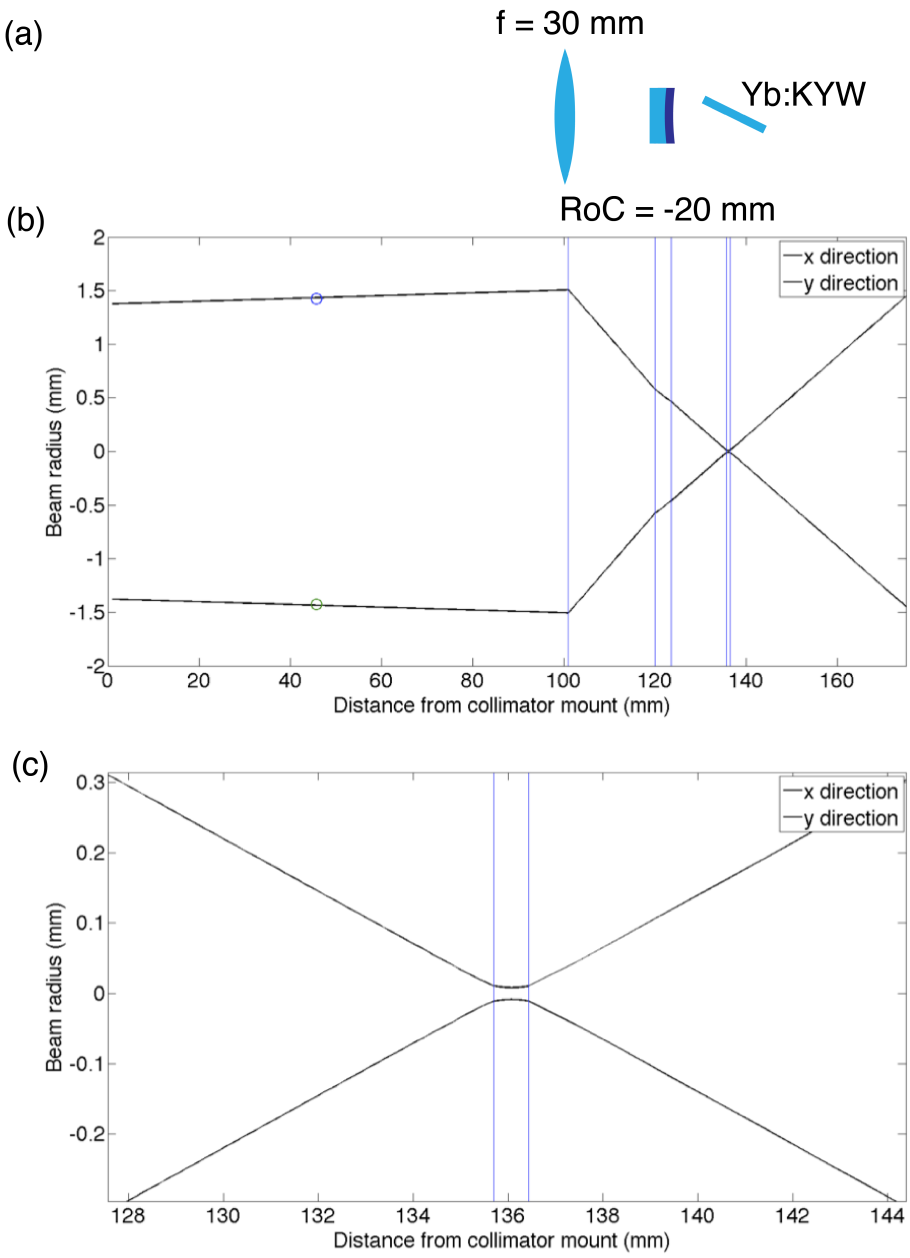

Figure 2.8: (a) Layout of the pump lens, cavity mirror, and Brewster-cut Yb:KYW crystal. (b) CW propagation of one of the pump lasers through the lens (first vertical blue line), mirror (centre pair of blue vertical lines), and crystal (final pair of vertical blue lines). (c) propagation within the crystal (vertical blue lines).

Measurements were also taken of the output power of the laser diodes related to the current passing through them, and are seen in Figure 2.9. Due to the linear nature of the output a simple equation was sufficient to describe each of them.

$$P_1 = 0.6821 I_1 - 41.545 \tag{2.3}$$

and

$$P_2 = 0.6798 I_2 - 34.504. \tag{2.4}$$

The power (P) is in mW and current (I) is in mA. These equations indicate the slope efficiency (68.21% and 67.98%) as well as the laser threshold (41.545 and 34.504 mA) of each laser.

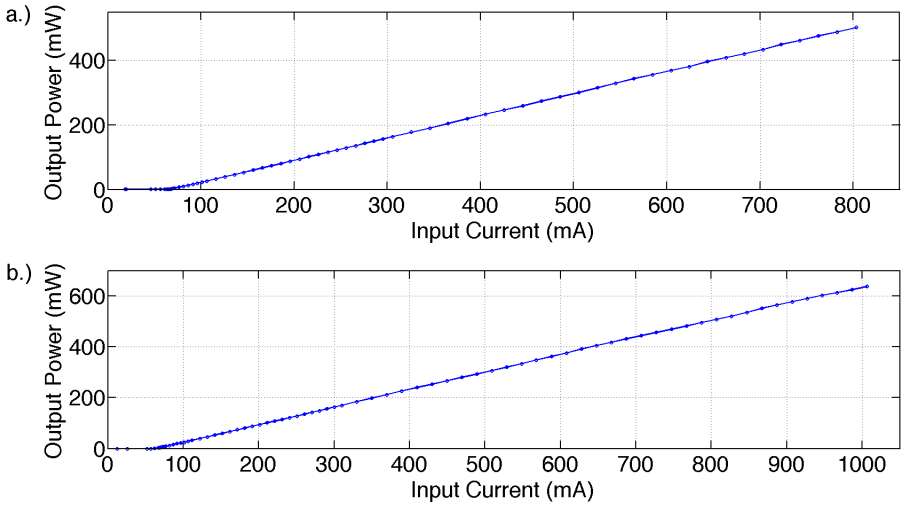

Figure 2.9: The output power of pump lasers 1 (a) and 2 (b) with increasing current

This light from the laser diodes was collimated, passed through half-wave plates to linearise and control the polarisation entering the KYW crystal for optimal transmission, and then focussed into the cavity (shown in Figure 2.10) using short focal length lenses selected using the previously mentioned modelling so that, when combined with propagation through the curved mirrors, provided a focal-spot radius of 17 μm ($1/e^2$ intensity) in the crystal. The coupling optics were all antireflection (AR) coated for 981 nm, and were chosen to ensure the best possible modematching and overlap of the pump beams with the intracavity beam.

At one end of the cavity was placed a plane-wedged output coupler with a transmission of 10%, initially. This value was chosen from the varied output couplers at hand through a Rigrod analysis [89] to ensure maximum laser power. A graphical representation of the results can be seen in Figure 2.11. In a Rigrod analysis a series of data points is measured of the output power of the laser with varying output coupling transmissions. These data are then fitted to the function:

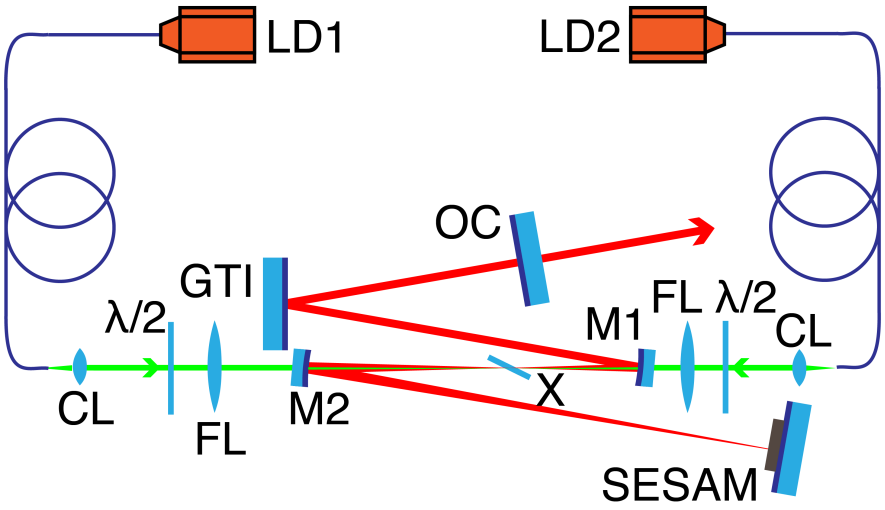

Figure 2.10: The 1-GHz cavity design for cw operation. Laser diodes (LD) emit 981-nm light (represented by green) that passes through coupled fibres before making its way through collimating lenses (CL), half-wave plates ($\lambda/2$), focussing lenses (FL), and the cavity's folding mirrors (M1 and M2) before meeting in the crystal (X). Generated 1040 nm light is shown in red.One direction has the output coupler (OC) whilst in the other direction is a highly-reflecting end mirror. M1 has RoC = -20 mm; M2 has RoC = -30 mm; FL1 has a focal length of 30 mm; FL2 has a focal length of 40 mm.

$$I_{out} = T_2 I_2 = \frac{T_2 I_{sat}}{(1 - r_2/r_1)(1 - r_2 r_1)} \left(\ln(G_0) - \ln\left(\frac{1}{r_1 r_2}\right)\right) \tag{2.5}$$

from which the maximum extractable intensity is derived to be

$$I_{avail} = 2\alpha_{m0} L_m I_s at \equiv \ln(G_0) I_{sat} \tag{2.6}$$

where G_0 is the single-pass unsaturated gain, α is the parasitic loss, and I_{sat} is the saturated output power of the laser [89], which were in this case $G_0 = 1.5252$, $\alpha = 0.024$, and $I_{sat} = 633.13$. The single-pass gain on that order indicates that the optimal output coupling would always be at the low end of transmittance as a single round trip would be unable to provide enough gain to remain a powerful steady-state system.

The measured, combined, incident pump power (after passing through the as-

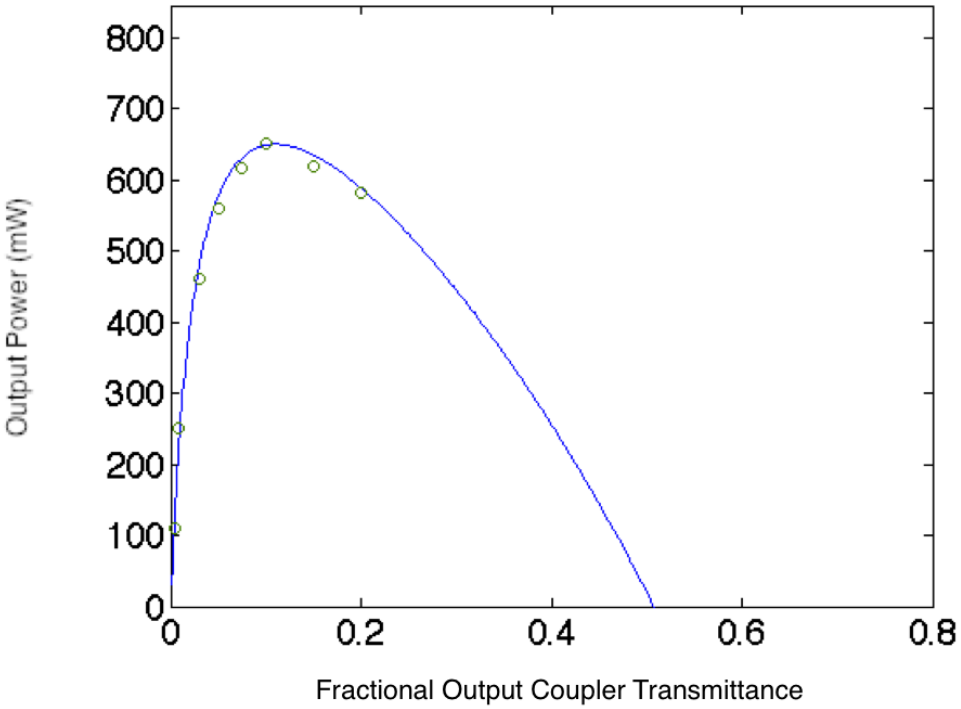

Figure 2.11: A Rigrod analysis of the optimal output coupling of the Yb:KYW laser – a maximum is sought, which can be seen about 10% transmission – for 1274 mW in. This has been fitted from Equation 2.5

sorted optics) on the laser crystal was 1274 mW due to the exceptional quality of the optics. This corresponded to a maximum output power of 650 mW with both diodes turned on. A power in/power out measurement was taken for two cases: that of one diode increasing in power before the other, and that of the two increasing together. These measurements are presented in Figure 2.12. From these measurements it was discovered that the laser had a slope efficiency of 51% and an optical-to-optical conversion efficiency of 50.5% with a spectrum centred about 1040 nm ($\approx$ 288.3 THz).

2.3.2. Optomechanical components used in construction

Due to the physical limitations of such a small cavity (for a standing-wave cavity to operate at 1 GHz it must be less than 15 cm in length), and the demands of SESAM modelocking, the different optics required mounts with a large degree of adjustability whilst still remaining non-intrusive. The angles within the designed cavity were also near-normal.

A great amount of thought and design went in to how the optics would not only

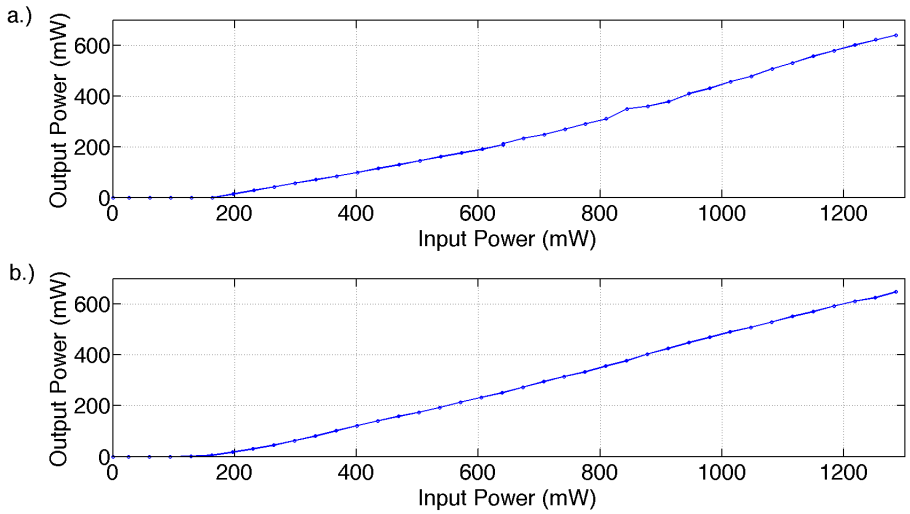

Figure 2.12: (a) is the power out of the Yb:KYW laser with the two pump diodes increasing in power one after the other, and (b) represents a simultaneous increase.

be held, but also adjusted and locked in place. It was apparent that the system would require linear stages that would not only maintain their position without the need to constantly readjust, but also a high number of turns per mm to ease the optimisation of the laser. The choice was made to use a series of steel extended contact bearing stages made by Opto-Σ because of the stages' high linear resolution and low angular drift. The remaining optomechanics, those which didn't move, were designed in Autodesk Inventor and submitted for construction through CNC (Computer Numerical Control) machining by the David Brewster workshop from aluminium, with the exception of the crystal mount which was milled from copper (Figures 2.13 and 2.14).

The laser was planned to be at 100 mm above table height so, along with a baseplate to allow for the optomechanics to be clamped in place to the table, spacers were also designed to ensure beam propagation at the centre of the optics, some of which were only 6.5 mm in diameter. Because of the small angles we used arms cantilevered from the tilting mirror mounts to hold each mirror in the beam path while allowing access to the translation stages and avoiding blocking further placement of mounts and stages. As can be seen in Figure 2.15 the designs were varied, but simple in construction.

Other designed components were baseplates and adapters of different sizes, which

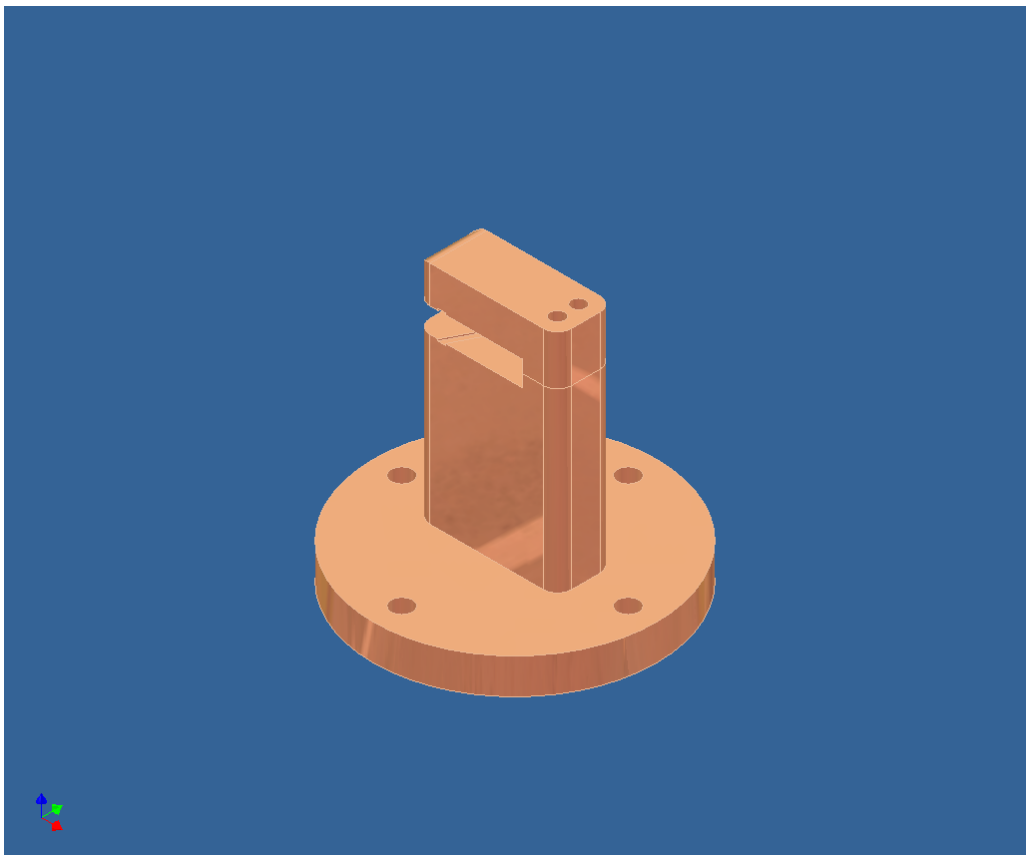

Figure 2.13: The copper-milled crystal mount made to gently hold the Yb:KYW crystal at Brewster's angle within the crystal. By utilising copper there was no need for extra temperature stabilisation or active cooling as there was ample volume for the amount of heat produced.

Figure 2.14: A close-up photo of the milled copper mount *in situ*.

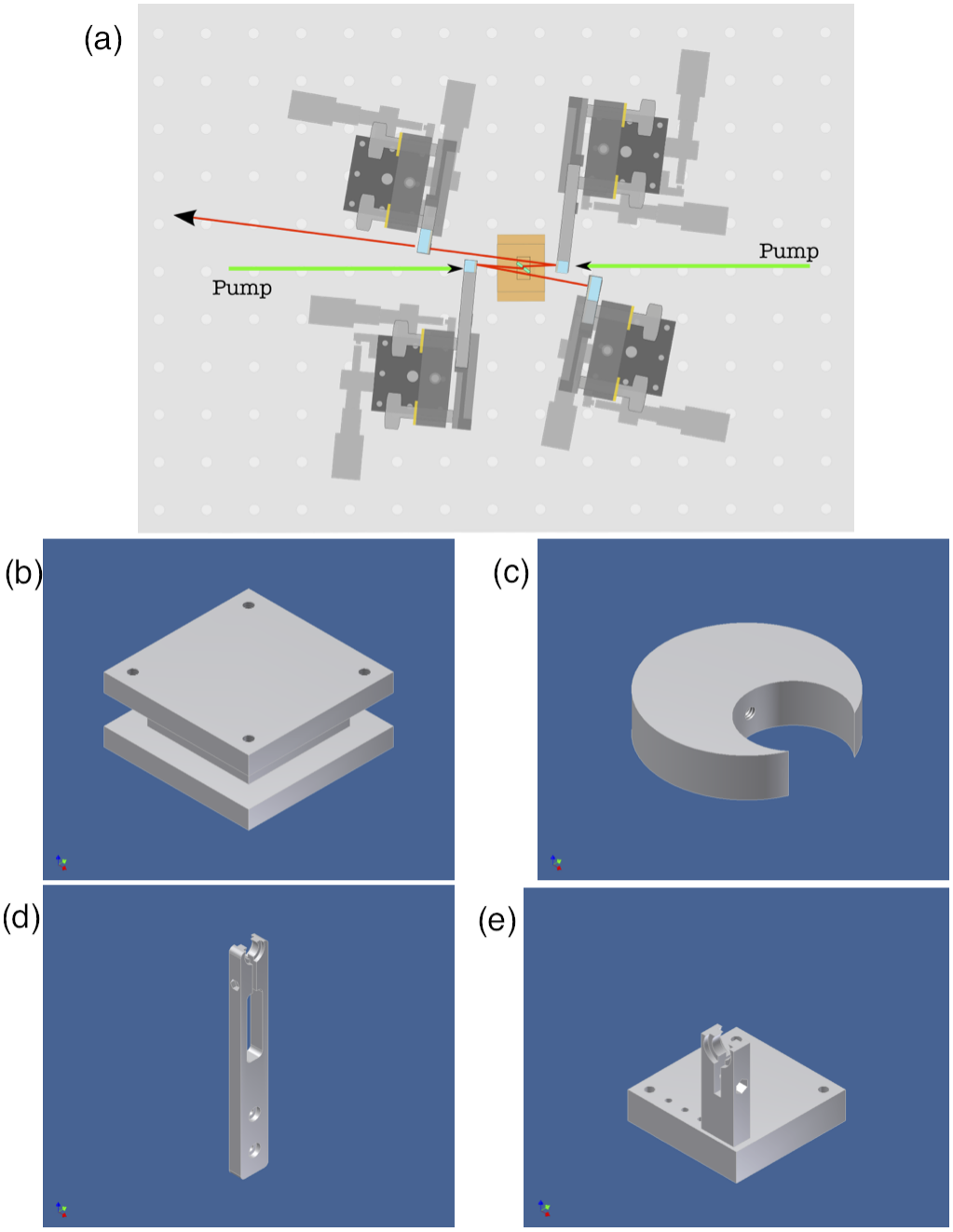

Figure 2.15: (a) Top-down representation of the cw laser cavity of the same length as that of the mode-locked system with a folding mirror (by Christopher Leburn); (b) base plate for the system; (c) adapter to a 25 mm mount for 12.5 mm optics (off-axis to allow for more space); (d) mirror-holding arm for 6.5-mm optics; (e) holder for the pump lenses.

are not shown here. A photograph of the assembled laser is shown in Figure 2.16.

2.3.3. Modelocking elements in the 1-GHz cavity

In order to generate self-starting modelocking we replaced the highly-reflecting end mirror with a non-resonant semiconductor saturable absorber mirror, or SESAM, made by BATOP GmbH. The characteristics of our device were a saturation fluence

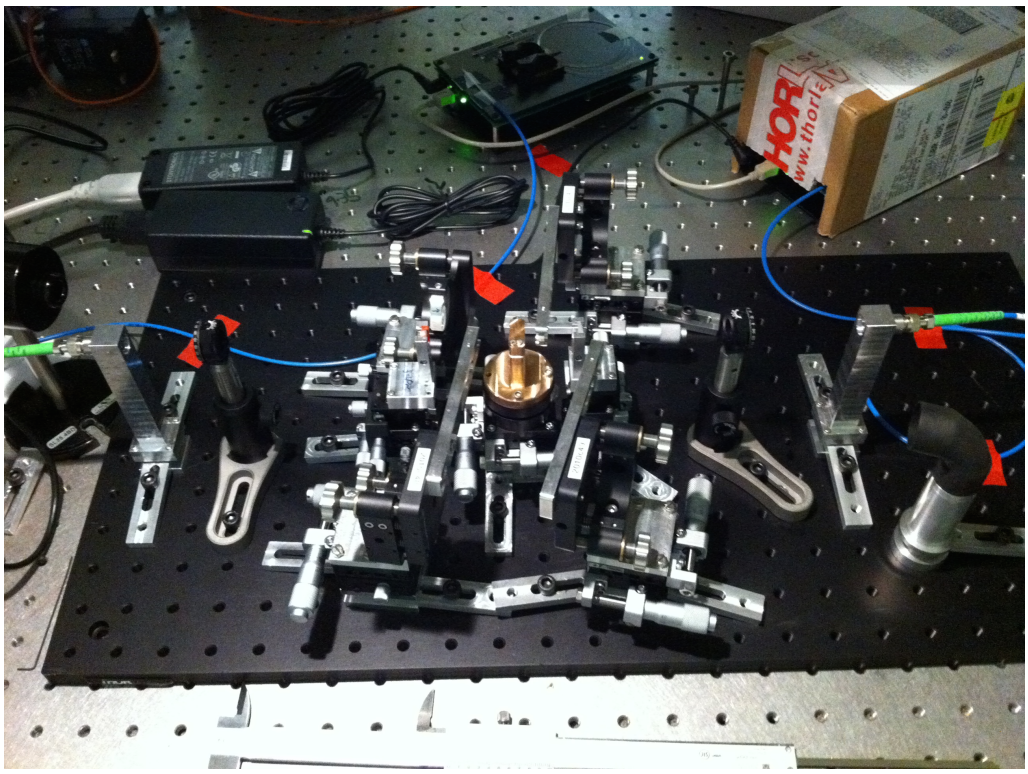

Figure 2.16: The 1-GHz cavity with all designed optomechanics assembled and mounted upon the breadboard.

of 90 μJ cm^{-2}, a nonsaturable loss of 1%, and a modulation depth – the upper bound for the device's nonlinear change in reflectance – of 0.5%. SESAMs are a distributed Bragg reflector capped by a saturable absorber: for this device a GaAs quantum well. Normal cw operation lacks the intensity required to saturate the absorber into transparency, but the leading edge of a pulse can, so the inclusion of a SESAM can lead to self-starting modelocking at a repetition rate directly related to the length of the cavity, though cw operation is also possible.

Our fifth surface, a Gires-Tournois interferometer (GTI) mirror, was included in the cavity to correct group delay dispersion (GDD), and had a double-pass GDD of -2600 fs^2. This optic was chosen through trial-and-error testing with several GTIs of varying GDD characteristics for the mirror that produced the shortest pulses. This resulted in greater negative intracavity GDD compensation when compared to the modelled value present from the Sellmeier equation – approximately 400 fs^2 – but by passing through air and reflecting off of dielectric mirrors the intracavity GDD was also higher than that derived purely from the dispersion characteristics of Yb:KYW, as well as possessing a change in nonlinear refractive index due to the presence of

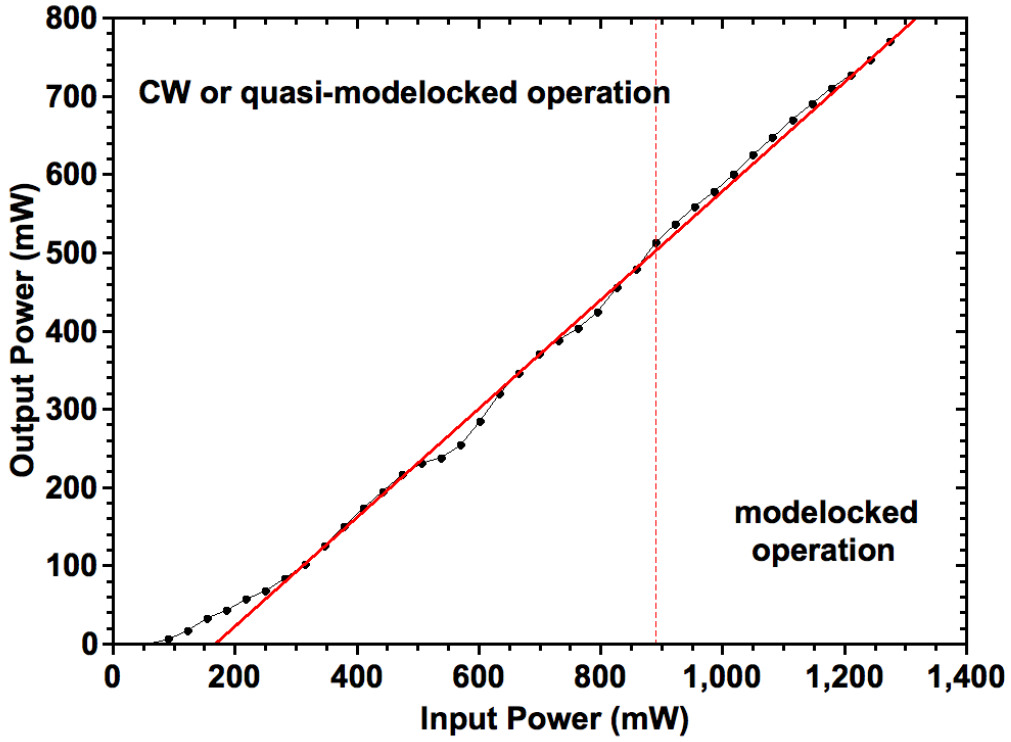

Figure 2.17: The power transfer characteristic produced by the 1-GHz Yb:KYW laser. Mode-locked operation was achieved at powers to the right of the dashed line. The slope efficiency (solid red line) was 67%.

an intracavity intensity.

2.4. Characteristics of the mode-locked 1-GHz cavity

The construction of the 1-GHz cavity was recorded and published as the mode-locked Yb:KYW laser with the highest-recorded optical-to-optical conversion efficiency in the GHz range of pulse repetition frequency [90]. With 1274 mW of incident power on the Yb:KYW crystal in the centre of the cavity the laser output was 770 mW, corresponding to a conversion efficiency of 61% and a slope efficiency of 67% when modelocked. The increase in output power arose as a result of a different choice of output coupler due to new terms of intracavity loss relating to the SESAM, thought to be a result of a faulty high reflector initially in place. These results can be seen in Figure 2.17

This exceptional level of efficiency was achieved through careful mode matching of the pump light, delivered by high-beam-quality fibre-coupled 981 nm laser diodes, with the intracavity mode. Due to the simple electronic structure of Yb^{3+} it is also possible to avoid excited-state absorption, up-conversion, and cross-relaxation. One

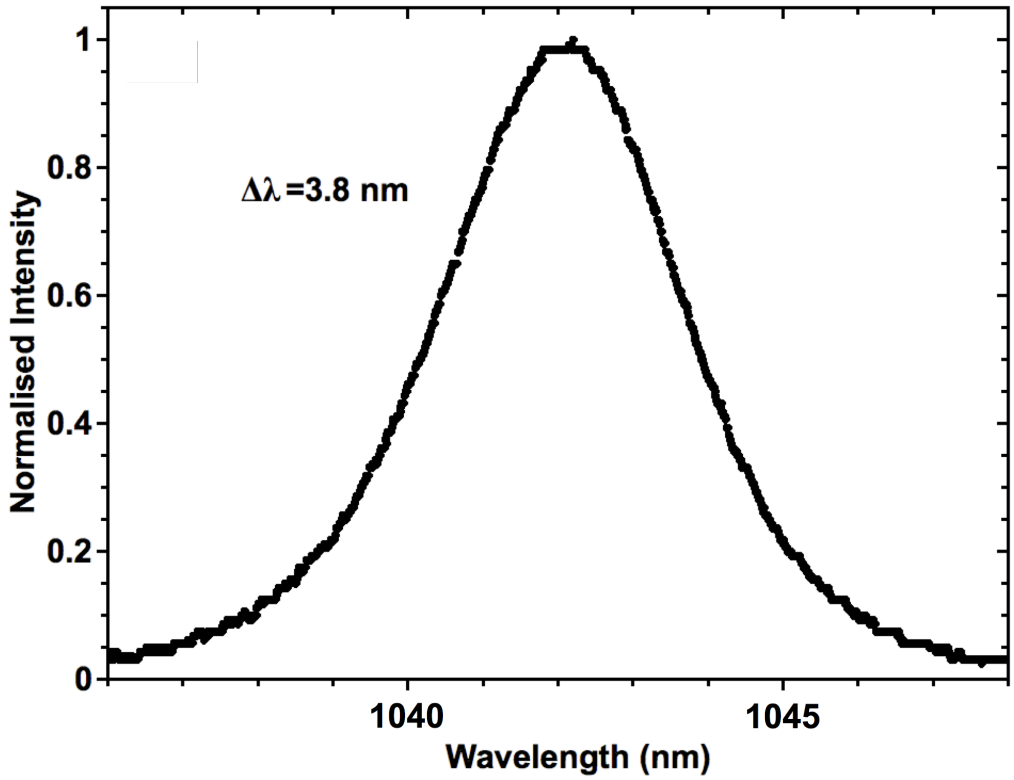

Figure 2.18: The output spectrum of the 1-GHz Yb:KYW laser centred at 1042 nm with a spectral width of 3.8 nm.

major hurdle to overcome, though, was the need to deplete the ground state to prevent reabsorption: this can be accomplished through high pump intensities. By focussing the beam to a radius of 17 μm we were able to generate an intensity of 140 kW cm^{-2} within the crystal, which is over 60 times the saturation intensity of Yb:KYW. Through this approach the possible reabsorption losses were adequately suppressed.

The Riis-measured spectrum of the Yb:KYW laser, with a spectral width of 3.8 nm centred about 1042 nm, can be seen in Figure 2.18, and the width of the fringe-resolved intensity autocorrelation was measured to be 536 fs (seen in Figure 2.19). Assuming a sech$^2(t)$ pulse intensity profile this corresponds to an actual pulse duration of 305 fs. Furthermore an RF spectrum confirmed the 1-GHz pulse repetition frequency (inset, Figure 2.19). These results were comparable to other 1-GHz sources at the time, save for the far-greater efficiency, which our system exhibited.

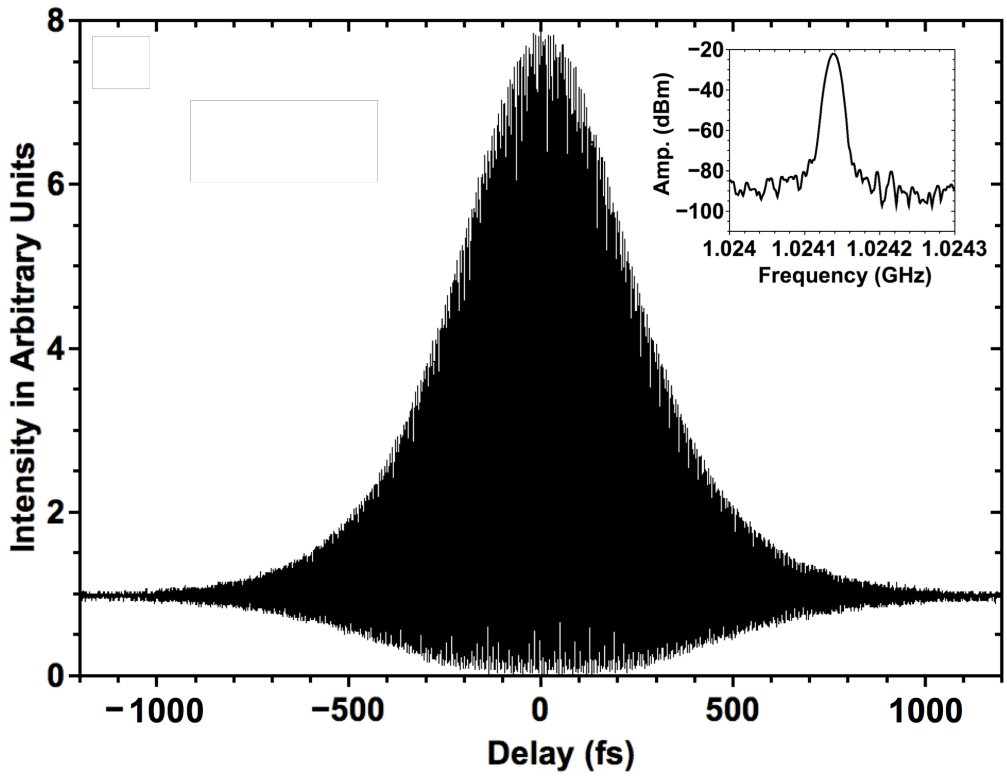

Figure 2.19: A fringe-resolved intensity autocorrelation of the Yb:KYW pulses. The full-width, half-maximum delay was 536 fs corresponding to 305 fs.

2.5. Analysis of the laser stability

The motivation behind developing the 1-GHz Yb:KYW laser was to provide a new, solid-state source for femtosecond frequency-comb metrology, an application which demands exceptional stability. This section describes the implementation of a relative intensity noise (RIN) measurement, which was used to reveal the frequency-domain characteristics of the power fluctuations from the laser.

2.5.1. Noise measurement theory

The output of a laser can be thought of in terms of intensity varying with time, and for a mode-locked laser this is the variance in intensity from pulse to pulse. These fluctuations are known as the relative intensity noise, or RIN. Among the phenomena that give rise to this effect are beam pointing, optical stability, ambient noise, and electrical noise. This collective noise can be represented visually by a power spectral density (PSD) plot, a method of showing the noise per unit-frequency interval in relation to the mean signal strength.

By using the following method we can find the general form of the PSD [91]

beginning with the Fourier transform equations for a time-dependent function $h(t)$:

$$H(\omega) = \int_{-\infty}^{\infty} h(t) e^{i\omega t} dt \tag{2.7}$$

$$h(t) = \frac{1}{2\pi} \int_{-\infty}^{\infty} H(\omega) e^{-i\omega t} d\omega. \tag{2.8}$$

If we replace the frequency term ω as $2\pi f$ we get

$$H(f) = \int_{-\infty}^{\infty} h(t) e^{2\pi i f t} dt \tag{2.9}$$

and

$$h(t) = \int_{-\infty}^{\infty} H(f) e^{-2\pi i f t} df. \tag{2.10}$$

Using Parseval's theorem, which states that the energy contained in a signal is equal in both time- and frequency-domains [91], we can write

$$E_{TOT} = \int_{-\infty}^{\infty} |h(t)|^2 dt = \int_{-\infty}^{\infty} |H(f)|^2 df. \tag{2.11}$$

As the energy in both domains is identical, the power spectral density – in the frequency-domain – can be thought of as the combined power of positive and negative frequencies

$$P_h(f) = |H(f)|^2 + |H(-f)|^2 \tag{2.12}$$

in the range $0 \leq f \leq \infty$.

As most of the work presented is analytical in nature, the results are from discrete Fourier transforms of the finite number of points available. If we assume a quantity h_j containing N points we can think of the Fourier transform as

$$H_k \equiv \sum_{j=0}^{N-1} h_j e^{2\pi i \frac{jn}{N}} \tag{2.13}$$

which can be normalised using the mean-squared amplitude. The integral of the PSD

from 0 to the Nyquist limit is equal to half of the mean-squared amplitude, and we can normalise using this relation. What we find ourselves with can be integrated over the entire frequency range to give the cumulative noise

$$\Delta h_{CUM} = \left[2 \int_0^{f_{Nyquist}} P_h(f) df\right]^{\frac{1}{2}} \tag{2.14}$$

wherein $P_h(f)$ is our normalised PSD and $f_{Nyquist}$ is the Nyquist limit.

2.5.2. Experimental work and discussion

Since the upper-state lifetime and pump sources differed from more common Ti:sapphire systems, the noise characteristics of the Yb:KYW laser were expected to differ as well. Both the laser and pump diode instantaneous powers were acquired simultaneously using a pair of fast silicon photodiodes, and processed through a 12-bit data acquisition card. These signals can be seen in Figure 2.20.

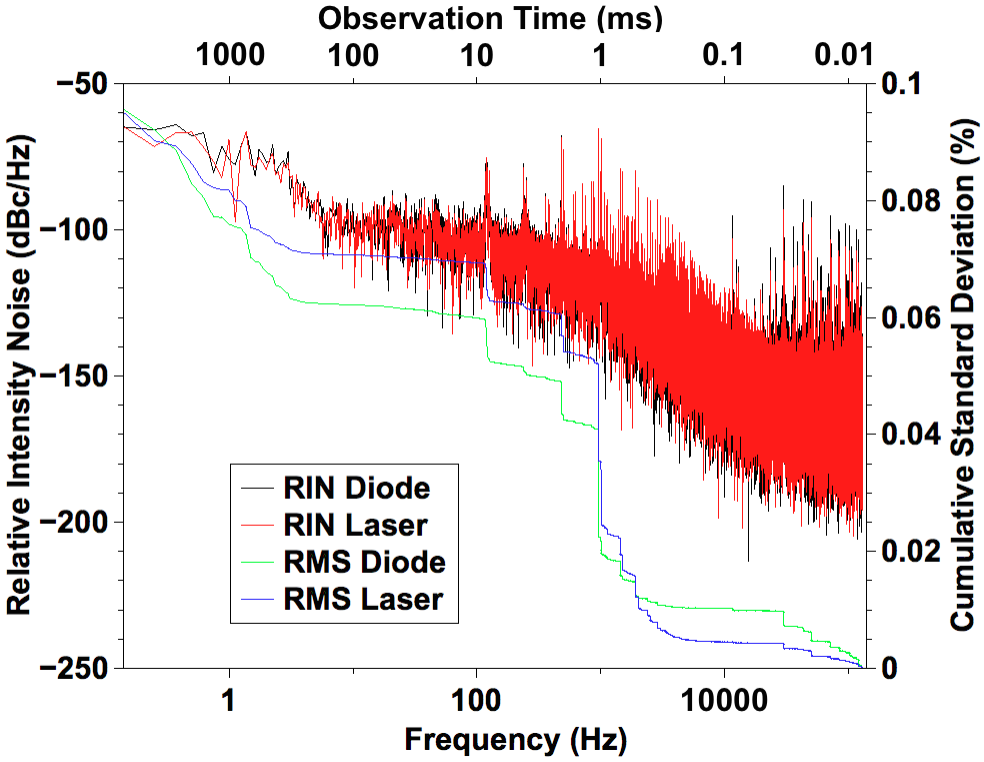

Figure 2.20: The RIN and cumulative standard deviation (the time-domain RMS noise) of the Yb:KYW laser for an 8-s observation time. The black and green lines represent data from one of the identical laser diodes while the red and blue lines represent the Yb:KYW output.

As can be seen, at frequencies below the 1-kHz level the RIN of the Yb:KYW laser exceeds the noise of the pump lasers, whilst at higher frequencies the laser-

diode noise is greater than that of the overall system. By thinking of these results in terms of the observation times instead of the frequencies – frequencies above 1 kHz corresponds to observation times below 1 ms – it can be understood that fluctuations faster than this are not strongly-coupled into the laser due to Yb:KYW's upper-state lifetime of 0.3 ms damping the modulations faster than the timescale. As a result the high-frequency RIN of the laser diodes is not seen in the Yb:KYW laser.

Below 1 kHz the laser noise overwhelms the noise of the laser diode: this implies noise arising from other contributions. So, at an observation time greater than 1 ms the acoustic and ambient noise couple into the cavity through the optomechanics increasing the noise to levels above that of the pump lasers. Above 1-second-long observation times the noise of both the diode and laser system are nearly identical at less than 0.1%; comparable to Ti:sapphire laser systems. Greater than 1-s times see an increase in the RMS noise, as well, thought to be due to temperature fluctuations.

2.6. Supercontinuum generation

To assess the possibility of f-2f referencing and a CEO-locked frequency comb the light was coupled into a 3-m PCF (NKT SC-3.7-975) with a 3.7 $\pm$0.3-μm core for broadening through self-phase modulation. Light was coupled in and out using a pair of ThorLabs C240TME-B aspheric lenses (f = 8 mm). A long focal-length lens was placed in the beam path to expand the beam to better fill the lens. A simulation based on the model introduced in Section 1.3 was used to predict the effective broadening of the Yb:KYW laser spectrum seen in Figure 2.21 [14]. The simulation parameters were as follows: average coupled power = 400 mW; γ = 0.018; τ_p = 278 fs, for a sech$^2(t)$ profile; L = 3 m. After achieving suitable coupling efficiency (70%) the output spectral bandwidth was measured to be >400 nm, and the results are shown in Figure 2.22.

Both experiment and theory indicated that the realisation of an octave-spanning supercontinuum was unlikely without further refinement of the laser. For this reason our efforts moved to a redesign of the laser cavity operation at a lower pulse-repetition frequency, thereby shortening the pulses, with the expectation of generating the desired octave-spanning spectrum from broadening in a PCF.

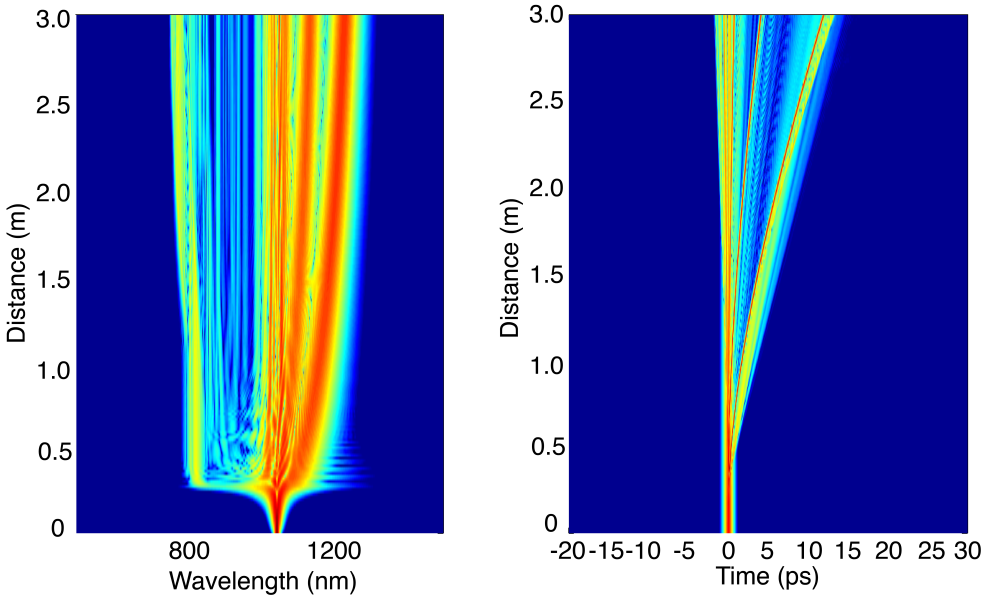

Figure 2.21: The predicted spectral (left) and temporal (right) broadening of the pulses from the 1-GHz Yb:KYW laser as they pass through a 3-m PCF. The extent of the broadening can be seen to form a supercontinuum from 800-1200 nm.

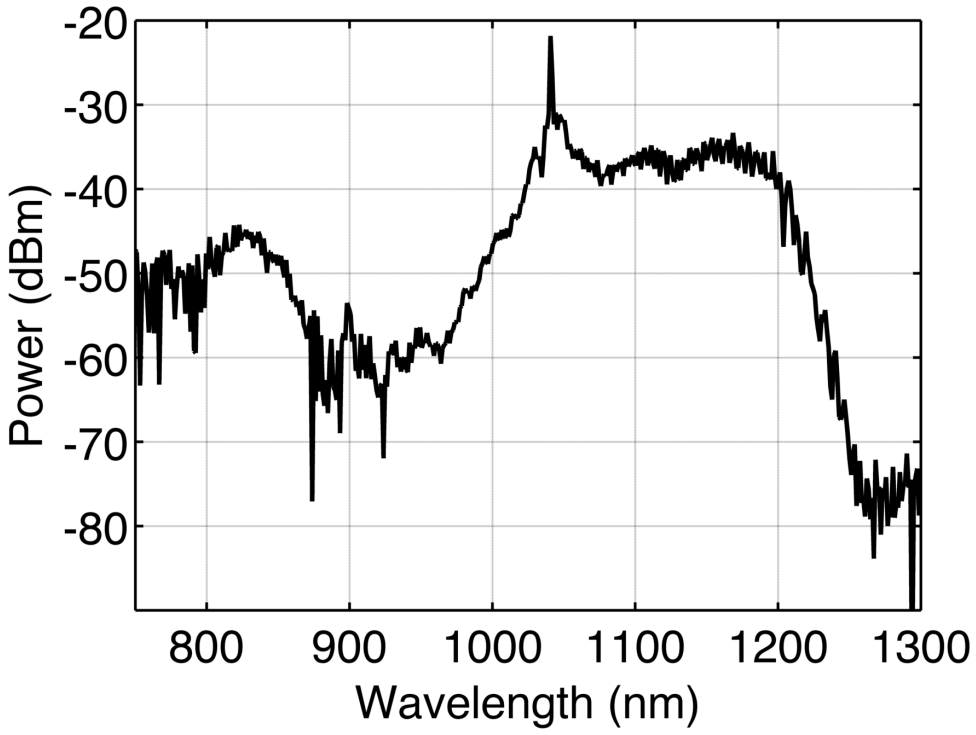

Figure 2.22: The experimentally recorded spectrum of the 1-GHz Yb:KYW laser broadened in a 3-m PCF

2.7. Conclusions

I have presented in this chapter a SESAM-mode-locked highly-efficient 1-GHz Yb:KYW laser operating with a 3.8-nm spectrum, transform-limited 278 fs pulses, and 770

mW average power. This laser achieved a record optical-to-optical efficiency of 61% and a slope efficiency of 67%. RIN measurements were performed and showed that the properties of the system at observation times longer than 1 second were comparable to those of Ti:sapphire systems. A supercontinuum from 800 nm to 1200 nm was obtained by passing the laser light through a PCF.

The system achieved excellent optical-to-optical efficiency – exceeding the performance of all previous systems – with several-hundred femtosecond pulse durations, but these were found to be too long to allow for octave-spanning supercontinuum generation from broadening in a PCF. With increased resources allowing for greater pump power the laser may have achieved short enough pulse durations for an octave. Furthermore, given resources enough, a positive-pressure low-grade clean room environment built to damp external vibrations would have decreased the RIN of the laser as well as the number of times cleaned.

In order to surmount the issues present the cavity was redesigned for a lower repetition frequency, as detailed in the following chapter.

3. Construction and repetition frequency stabilisation of a 666-MHz Yb:KYW femtosecond laser

3.1. Introduction

In Chapter 2 I introduced a highly-efficient 1-GHz system generating 278-fs pulses and capable of producing a supercontinuum from 800 to 1200 nm. A simulation based on modelling by Dudley, *et al* [14] indicated that such pulse durations are too long for the spectrum to broaden sufficiently – that is, to reach a full octave – and to maintain coherence across the full supercontinuum bandwidth. In order to address this problem the laser was redesigned to operate at a lower repetition frequency, with the expectation that the pulse intensity would increase proportionately as well for a constant average power. These higher peak pulses should, in turn, increase the level of self-phase modulation (SPM) in the gain medium, allowing shorter pulses to be generated, which themselves should be more suitable for broadband supercontinuum generation and more efficient Raman single-soliton generation, which leads to a greater spectral coherence of the pulses.

Such a supercontinuum is necessary to permit a strong beat note to be generated via an f-2f interferometer in order to stabilise the f_{CEO} of the laser. Unless the repetition frequency is stabilised, controlling the carrier-envelope offset (CEO) signal will fail to produce a stable comb because of noise contributions from the repetition rate. This can be seen in the description of each individual frequency-comb mode:

$$f_{mode} = N f_{rep} + f_{CEO}. \tag{3.1}$$

where N is the comb mode number. As can be seen the contributions from f_{rep} have a much greater effect on the frequency of the N^{th} comb mode than f_{CEO} does: locking f_{rep} is absolutely necessary for comb stabilisation. Work to stabilise the repetition rate was therefore prioritised over broadening the laser spectrum.

3.2. 666-MHz Yb:KYW laser design

Reducing the repetition frequency of the 1-GHz laser cavity to 666 MHz was expected to increase the peak pulse power by 50%, which was considered potentially sufficient to improve the coherence of the supercontinuum spectrum while still representing a high-repetition-rate laser comb. As before, a model of the cavity was produced using LCAV to ensure that the necessary characteristics for stable mode-locked operation would be maintained, including the spot size in the crystal and sufficient astigmatic compensation necessary due to the placement of the gain material at Brewster's angle.

Using the values from the LCAV simulation (the result of which can be seen in Figure 3.1) and the same z-fold arrangement as was used as in Figure 2.10 the new cavity was built, as shown in Figure 3.2.

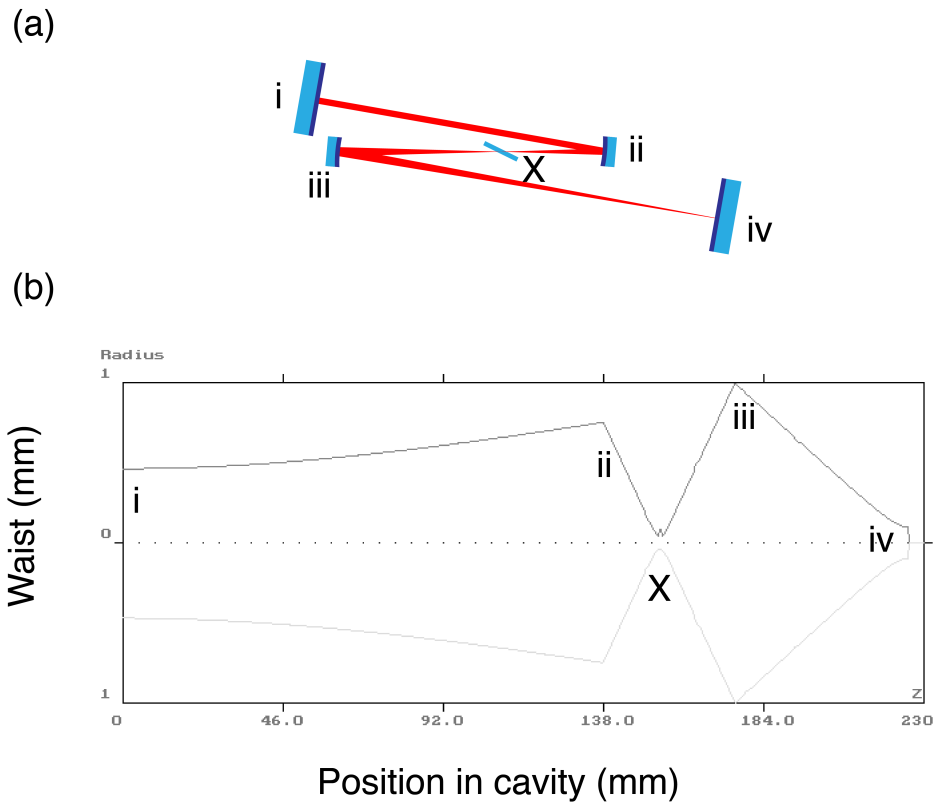

Figure 3.1: (a) Initial 4-mirror cavity design for 666 MHz; (b) the modelled beam propagation in the designed cavity. The close matching of both the tangential and sagittal planes is seen. The mismatch at the smallest radius is due to passage through the Yb:KYW crystal, which is off-axis. Values are in mm.

Many of the components were identical to those used in the 1-GHz cavity, though

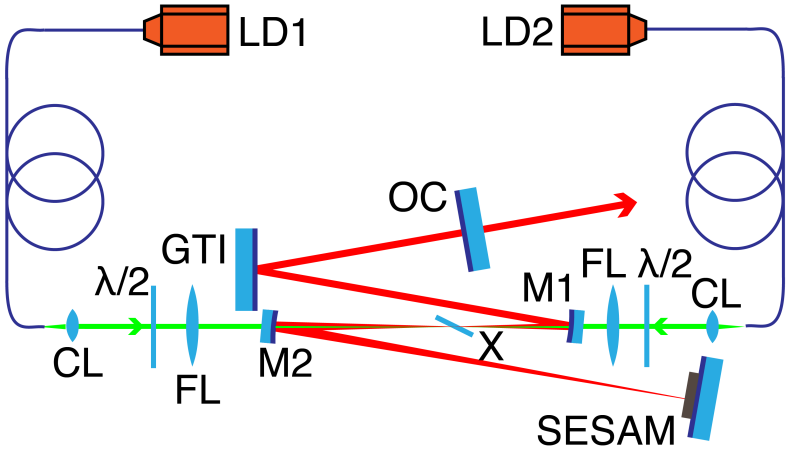

Figure 3.2: The design of the 666-MHz laser cavity, which was very similar to the 1-GHz laser in design. Laser diodes (LD) emit 981 nm light (represented by green) that passes through coupled fibres before passing through collimating lenses (CL), half-wave plates ($\lambda/2$), focussing lenses (FL), and the cavity's folding mirrors (M1 and M2) before meeting in the crystal (X) with a focussed spot size of 17 μm. At one end of the cavity the output coupler (OC) is situated; at the other end lies a semiconductor saturable absorber mirror (SESAM).

one of the folding mirrors had to be exchanged for one with a larger radius of curvature, and the corresponding focussing lens had to be moved to compensate for the change in focussing power. The identifying information of the included optics and their distances can be seen in Table 3.1

3.3. Characteristics of the 666-MHz cavity

In this modified system a 3% output coupler was used for stable modelocking, which was found to achieve the correct fluence (calculated to be approximately 600 μJ cm^{-2}) while using a 45-μm spot size on the SESAM. The average output power depended on the exact cavity alignment, but the laser was often stably mode-locked between 700 and 750 mW. At the higher end of that range the laser's spectral bandwidth was measured using a Riis to be 5 nm, evident from the spectrum in Figure 3.3. An autocorrelation of the pulses was also obtained (shown in Figure 3.4) using a Michelson-interferometer fringe-resolved intensity autocorrelator: after correcting for a sech^2 profile, the duration of the pulses was found to be 220 fs. The duration-

Cavity element	Value
Output coupler	3% transmission
Distance between output coupler and GTI	40.2 mm
GTI GDD	1300 fs^2
Distance between GTI and M1	97.7 mm
M1 radius of curvature	-30 mm
Half-angle of M1	4°
Distance between M1 and crystal	16.18 mm
Spot size in crystal	17 μm
Distance between crystal and M2	20.9 mm
M2 radius of curvature	-30 mm
Half-angle of M2	5°
Distance between M2 and SESAM	50 mm
Spot size on SESAM	45 μm

Table 3.1: The components, the distances between them, and necessary characteristics required for construction of the 666-MHz laser cavity. Labels refer to those seen in Figure 2.10.

bandwidth product was 0.305, very close to the ideal of 0.315 for $sech^2$ pulses. The difference can be understood as a result of error in measuring the FWHM of both spectrum and autocorrelation due to poor signal-to-noise on the spectrum arising from low incident power.

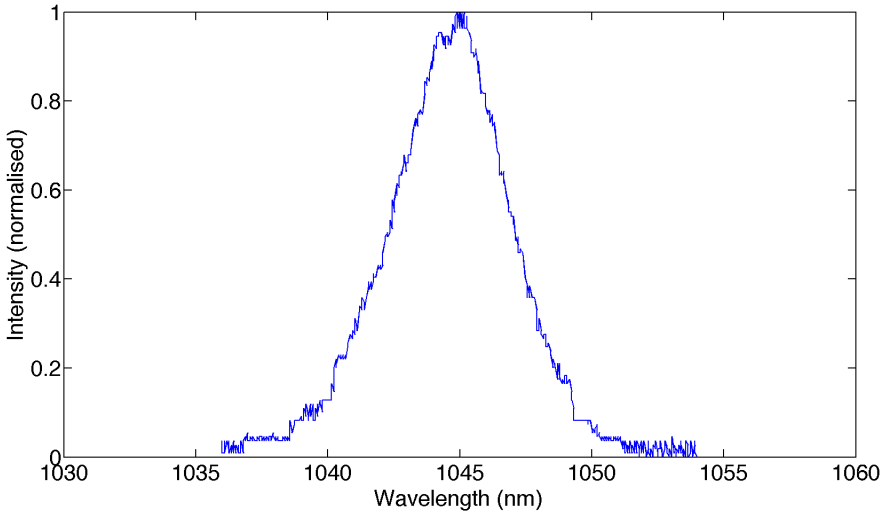

Figure 3.3: Spectrum of the 666-MHz cavity with a FWHM bandwidth of 5 nm.

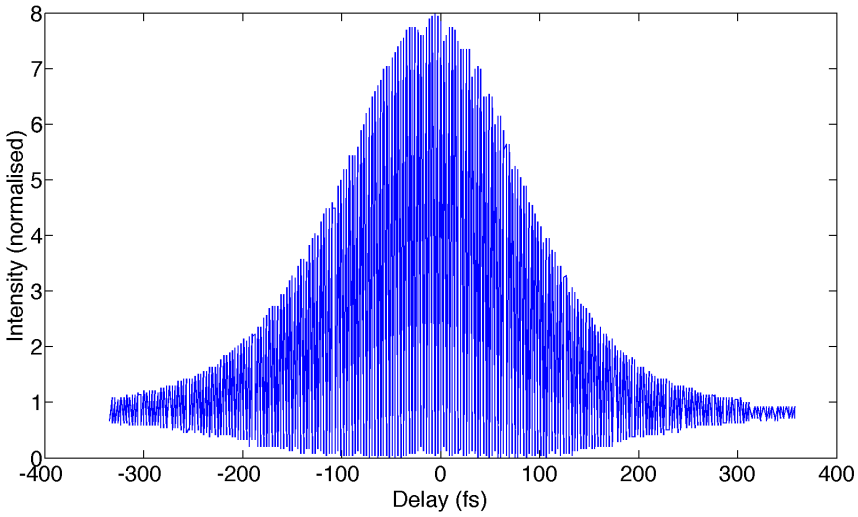

Figure 3.4: Fringe-resolved intensity autocorrelation of the 666-MHz cavity. Assuming sech^2 pulses the FWHM Yb:KYW laser pulse duration was 220 fs.

3.4. Locking the repetition rate

3.4.1. Design of the locking apparatus

Changes in the length of the laser cavity due to thermal variations, relaxation of optomechanics, and acoustic vibrations, among other effects, mean that locking the repetition rate is critical to achieve a stable frequency comb: it can vary quickly and has a great impact on the overall stability of the laser mode frequencies, the locking of the CEO frequency, and the eventual usefulness of the laser for frequency measurement. The effects of this noise can be understood by first looking at the laser modes.

The frequency of the N$^{\text{th}}$ laser mode, f_{mode}, is

$$f_{mode} = N f_{rep} + f_{CEO}. \tag{3.2}$$

Now if we look at the repetition rate

$$f_{rep} = \frac{c}{2L} \tag{3.3}$$

and differentiate to show the variance of the length of the cavity, we come to

$$\Delta f_{rep} = \frac{-\Delta L c}{2L^2}, \tag{3.4}$$

which, when we substitute for L, leaves us with a method for defining our frequency change as

$$\Delta f_{rep} = \frac{-2f_{rep}^2 \Delta L}{c}. \tag{3.5}$$

The error of an individual frequency mode can then be understood as

$$\Delta f_{mode}^2 = (N\Delta f_{rep})^2 + (\Delta f_{CEO})^2, \tag{3.6}$$

The contribution of cavity-length fluctuations to the absolute uncertainty in the position of the central laser mode is therefore,

$$\frac{c}{f_{rep}\lambda} \times \frac{2f_{rep}^2 \Delta L}{c} = \frac{2f_{rep}\Delta L}{c} \tag{3.7}$$

It is necessary to know how much elongation or contraction of the laser cavity will be necessary to stabilise the cavity within a given range. In order to stabilise a single mode of the laser to 0.1 radian, the uncertainty contributions from the repetition rate must be less than or equal to

$$\Delta f_{mode} = \frac{0.1}{2\pi} \times f_{rep} = 10.6 \text{ MHz}. \tag{3.8}$$

This corresponds to a change in the length of the cavity by 8.3 nm, which, for a 10-μm piezo, is approximately 0.1 V, and indicates that a single piezo should, once the system is locked, be able to correct fluctuations with sufficient precision.

PZTs were installed on both the GTI mirror (14-μm displacement) and the SESAM (9-μm displacement) in order to achieve the necessary range of motion and provide the possibility of using a cross-over circuit to drive one at high frequencies and the other at lower frequencies, but across a longer range. The placement of both can be seen in Figure 3.5.

By using a thin wedge in the output beam path a small portion of the light was redirected at a focussing lens and onto a fast Si photodetector with a frequency response of up to 1 GHz (Hamamatsu S5973-01). The output signal passed through an 18-dB amplifier (MiniCircuits ZFL-1000+), and into a double-balanced mixer

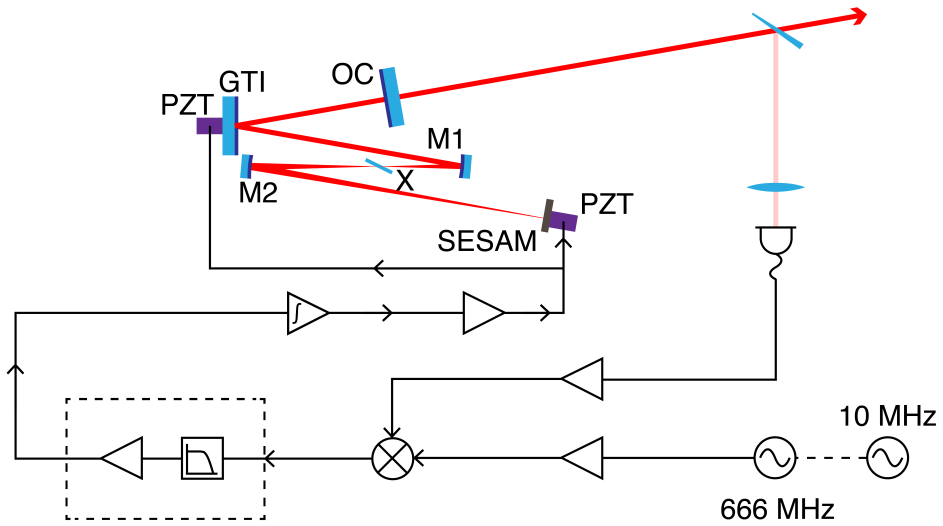

Figure 3.5: The schematic of the locked 666-MHz Yb:KYW system. A small portion of the laser light, 4%, was picked-off from the laser output and was incident on a fast photodiode. The signal passed through an amplifier and into a mixer with the output from a frequency synthesiser, which was, in turn, stabilised using the 10-MHz output from a Rb source. This then passed through a home-built amplifier (bounded by the dashed line), through an integrating amplifier, and further amplification before the signal was transmitted to the two PZTs controlling the linear position of both the GTI mirror and the SESAM. Pump diodes are not shown, for clarity.

(MiniCircuits ZX05-C24 S+) for heterodyne beating. Simultaneously a signal very close in frequency to the repetition rate was produced by a synthesiser (Agilent 8664A), passed through a 20-dB amplifier (MiniCircuits ZFL-500LN), and into the mixer's other channel. From there the signal was amplified and filtered using a home-built amplifier, described later in 3.4.2. Both signals were amplified to achieve the 7 dBm necessary to properly operate the mixer and maintain the lower-noise characteristics of operating a synthesiser at lower output powers.

The repetition rate was then controlled by an integrating amplifier with PI control and passed through a high-gain amplifier (Falco 20x amplifier) to extend the voltage range to a suitable level for PZT control. It was from there that the output was passed to the two PZTs.

3.4.2. Integrating amplifier design

The original plan for repetition rate locking was based on an in-house amplifier design that had proved to be successful with other repetition-rate locked systems. Over the course of working with the system many changes were made to better suit

the particular application. The circuit diagram can be seen in Figure 3.6.

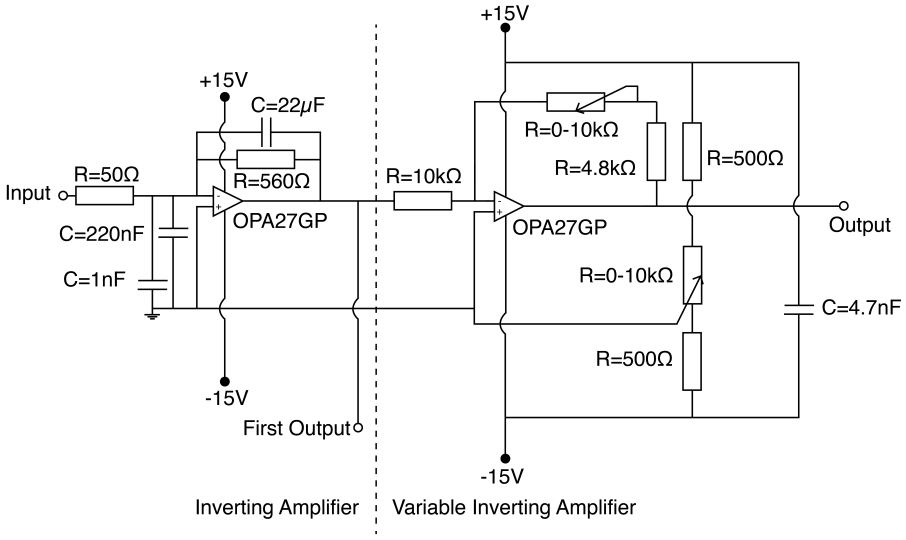

Figure 3.6: Circuit diagram of the amplifier used to condition the repetition rate signal for locking. The system consisted of two inverting amplifiers, the first a fixed-gain amplifier with low-pass filtering (corner frequency of 25 kHz) and the second a variable gain amplifier. in the second of the two amplifiers the variable resistor orientated horizontally acted at the main gain whilst that orientated vertically was the DC offset.

The amplifier had serious noise issues from the start; it provided a series of extra frequencies on top of the lock signal. In order to address these problems a 220 nF and a 1 nF capacitor were placed between the input of the first amplifier and ground to act as low-pass filters. A 50 Ω resistor allowed for the correct impedance matching. The integrating amplifier stage comprised a 560 Ω resistor and 22 μF capacitor had a 3-dB reduction at near 25 kHz.

This was then passed into another inverting amplifier with variable gain settings. The 4.8 kΩ resistor prevented the gain from ever passing below 0.5 V and the additions of two 500 Ω resistors to either side of the other variable resistor were to reduce the total gain of the amplifier to $\frac{1}{20}^{th}$ of the original. A further grounding of the positive input of the op-amp was part of an effort to reduce noise by creating a virtual ground.

Eventually the entire system was grounded to its case, the case was shielded against RF interference, and a switching mains power supply was replaced with 9-V batteries.

3.4.3. Repetition frequency locking

The initial locking signal lacked any long-term stability, suggesting environmental factors had to be assessed. The first step was to place the entire laser in a box to prevent in-lab air currents from having an adverse effect on the laser's stability. The box was then lined with foam to prevent ambient temperature changes and the table floated to reduce acoustic noise contributions. A 320-second acquisition of the laser power was performed with the repetition rate free-running, the cumulative standard deviation (CSD) and relative intensity noise (RIN) results of which are visible in Figure 3.7.

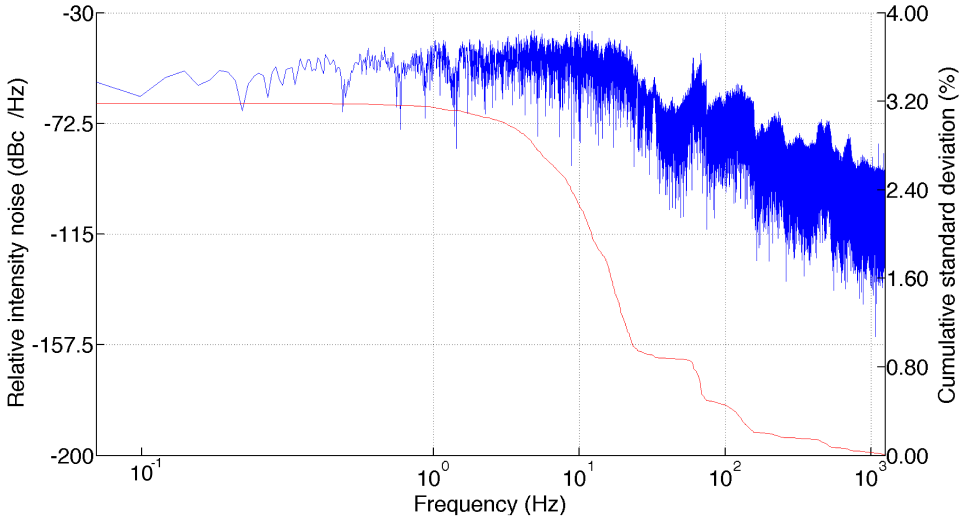

Figure 3.7: The cumulative standard deviation (red) and relative intensity noise (blue) of the laser output over 320 seconds while the repetition-frequency-locking circuit was off.

The repetition-rate lock was then engaged and another measurement was performed, the results of which can be seen in Figure 3.8. The lock was seen to reduce the noise characteristics of the laser at low frequencies, as a changing cavity length leads to power fluctuations, but there were still very visible spikes near 50 and 100 Hz, as well as higher-frequency noise present. The main peaks being where they were (≈100 Hz) led to the conclusion that acoustic noise in the cavity was playing a larger role than previously thought, and steps needed to be taken to reduce or remove this noise.

Firstly further efforts to remove noise-making components were implemented: laser drivers and other systems with transformers were removed from the area to try

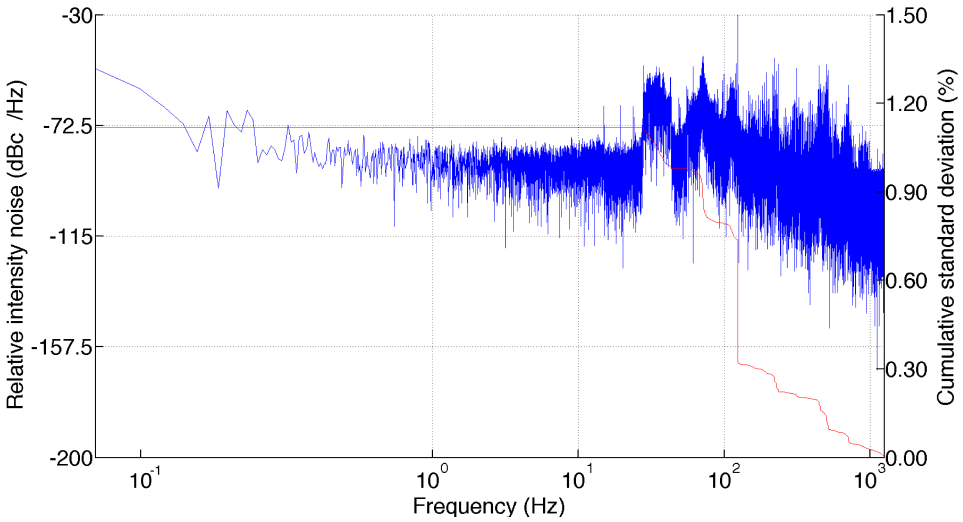

Figure 3.8: The cumulative standard deviation (red) and relative intensity noise (blue) of the laser output over 320 seconds while the repetition-frequency-locking circuit was on. Immediate reduction of noise and error of the signal can be seen, though there are still substantial contributions to noise in the acoustic range.

to alleviate the symptoms. Further attempts at electrical isolation – greater shielding and improved grounding – were also introduced, but without any appreciable improvement.

The search for the noise-making components came to an end when the mounts in the cavity were reassessed: due to the space constraints of the original laser design the mirrors had been set into cantilevered arms fixed to the fronts of standard mirror mounts. These arms had become, essentially, tuning forks.

To address the noise created by the movement of these arms copper weights (estimated mass of 100 g) were placed on the arms to damp the possible modes generated, explained in Figure 3.9 and shown in Figure 3.10. Upon completion, the intensity was measured once again.

As can be seen in Figure 3.11 this alteration greatly reduced the high-frequency contributions to noise and reduced the entire noise profile. There remained contributions to noise at 50 Hz – due to mains hum – and at some of the higher-order acoustic modes because the added weight could not entirely damp the frequencies present. More careful component choice and the use of a Voltage reference chip across the DC-bias of the second amplifier could reduce this further. The RMS noise was reduced from 1.1% to 0.50% over 320 s.

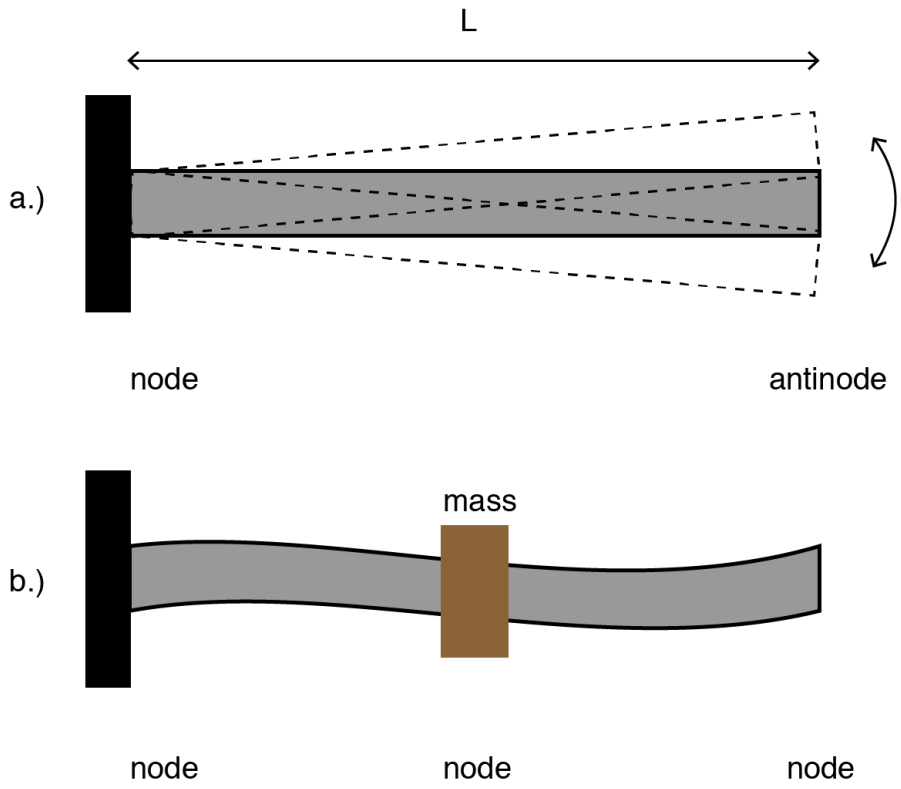

Figure 3.9: The cantilever arms before (a) and after (b) damping. If a mass is placed at L/2 away from the ends of the cantilever this forces that point to be a node, which then means that the lowest normal mode of the system is one with a node at the free end of the cantilever, significantly reducing the amplitude.

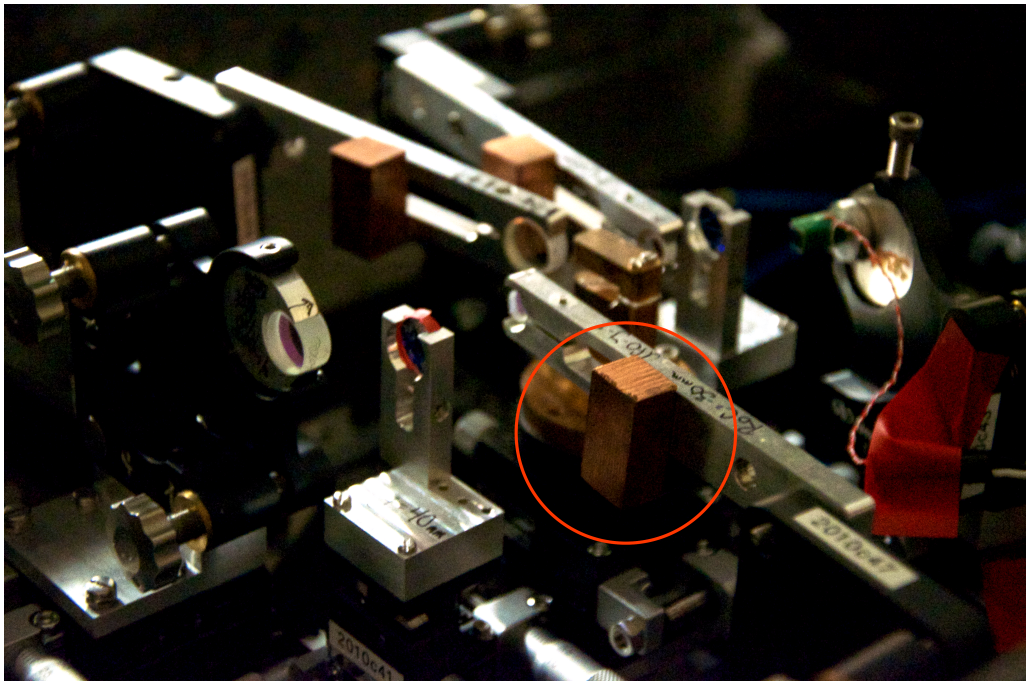

Figure 3.10: The implementation of damping. A mass is circled in red.

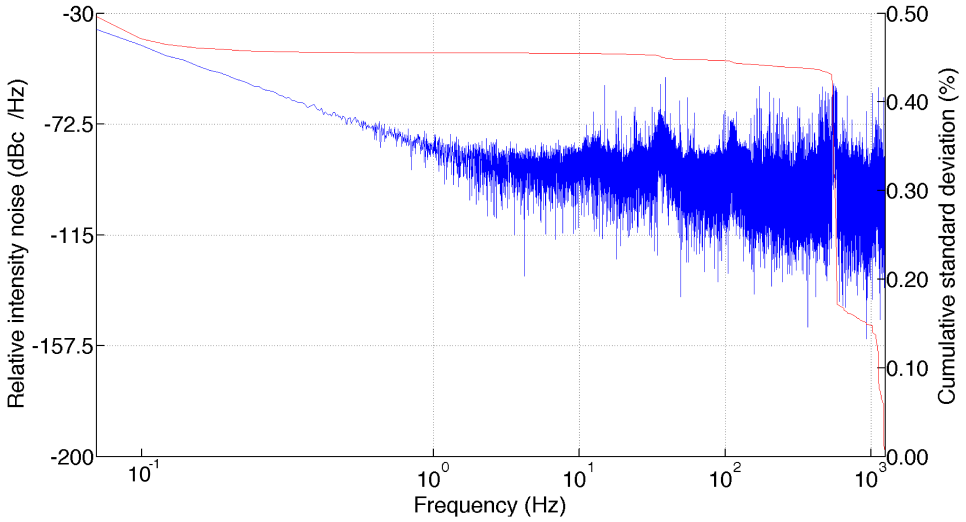

Figure 3.11: The cumulative standard deviation (red) and relative intensity noise (blue) of the repetition-frequency-locked laser output over 320 seconds after damping of the cantilever mounts had been performed. There is an overall flattening of the noise profile and a removal of many of the noise spikes. The remaining noise spike could have been the resonance of the PZTs in the cavity.

3.5. Conclusions

I have presented work to design, characterise, and lock the pulse repetition frequency of a 666-MHz Yb:KYW laser. Noise characteristics of the system showed large levels of acoustic noise after isolating the laser from external influences and steps were taken to dampen the remaining acoustic noise caused by vibrations of the mirror mount arms. Due to the large level of noise in locking f_{rep} the laser was not considered viable for self-referencing or stable comb generation, and thus only preliminary work was performed to begin launching the light into a supercontinuum.

From the failings of this system many things could be learned. Perhaps foremost was the mechanical: were this system to be built again the mounts would have been designed very differently to reduce noise. Instead of long cantilevered arms, low-profile posts would be used to ensure that vibrations would be less of a problem. A thermal management system for the box would have been integrated from the start, as well as early steps to physically isolate the laser. Furthermore, movement from switching power supplies to battery power would have further reduced noise at 50 Hz and its harmonics. The removal of the large connection loops between equipment could have reduced the electronic noise of the system and a vibration-damped

environment to reduce more forms of environmental noise would have improved the acoustic noise characteristics of the system.

The move to 666 MHz had been one based on a hope to retain the high pulse repetition frequencies while increasing the peak power of the laser. Given the chance to repeat this experiment I would have liked to decrease the repetition frequency further in an attempt to achieve an octave-spanning supercontinuum.

Had the laser noise been lower, steps would have been taken to shorten the pulses, as demonstrated by Pekarek, *et al*, performed [92] by using a short length of PCF to broaden the pulse and prism pairs to compensate for linear chirp, thus compressing the pulses to a fraction of their original length. This would have also allowed the initially long pulses of this system to be of a duration suitable (<150 fs) to produce a spectrally-coherent supercontinuum.

4. ^{87}Rb stabilisation of a 375-MHz Yb:fibre femtosecond frequency comb

4.1. Introduction

Due to the long pulse durations and lower-than-needed peak power available from the 1-GHz and 666-MHz Yb:KYW lasers for the purposes of referenced comb generation another method was necessary to generate and lock the f_{CEO} beat. We moved to a femtosecond Yb-doped fibre laser due to its inherently broad spectrum, which supported shorter pulses, which could easily be compressed using suitable dispersion management.

In this chapter I first describe the state of fibre-laser frequency combs from their inception before discussing the properties of Yb-doped fibres. I then review the various methods for modelocking a fibre laser for femtosecond pulse generation and the specific techniques that can be used with Yb:fibre. Moving from there to the design and construction of the Yb:fibre laser sets the stage for introducing the experimental work. The steps taken to stabilise the pulse-repetition frequency and the resulting noise characteristics are then discussed. This repetition-frequency-locked oscillator was spectrally broadened as a means to locking its carrier-envelope offset frequency to a rubidium optical frequency standard.

I discuss work done designing and building a ^{87}Rb-stabilised external cavity diode laser (ECDL) system, the theory behind its operation, and efforts undertaken to directly control the CEO-beat frequency by use of this device. Amongst the methods attempted were direct current control of one of the pump laser diodes, feed-forward locking using an acoustooptic modulator, and direct control of the intracavity beam through movement of an integrated filter. My successes with the last method are discussed, as well as methods to further improve lock control. Noise measurements and a performance analysis of the final system are presented.

4.2. Review of fibre-laser frequency combs

Passively mode-locked ultrafast fibre lasers were first characterised in 1992 by Hofer *et al* at the Technische Universität Wien using Nd-doped fibres with pulse durations of 50 fs and about 15 mW cw power with optimal dispersion compensation [93]. The first analysis of Yb-doped fibres appeared in 1998 when Arkwright *et al*, at the Australian Photonics Cooperative Research Centre, explored the nonlinearities inherent in such fibres between the wavelengths of 514 nm and 1570 nm [94]. Their work was concentrated largely on the promise of ms optical switching at telecommunications wavelengths, and while it focussed little on achieving short pulse durations it was the first to look at the nonlinear response of Yb-doped fibres to intensity change.

Abedin *et al* at MIT observed self-stabilisation of a ring-cavity Er:fibre laser with 125-fs pulses and a pulse-repetition frequency of 220 MHz with average power of nearly 80 mW in 2002 [95], and Rauschenberger *et al* at JILA in Colorado showed that these pulse-stretched, Er:fibre lasers can be directly controlled by Ti:sapphire combs thereby allowing for frequency metrology up to 1.55 μm. By controlling the pump laser's power they were able to induce feedback to control the CEO-offset with a 355 kHz jitter [96]. Work on utilising the tunable range of SESAM-mode-locked Yb:fibre lasers was presented by Okhotnikov *et al*, which was achieved by tilting a dichroic high reflector to change the wavelength-dependent finesse of the cavity [97]. They were able to generate pulses over a 90-nm tuning band with pulse durations between 1.6 ps and 2 ps.

Washburn *et al* at NIST in Colorado brought self-referenced fibre lasers from conception to reality using f-2f referencing of an Er:fibre laser. Using a highly-nonlinear optical fibre the bandwidth was broadened to a range allowing for comparison to comb modes at 1100 nm and 2200 nm. The pulse duration was approximately 130 fs at a repetition frequency of 50 MHz, whilst the f_{CEO} beat signal was stabilised using an RF standard [98]. Work by Orsila *et al* at the Optoelectronics Research Centre on mode-locked Yb:fibre lasers realised 500-fs pulses at 95 MHz by using suitable intracavity dispersion management [99].

In 2006 work by Zhou *et al* at Cornell University demonstrated a Yb:fibre laser

with pulse durations of approximately 500 fs with a pulse-repetition frequency of 1.5 GHz through harmonic modelocking (HML) – an integer number of evenly-spaced pulses circulate through a ring cavity leading to a shorter pulse repetition frequency than would be possible otherwise with the available cavity length [100]. The following year saw papers by Chong *et al* [101], Pal *et al* [102], and Hartl *et al* [103] all on pulsed Yb-doped fibre lasers. The first focussed largely on high pulse energies with normal dispersion: using nonlinear polarisation evolution (NPE) they were able to produce 20 nJ pulses, dechirped to less than 200 fs, at a repetition rate of 12.5 MHz [101]. The second paper detailed the construction of the first self-referenced Yb:fibre laser comb with 120-to-150-fs pulses generated at 90 MHz using a saturable absorber, and average powers of up to 1.4 W. By passing the output light through a dispersion micro-managed holey fibre they were able to broaden the laser output to between 400 nm and 1300 nm, allowing for frequency doubling of the fundamental to 523 nm. This work produced a locked f_{rep} with a 0.5-MHz RMS deviation and f_{CEO} with 1.6-MHz RMS deviation (both at 10-second gate times) [102]. The third discussed the generation of 95-fs pulses at a pulse repetition frequency of 125 MHz and peak power of 230 MW, mainly for purposes of ionising noble gasses, but also demonstrating the high powers that can be generated using Yb:fibre [103].

Work in 2008 led to even more results from Yb-doped fibre combs. Kivistö *et al* at the Tampere University of Technology in Finland worked on acoustooptic wavelength tuning of Yb:fibre lasers with a range of over 30 nm and found fast tuning on the order of 15 μs with an accuracy of 0.1 nm [104]. Chong *et al* furthered exploration into the dispersive properties of Yb:fibre lasers with sub-200-fs pulse durations in a normal-dispersion regime [105]. Herda *et al* generated 89-fs pulses without an external bulk compressor at an average power of 1.5 mW – the shortest achieved without bulk compression [106]. The shortest pulses achieved with Yb:fibre lasers were 28.3 fs in duration and created by Zhou *et al* at the Japanese National Institute of Advanced Industrial Science and Technology. Their work had a broad spectrum from 1000 nm to 1120 nm, with an 80-MHz pulse repetition frequency,

and dispersion management through intracavity prisms [107].

Work continued on improving the performance characteristics of Yb:fibre lasers. In 2009 Braje *et al* at NIST built a cw-seeded Yb:fibre laser achieving a broad comb with the main modes separated by 2 THz, and intermediate modes spaced by 10 GHz through the use of a monolithic cavity comprised of a 5.2 cm segment of dispersion-flattened fibre with mirror-coated end faces [108]. Schultz *et al* engaged in research towards more accurate tuning of Yb:fibre lasers with an intracavity interference filter. Through this method they obtained 108-fs pulses over a range between 1015 and 1050 nm [109]. Wilken *et al* pursued high repetition rates in their work, achieving a 570-MHz pulse repetition frequency without the earlier method of HML used by others. They reported 50-fs pulses and a spectral bandwidth of up to 70 nm [110].

Since their inception much had been accomplished to characterise and build varying Yb:fibre frequency combs to a point where a suitable system could be built for the purposes of creating a ^{87}Rb-referenced Yb:fibre frequency comb system. A summary of fibre comb results is shown in Table 4.1.

4.3. Yb-doped fibre lasers

Fibre lasers have many attractive properties for stable modelocking and, therefore, frequency comb generation. These lasers are based on a length of glass fibre with a doped core containing a rare-earth ion (neodymium, erbium, ytterbium, holmium, thulium or praseodymium), and have been proven useful for mode-locked lasers with high power stability. In this section I will elucidate these qualities as well as several common methods of pulse generation before moving on to the design and construction of the Yb:fibre laser used for comb generation.

4.3.1. Properties of Yb:fibre

Yb-doped fibres are generally composed of either silicate or phosphate glass, though the former is far more likely. The choice of glass is vital to ensure transparency at the emission wavelengths of Yb^{3+} between 1 μm and 1.1 μm. Silicate glasses also have advantages in production and handling as they are inexpensive to produce

Ref.	Year	Material	Mode-locking	P_{out}	τ_P	f_{rep}
[93]	1992	Nd:fibre	NPE	15 mW avg.	50 fs	N/A
[94]	1998	Yb:fibre	N/A	14 mW cw	N/A	N/A
[95]	2002	Er:fibre	NPE	80 mW avg.	125 fs	220 MHz
[96]	2003	Er:fibre	NPE	45 mW avg.	500 fs	33.33 MHz
[97]	2003	Yb:fibre	SESAM	3 mW avg.	1.6 ps	N/A
[98]	2004	Er:fibre	Fo8	3 mW avg.	130 fs	50 MHz
[99]	2004	Yb:fibre	SESAM	1 mW avg.	1.5 ps	140 MHz
[100]	2006	Yb:fibre	HML	45 mW	500 fs	1.5 GHz
[101]	2007	Yb:fibre	ANDi	275 mW avg.	200 fs	10 MHz
[102]	2007	Yb:fibre	SA	1.4 W avg.	150 fs	90 MHz
[103]	2007	Yb:fibre	similariton	3 kW avg.	95 fs	136 MHz
[104]	2008	Yb:fibre	SESAM	60 mW avg.	360 fs	40 MHz
[105]	2008	Yb:fibre	ANDi	N/A	150 fs	N/A
[106]	2008	Yb:fibre	SESAM	1.5 mW	89 fs	66 MHz
[107]	2008	Yb:fibre	NPE	56 mW avg.	28.3 fs	80 MHz
[108]	2009	HNLF	N/A	N/A	N/A	N/A
[111]	2009	Er:fibre	N/A	20 mW avg.	100 fs	100 MHz
[109]	2009	Yb:fibre	NPE	147 mW avg.	108 fs	38.7 MHz
[110]	2009	Yb:fibre	NPE	500 mW avg.	50 fs	570 MHz
[112]	2011	Er-Yb:fibre	HML	300 mW avg.	900 fs	10 GHz

Table 4.1: Results of fibre comb experiments prior to start. "Fo8" refers to a figure of eight construction.

and can be manipulated without a high risk of breakage. Fibres can be either core- or cladding-pumped, the latter allowing for the pump light to pass through the cladding as a waveguide and provide a large NA for the input.

4.3.1.1. Laser action in Yb:fibre

In order to generate laser action without reabsorption loss the fibre must be pumped with sufficient intensity to exceed its pump saturation intensity, thus the length of the fibre must be chosen such that the pump absorption is not so strong as to allow the reabsorption losses towards the end of the fibre due to the absence of a population inversion [113]. This has become less of an issue in recent years with high-power, fibre-coupled laser diodes because of the ability to deliver high pump powers without severe coupling losses that free-space insertion would entail.

Yb-doped fibres have poorer thermal conductivity than Yb:KYW, but this is largely mitigated by the low quantum defect of Yb^{3+} and the fact that the fibre geometry naturally offers a large surface-to-volume ratio enabling easy heat dissipa-

tion.

The emission spectrum of Yb:fibre is broader than that of Yb:KYW. In mode-locked operation this is mainly due to the dispersion characteristics of silicate glasses: any pulses passing through the length of fibre will become chirped, but, operated in the normal-dispersion regime, SPM will lead to a broad emission when compared to that of Yb:KYW. Absorption and emission cross-sections of Yb:fibre were found to be 0.39 pm^2 [114].

4.3.1.2. Optical and dispersive properties of Yb:fibre

The fibre chosen for the 375-MHz Yb:fibre laser utilised in this experiment was a core-pumped, single-mode, Yb-doped fibre made by Liekki (Yb1200-4/125) and purchased through ThorLabs. Due to its high-doping concentration, permitting the use of very short lengths, the fibre contributed only a small nonlinearity. The mode field diameter (at 1060 nm) was 4.4 $\pm$ 0.8 μm. The core absorption at 920 nm was 280 dB/m, while the peak core absorption at 976 nm was 1200 dB/m. The core's numerical aperture was 0.2, and the cut-off wavelength was 1010 $\pm$ 70 nm. The fibre had a nominal slope efficiency of 78%. The characteristics of absorption and emission are shown in Figure 4.1.

4.3.2. Modelocking methods

Due to the large gain bandwidth of doped fibres there is a great opportunity for modelocking, though the strong nonlinearity in long fibres can have serious implications on the generation of femtosecond pulses: a strong chirping effect on pulses lengthens their duration requiring the addition of intracavity dispersion management or construction of pulse-conditioning systems after the fibre. The main modelocking methods used are as follows: a figure-of-eight (FoE) construction of two fibre loops wherein one is a resonator and the other a nonlinear amplifying loop mirror to provide modelocking through interference to create low gain for low powers but to encourage high-power pulses (usually used for Er:fibre systems as seen in [98]); the inclusion of a SESAM at one end of a fibre (used in [106]); the creation of multiple pulses travelling simultaneously through the cavity to achieve high pulse repetition rates known as harmonic mode locking [100]; nonlinear polarisa-

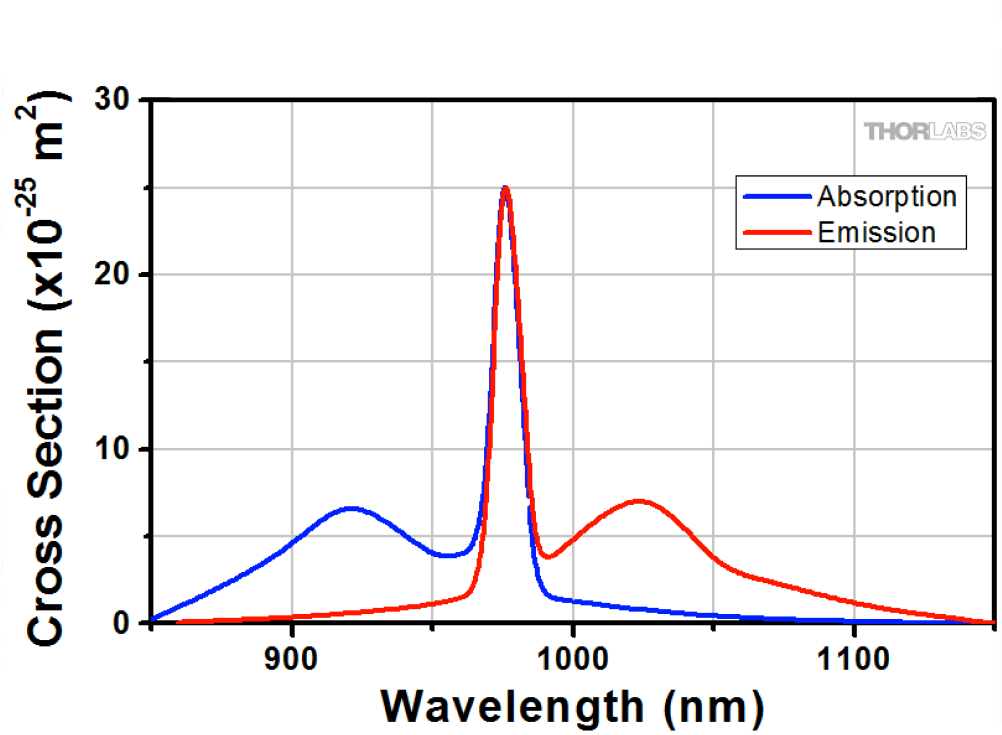

Figure 4.1: The characteristics of absorption and emission in the Yb-doped fibre used in the experiment. Peak absorption and emission overlap, but with intracavity filtering the emission spectrum can be forced into lasing at 1040 nm.

tion evolution (NPE), in which an intensity-dependent polarisation change can be exploited to encourage pulse generation (seen in [107]); and an offshoot of NPE, all-normal-dispersion (ANDi), which operates similarly to NPE save for the creation of the cavity with only normal-group-velocity-dispersion components to eliminate the need for further dispersion management in the cavity (as utilised by [101]). Active modelocking is also possible, but does not generate fs pulses. As the system used was based on a Yb-doped fibre I will explain the modelocking methods most suitable for Yb systems.

SESAM modelocking in Yb:fibre lasers is much the same as in free-space systems – pump light is coupled into the fibre and passes through a dichroic coupler into the doped fibre. The light then excites the dopant of the fibre as it passes through, meeting the other end which has been coated for reflection [115], or had a fibre Bragg mirror spliced on, with a small percentage of leakage to act as an output coupler. The laser light that passes back through the fibre reaches the dichroic coupler and, instead of passing through to the pump laser, is redirected to a SESAM.

Once sufficient intensity to saturate the absorber has been applied to the SESAM it reflects a pulse back through the doped fibre. After a short time the SESAM will generate in the fibre a strong pulse passing back and forth from output coupler to SESAM leading to mode-locked operation. This method works for all fibre lasers, and is commonly used in Yb:fibre systems. Intracavity dispersion compensation is needed to obtain transform-limited pulses directly from the cavity. An example system is shown in Figure 4.2.

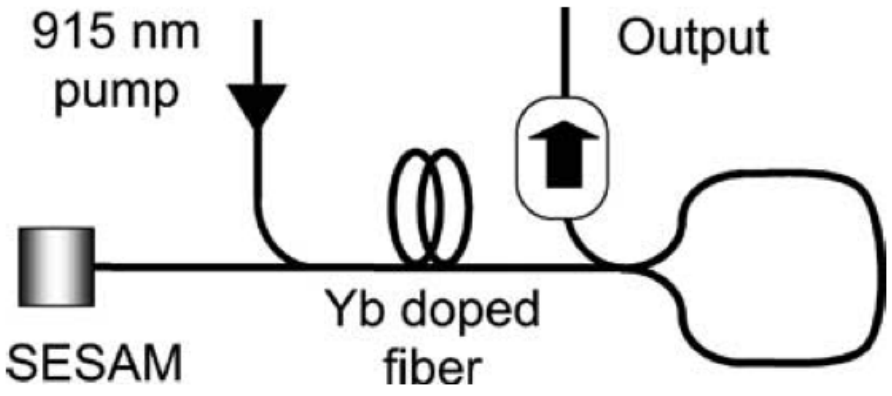

Figure 4.2: An example of a SESAM mode-locked fibre laser taken from [116].

NPE modelocking is another very common method of achieving short pulse durations at high pulse repetition frequencies. This method requires a birefringent fibre without internal polarisation stabilisation, thereby allowing for a polarisation change (not necessarily rotation of the polarisation, but a change in ellipticity) due to the inherent nonlinearities in the fibre. Used in ring cavities, NPE is often achieved by using a series of fibres with alternating normal and anomalous dispersion characteristics to have a net aggregate normal dispersion and waveplates to create a system that encourages maximum loss for polarisation states that do not correspond to the highest possible peak powers – usually configured to allow for maximum transmission of only components of the circulating field with the highest peak powers. Unlike a Q-switched system, the polarisation control before the beam splitter is to act as a change to the degree of output coupling of the system, and not a switch in place to allow or disallow laser action. A further arrangement, called all-normal-dispersion (ANDi) modelocking, removes any anomalous dispersion components and can al-

low for even shorter pulse durations at higher powers. The pulses produced by an ANDi design are highly chirped when they leave the cavity, typically requiring a grating compressor to dechirp them after the laser. An example system is shown in Figure 4.3.

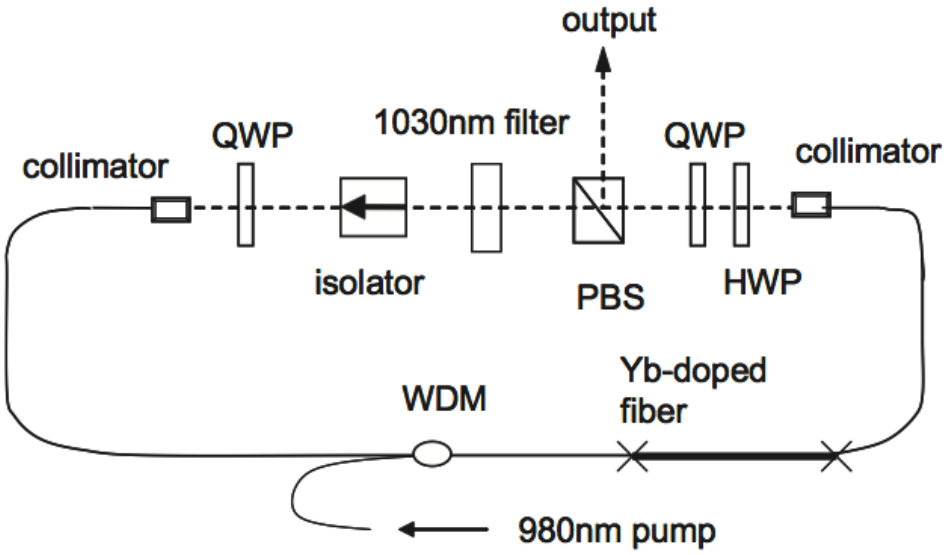

Figure 4.3: An example of a NPE/ANDi mode-locked fibre laser taken from [117].

4.4. Yb:fibre laser design, construction, and performance

The Yb:fibre laser used for the implementation of a CEO-locked frequency comb was designed and built by Carl Farrell, and was detailed in his paper *Octave-spanning super-continuum from a silica PCF pumped by a 386-MHz Yb:fiber laser* [118]. I include a description here for completeness, and because this laser was the one used for the development of the Rb-stabilised comb presented later.

4.4.1. Cavity design

The laser cavity, represented in Figure 4.4, was constructed in a ring configuration. Light from two commercially-available fibre-pigtailed laser diodes (3S Photonics 1999-CHP) was passed into a polarisation-maintaining fibre combiner. The combiner's output was spliced with a fibre-compatible collimator from which 1.35 W of 976-nm pump light passed through a pair of dichroic mirrors coated for optimal transmission at 976 nm and peak reflection at 1030 nm. The pump light then passed through a quarter-wave plate to control the ellipticity of the polarisation, into a col-

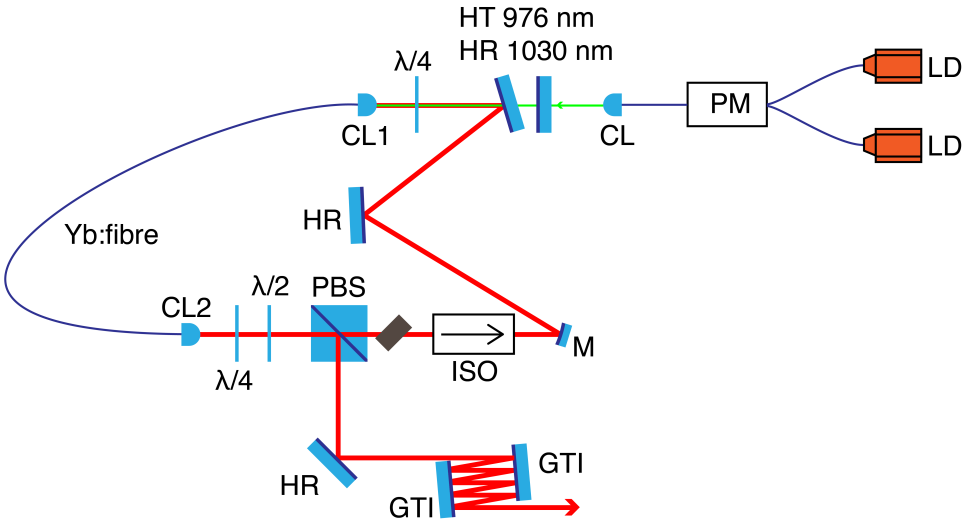

Figure 4.4: The design of the 375-MHz Yb:fibre laser. Two fibre-pigtailed laser diodes (LD) emit pump light that passes into a polarisation combiner (PM) and through a collimator (CL). The light then passed through a pair of dichroic mirrors, which were highly transmitting at 976 nm and highly reflective at 1030 nm. The pump light then passed through a quarter-wave plate ($\lambda/4$) and into a collimator (CL2) which coupled it into the Yb:fibre (YDF) generating laser light. This generated light passed through another collimator (CL1) and through a quarter-wave and half-wave plate ($\lambda/4$ and $\lambda/2$) before interacting with a polarising beam-splitter cube (PBS). The accepted laser light then passed through an interference filter (IF), an optical isolator to ensure directionality (ISO), a curved mirror (M), and a further high reflector (HR) before arriving back at the dichroic mirror pair.

limator – identical to the pump-laser output – spliced on the end of the Yb:fibre. The fibre, itself, was a 19-cm segment of highly-doped silicate fibre with a slope efficiency of 78%. On both ends were spliced identical fibre collimators, each 4.5 cm in length, bringing the length of the fibre segment of the laser to 28 cm.

Once the laser light was generated in the Yb:fibre it continued on the path of the pump beam, leaving the second collimator and passing through a quarter-wave and half-wave plate. These were used to control the directionality of the polarisation leaving the fibre as the next component was a polarising beam splitter, operating as the laser output coupler. When the laser light is of high intensity, such as during a pulse, the polarisation of the light is rotated to leave the cavity, whilst all other polarisation states corresponding to lower powers will continue on in the cavity.

The light circulating in the laser cavity passed through an interference filter of 10-nm bandwidth and set at an angle to prioritise 1030-nm light generation. The intracavity beam then travelled through a Faraday rotator (or optical isolator),

which was to ensure the uni-directionality of the ring cavity before reflecting off a curved mirror, a high reflector, and again off the input dichroics before being coupled back into the Yb:fibre. The curved mirror was in place to directly image the mode from one of the Yb:fibre's collimators onto the other, thereby improving coupling efficiency. In order to choose the ideal curvature of the imaging mirror an ABCD matrix model was created for calculating the coupling efficiency resulting in an optimal value of 500 mm radius of curvature.

4.4.2. Characteristics of the Yb:fibre laser

An initial power optimisation was performed, resulting in an output power of 605 mW, indicating an optical-to-optical conversion efficiency of 45%. A measurement of the laser spectrum, as well as an interferometric autocorrelation, was performed (seen in Figure 4.5). As the spectrum could not be described adequately by a Gaussian or sech^2 profile a fitting procedure was used to estimate the duration and pulse shape of the pulses leaving the fibre. In order to accomplish this the optical spectrum was recalibrated through the addition of quadratic and cubic spectral phase before Fourier transforming to find the corresponding pulse. The autocorrelation of this pulse would then be numerically calculated and compared with the experimental result. A flowchart describing the fitting approach is shown in Figure 4.6.

In order to produce the shortest possible pulses from the Yb:fibre laser, the system was aligned into a pair of GTI mirrors (as seen in Figure 4.4) to apply an extracavity GDD – the group-delay dispersion (GDD) response curves of which are seen in Figure 4.7. To determine the optimum compression the autocorrelation traces were fitted using the method outlined above. A series of these measurements, between 10 and 16 bounces off of -1300 fs^2 GTI mirrors (as well as a possible addition of -600 fs^2 from an optional steering mirror) allowed for a broad range of compression, and, it was hoped, would bracket the ideal number of bounces for pulse duration optimisation. As these mirrors also had a reflectance at 1040 nm of 99.9762%, the pulse compression was expected to reduce the laser power only by a small fraction. The results of these tests are seen in Figure 4.8.

When the total applied GDD was -18800 fs^2, the pulse durations were measured

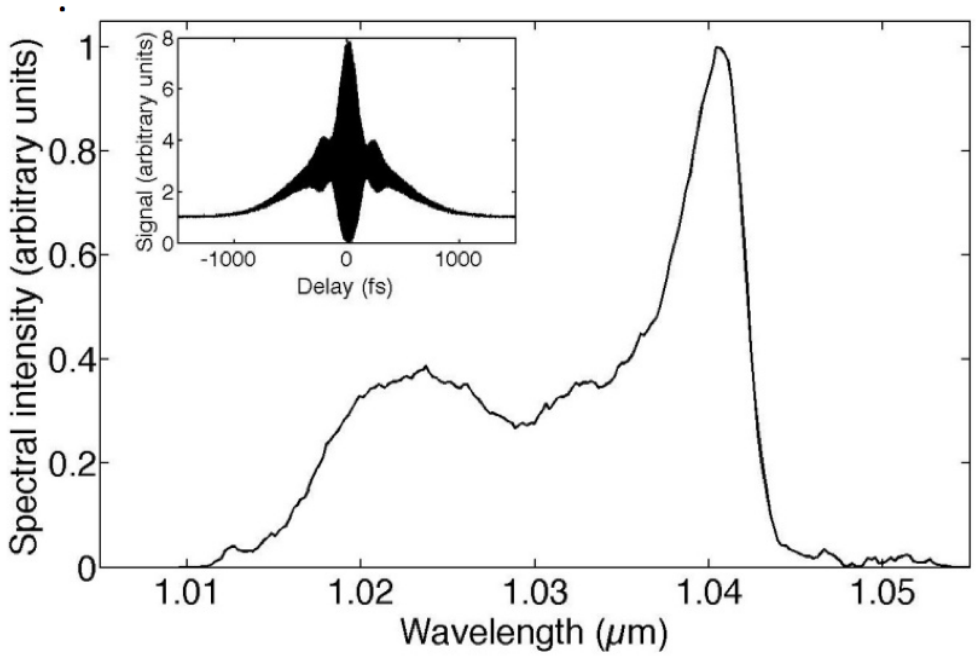

Figure 4.5: The optical spectrum from the mode-locked fibre laser with simultaneous interferometric autocorrelation (inset) [118]. This laser spectrum was much broader than that from the Yb:KYW laser, thereby allowing for better pulse compression.

to be at their minimum value. A comparison of these pulse durations with the applied GDD is seen in Figure 4.9.

The amount of quadratic spectral phase corresponding to the best-fit result generated by measuring the autocorrelations was -18000 fs^2, which meant a FWHM pulse duration of 750 fs, that, when de-chirped, implied transform-limited durations of 123 fs. Despite the lack of rigour when compared to the frequency-resolved optical grating (FROG) technique we are still able to find the pulse chirp, thereby improving future compensation.

Figure 4.10 presents the autocorrelation and temporal profile (inset) if the optimally de-chirped pulses. Average power post-compression was 580 mW, or 13.7 kW peak pulse power. The laser's higher peak power would, it was expected, lead to a broader spectrum post-PCF broadening, but the lower pulse-repetition frequency and unusual profile (non-$sech^2$) indicated issues with pulse measurement.

It was with this system, with its short pulses and broad spectrum, that further work to create a CEO-stabilised frequency comb was undertaken.

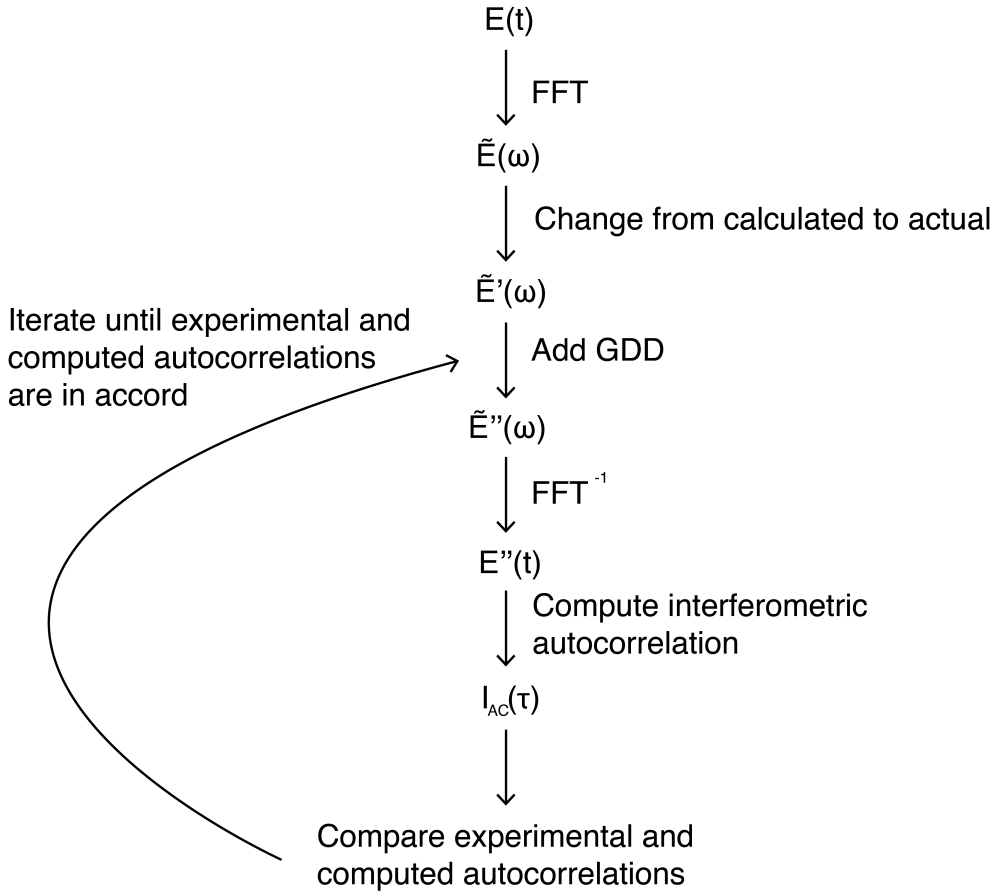

Figure 4.6: A flowchart detailing the fitting procedure using a bespoke MatLab code. After making an initial guess as to the pulse's field amplitude in time the frequency-domain amplitude is calculated before replacing the guessed field intensity with the square root of the measured intensity. A GDD value is added and an inverse Fourier transform is performed on the resultant field amplitude. We now compute the interferometric autocorrelation and compare it to the measured autocorrelation. If they do not correspond, then a further GDD value is added to the calculated pulse and the loop runs again until the two are in agreement.

4.5. Repetition rate stabilisation of the Yb:fibre laser

4.5.1. Locking loop design

The pulse repetition frequency of the Yb:fibre laser was stabilised in much the same manner as that of the Yb:KYW laser: a small proportion of the light – approximately 4% – was picked-off after the pulse compression system and redirected into a fast photodiode. The signal from the fast photodiode was filtered using a < 500-MHz low-pass filter and directly into a double-balanced mixer (MiniCircuits ZFL-500LN) where it met a 375-MHz signal from a referenced frequency synthesiser. The resultant beat was passed through a PI controller and through a high-voltage amplifier

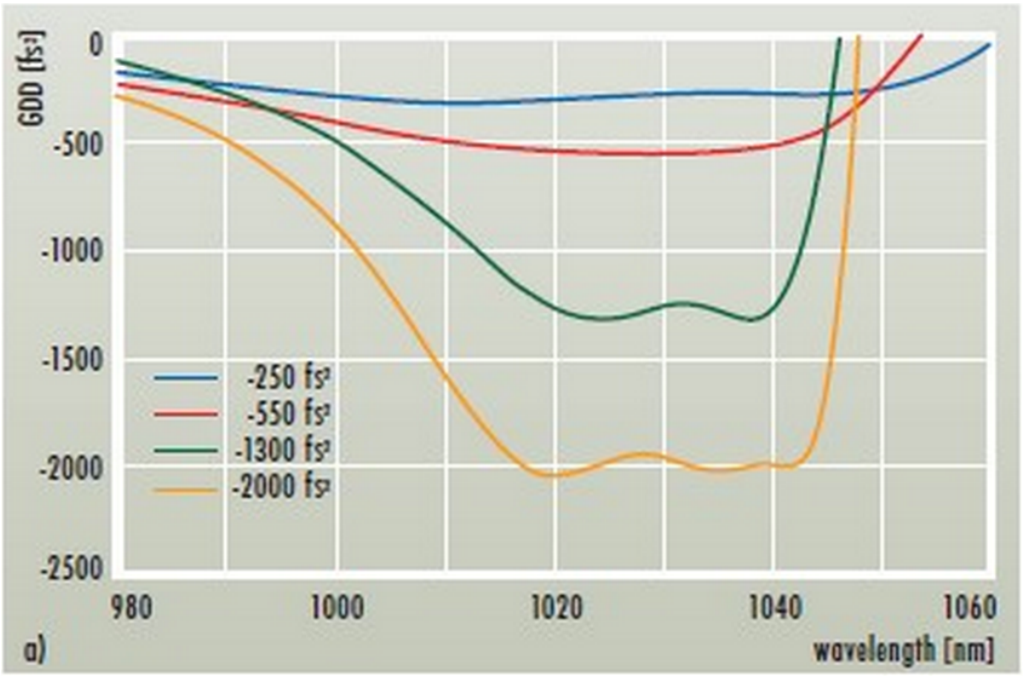

Figure 4.7: The sample GDD curves of Layertec GTIs at -250, -550, -1300, and -2000 fs^2 at wavelengths between 900 and 1060 nm. The green curve represents the characteristics of the mirrors used. [Taken from www.layertec.de/en/capabilities/femtosecond/GTI]

(Falco 20x amplifier) before reaching the piezo driving the placement of the curved mirror in the cavity.

A 9-μm-travel piezo element was included in the cavity (see Figure 4.13) by placing it in the curved mirror's translation stage, and, due to the stretching of the laser cavity to accommodate the PZT, the resulting Yb:fibre laser now had a pulse repetition frequency of 375 MHz.

4.5.2. Noise characteristics of the locked repetition rate

Due to the small scale of the noise from f_{rep} (<1 Hz), and the limited resolution of the frequency counter when used on a multi-100-MHz scale, a comparative arrangement to measure the frequency variance was needed. By mixing the output with another referenced synthesiser operating approximately 2 kHz away from the beat signal and counting the frequency I was able to discern the RMS deviation and Allan variance (two-point deviation) with observation times between 0.1 and 50 seconds (results shown in Table 4.2).

A graphical representation of these results can be seen in Figure 4.12. The slight increase towards the longer averaging times is understood as longer-term instabilities

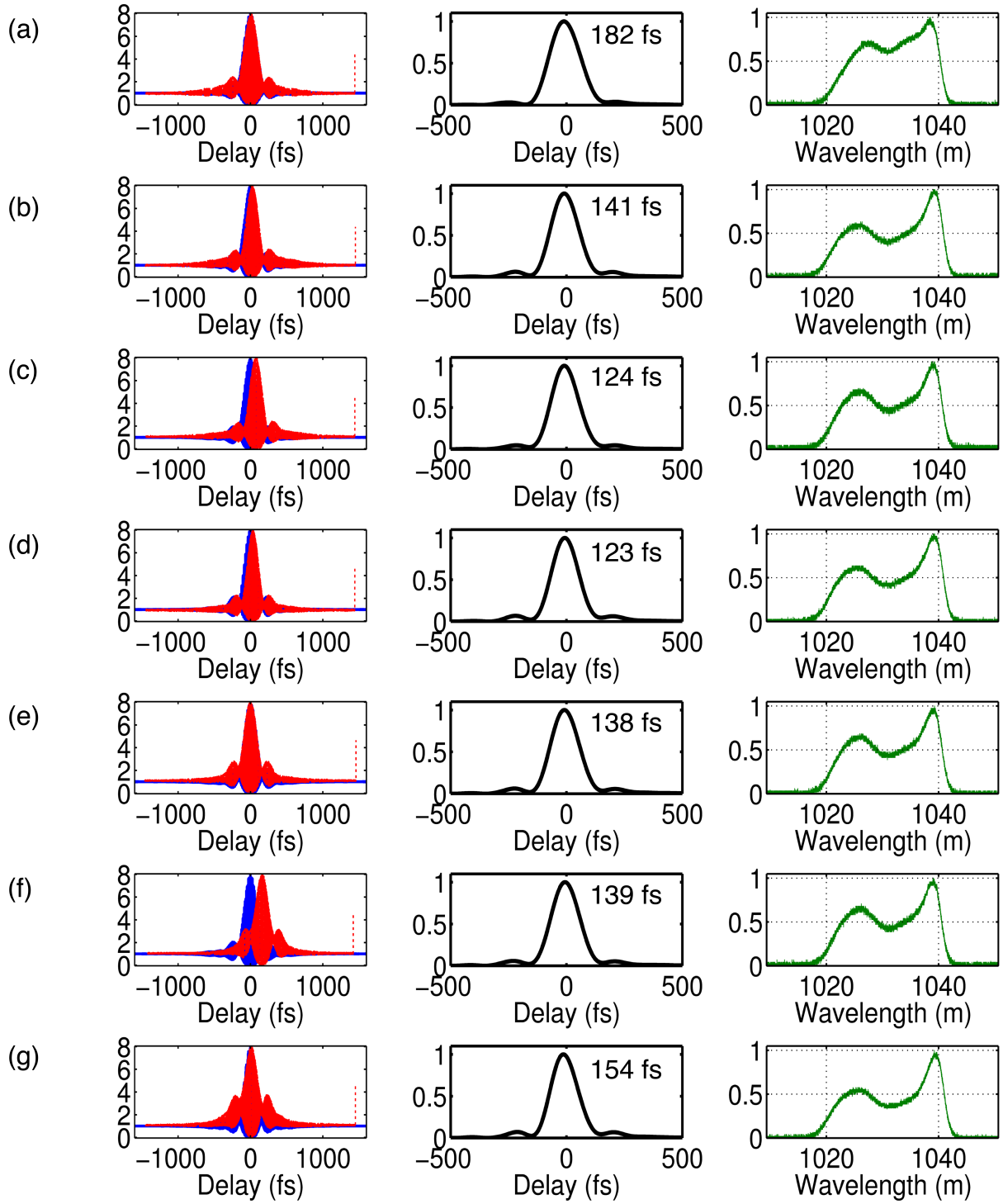

Figure 4.8: Left to right: Comparison of computed (blue) and measured (red) autocorrelations, the corresponding temporal pulse intensity, and the measured spectrum after the compressor for extracavity GDD of (a) -13000 fs^2; (b) -13600 fs^2; (c) -15600 fs^2; (d) -16200 fs^2; (e) -18200 fs^2; (f) -20800 fs^2; and (g) -21400 fs^2.

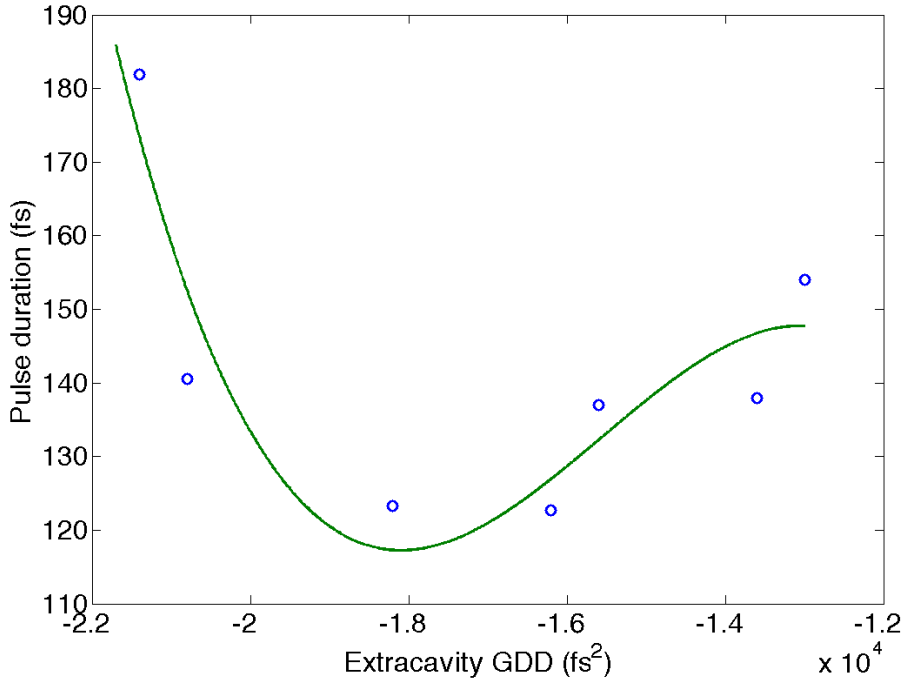

Figure 4.9: FWHM durations of the computed pulse profiles as the extracavity GDD was varied (symbols) and a cubic fit to the data (green line). Optimum compression is limited by 3rd-order dispersion to ≈123 fs at a GDD of ≈ -18000 fs^2.

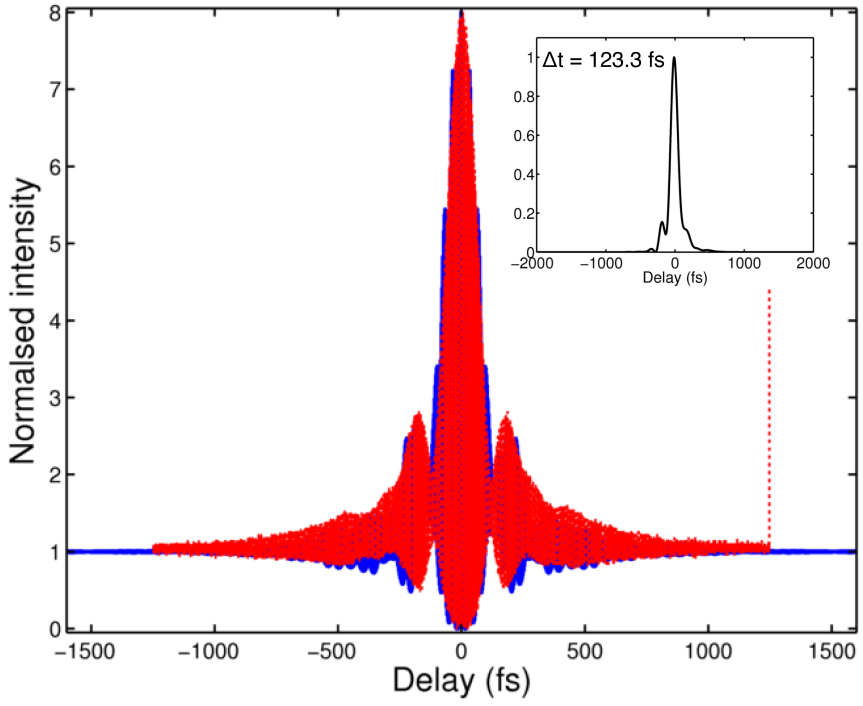

Figure 4.10: The interferometric autocorrelation from the laser after compression, corresponding to a pulse duration of 123 fs. Inset: the pulse profile [118]. This leads to a much higher peak power, but the lower pulse-repetition frequency will decrease the spacing of laser modes and the non-sech^2 profile would lead to problems with measurement of pulse durations.

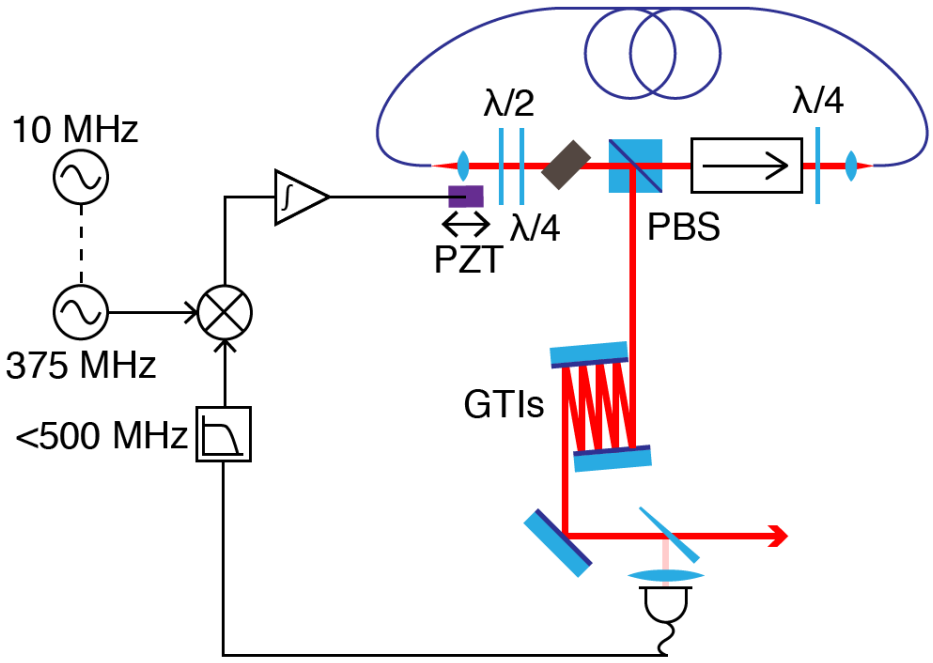

Figure 4.11: The schematic of the rep-rate locked 375-MHz Yb:fibre system. 4% of the emitted light is redirected to a fast photodiode, the output of which is passed through a low-pass filter at 500 MHz and into a double-balanced mixer with the 375-MHz output from a 10-MHz Rb-stabilised frequency synthesiser. The heterodyne beat between the two is then amplified through an integrating amplifier, and the resultant signal is applied to a PZT in the cavity to change the cavity length.

Gate Time	RMS deviation	Allan variance
100 ms	0.109105 Hz	0.105827 Hz
200 ms	0.056505 Hz	0.052463 Hz
500 ms	0.033163 Hz	0.029754 Hz
1 s	0.026014 Hz	0.024399 Hz
2 s	0.021185 Hz	0.016456 Hz
5 s	0.021474 Hz	0.014117 Hz
10 s	0.010895 Hz	0.010505 Hz
20 s	0.013680 Hz	0.005396 Hz
50 s	0.012402 Hz	0.005893 Hz

Table 4.2: RMS deviation and Allan variance of Yb:fibre f_{rep} at differing observation times.

present in the repetition rate from thermal fluctuations.

The frequency change with respect to its mean can similarly be seen, graphically represented, in Figure 4.13. This shows an excellent long-term stability with few major fluctuations.

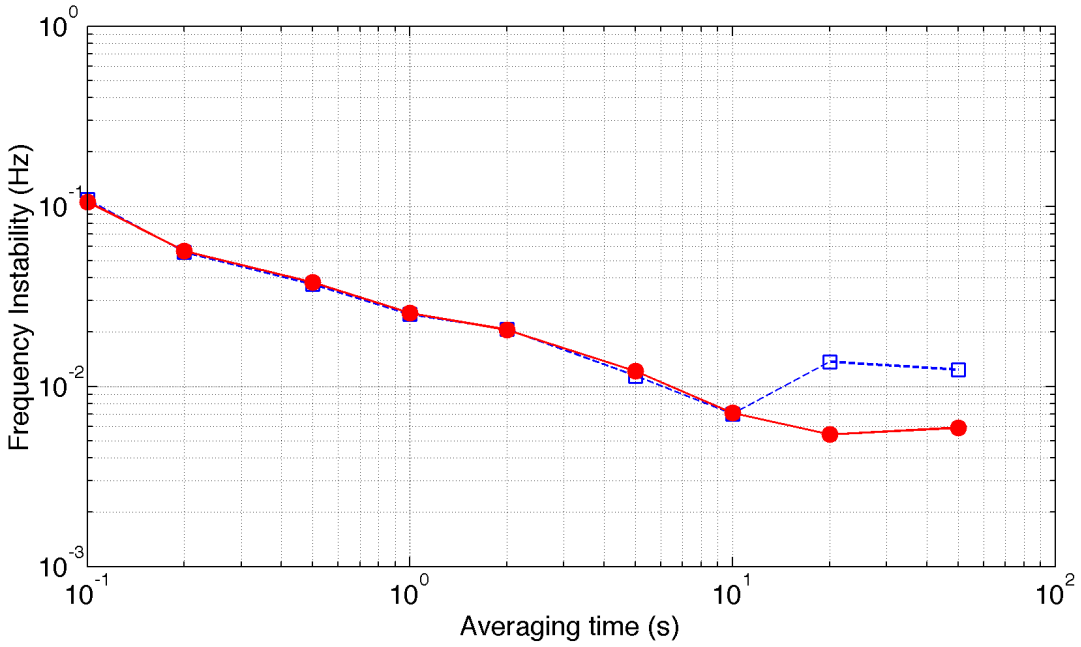

Figure 4.12: The RMS deviation (dashed blue) and Allan variance (solid red) of the pulse repetition frequency with increasing observation times.

Now, as the contribution to noise from f_{rep} is multiplied as the comb mode increases, we can look at the variation at the centre wavelength of the produced comb. If we take the centre wavelength to be 1030 nm, or 2.906 $\times 10^{14}$ Hz:

$$\frac{2.906 \times 10^{14} \text{ Hz}}{375 \times 10^{6} \text{ Hz}} \approx 776000 \tag{4.1}$$

The centre frequency corresponds to the 776000$^{\text{th}}$ comb mode. Multiplying this by the RMS deviation of f_{rep}:

$$776000 \times 0.012402 \text{ Hz} = 9624.0 \text{ Hz}. \tag{4.2}$$

It can be seen that the RMS change in frequency at the centre of the output spectrum is 9.6 kHz. Similarly the point-to-point deviation ($\approx$ Allan deviation) implies an uncertainty of

$$776000 \times 0.005893 \text{ Hz} = 4573.0 \text{ Hz}. \tag{4.3}$$

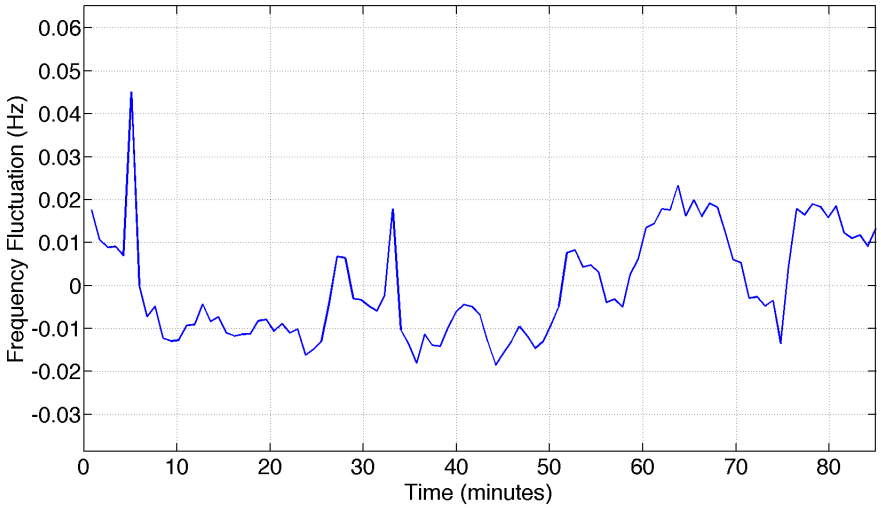

Figure 4.13: The frequency fluctuations of the pulse repetition frequency relative to the mean with f_{rep} stabilisation turned on for averaging times of 50 s over a period of 83 minutes (100 samples). The RMS deviation was 12.4 mHz.

4.5.3. Conclusions

Pulse repetition frequency locking was performed on the Yb:fibre laser, and measured over many observation times ranging from 0.1-50 seconds. The RMS deviation of f_{rep} was calculated and, thus, the noise contribution to the centre frequency of the laser's output, approximately the 776000^{th} comb mode, was found to be 9.6 kHz. This showed a system with a pulse repetition frequency instability of only 3.3×10^{-11}, which was of a sufficient stability for a GPS-stabilised frequency comb of the intended accuracy.

An attempt to control and reference the carrier-envelope offset for referenced comb generation was carried out.

4.6. CEO stabilisation

While many femtosecond frequency combs have been built for superb accuracy in the frequency-domain (on the order of 10^{-17} to 10^{-18} Hz) many applications require only accuracy more in the range of 10^{-11} Hz for example, comb-line spectroscopy at 1040 nm using a comb with $1{:}10^{11}$ stability would have a resolution of <3 kHz, which easily has the resolution necessary to resolve the typical Doppler-limited linewidths of room-temperature atoms and molecules. A further problem arises in the standard method for stabilised comb generation, f-2f referencing, which has necessitated the

use of Yb:fibre amplifiers to increase the average powers of these systems to more than 1 W to generate pulses suitable for producing octave-spanning supercontinua [102]. This becomes even more difficult at higher pulse repetition frequencies, which lack the pulse powers to reliably generate a spectrally-coherent octave. These higher repetition rates, however, lead to higher power per comb mode, which indicates that direct referencing from a frequency standard should prove achievable.

Direct referencing of comb teeth through heterodyne beating to a separate frequency reference has been demonstrated, and work was undertaken to lock the 375-MHz Yb:fibre laser to an absolute optical frequency reference derived from the crossover resonance in ^{87}Rb, which was used to stabilise an ECDL lasing at 780.2 nm.

4.6.1. ^{87}Rb-stabilised ECDL

The crux of the carrier-envelope locking loop was a direct reference to a Rb atomic optical standard; the transition from the $5^2S_{1/2}$ energy level to the $5^2P_{3/2}$ level. First I will detail the design of the ECDL (constructed by Karolis Balskus) followed by a description of the underpinnings of Rb-locking to the D2 transition crossover resonance of ^{87}Rb, itself having an average output of 780.24 nm [119].

4.6.1.1. ECDL design

To create a suitable and direct optical reference for the stabilisation of a frequency comb it was decided that a laser diode locked to a rubidium optical standard would be used. Most diode lasers possess an emission bandwidth of $\approx$ 1 nm, unsuitable for accurate frequency locking, and can have problems of long-term frequency and output power stability. By controlling the drive current and device temperature the emission wavelength can be tuned, with additional wavelength selectivity possible by the introduction of a diffraction grating forming an external cavity. By turning the diffraction grating it was possible to tune the wavelength of the laser output, and an additional piezo element allowed for fine-tuning and feedback control.

The system was designed as shown in Figure 4.14. Laser light exited the laser diode, passed through a collimating lens, and was incident on a diffraction grating, the first-order diffraction of which was directed back at the laser diode. As the

polarisation of the diode light was orientated such that the Littrow-diffracted light experienced only low efficiency, the 0^{th}-order light formed the useable output.

If we examine the grating equation

$$D \cdot (\sin\theta_i + \sin\theta_d) = m \cdot \lambda \tag{4.4}$$

where D is the diffraction grating pitch, θ_i is the incident angle of the laser light, θ_d is the diffraction angle, and m is the diffraction order we find that the angles θ_i and θ_d must be identical to reflect light back into the laser cavity as the Littrow configuration where the diffracted wavelength is dependent on the incident angle:

$$\frac{\lambda}{D} = 2 \cdot \sin\theta_i. \tag{4.5}$$

The control of the emitted wavelength could then be performed by a direct voltage applied to the piezo attached to the diffraction grating.

The light from the 0^{th}-order passed through a Rb cell and onto a photodetector, the signal from which then entered a variable-gain amplifier and into a double-balanced mixer with a 7.46 kHz signal provided by a frequency synthesiser. The output of the mixer passed through a 153-Hz LPF and an integrating amplifier before entering a summing amplifier. Similarly a DC voltage, the 7.46 kHz signal, and ramp generator were all input to the summing amplifier, the output of which drove the PZT attached to the diffraction grating.

Once a feedback loop was created it was possible to lock the wavelength output of the diode laser to a known frequency standard. For these purposes Rb-gas saturated absorption control was utilised, as ^{87}Rb provides very strong absorption lines. The line of particular interest is the D_2 transition, that from the ground state of the $5s^1$ electron to the excited state $(5p)^2P_{3/2}$, with a wavelength of 780.241209686 nm.

For the purposes of this system we used a Rb-gas cell containing a naturally occurring isotope mixture of 28% ^{87}Rb and 72% ^{85}Rb atoms. The absorption spectrum measured for locking is shown in Figure 4.15. The absorptions on the left-hand side belong to the transitions in ^{87}Rb while those on the right belong to the ^{85}Rb transi-

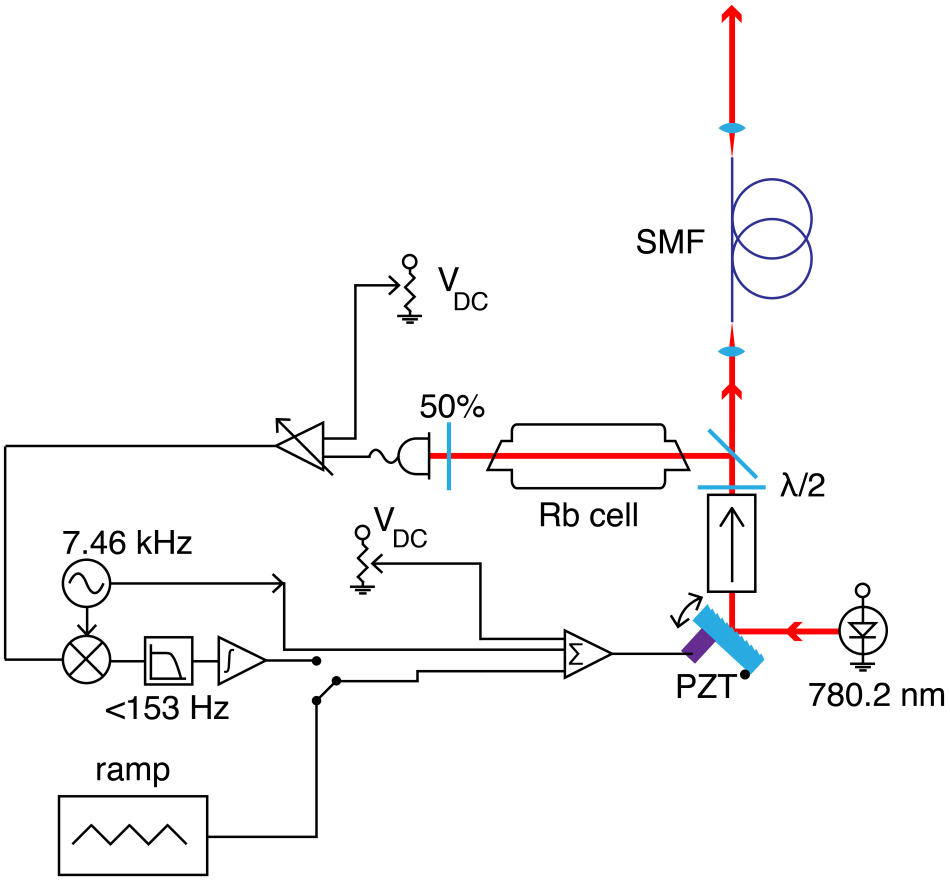

Figure 4.14: The design of the rubidium-locked external cavity diode laser. Light exits a laser diode operating at 780.2 nm and interacts with a diffraction grating in Littrow configuration. The 1st-order light reenters the laser diode while the 0th-order light passes through an optical isolator and a half-wave plate before reaching a 99:1 beamsplitter. 99% of the light passes through and is collimated into a SMF. The other 1% traverses a Rb-gas cell, through a 50:50 beamsplitter, and on to a photodiode. The signal from the photodiode has a DC-voltage applied to it and enters a double-balanced mixer with a 7.46 kHz signal from a frequency synthesiser, which is simultaneously sending the same signal to a summing amplifier. The combined RF signal exits the mixer, passes through a 153 Hz LPF, into an integrating amplifier, and subsequently into the same summing amplifier as before. A ramp signal and DC voltage are also applied to the summing amplifier, the output of which drives the PZT on the diffraction grating.

tions. The ECDL was locked to the strongest ^{87}Rb transition, the $F = 2 \rightarrow F' = 2, 3$ crossover, and had an absolute optical frequency of 384 227 981.9 MHz [119].

A very small proportion of the laser light, 1%, was redirected by a beamsplitter through a Rb-gas cell and onto a photodiode. A 50% reflecting mirror before the photodiode returns sufficient light through the ^{87}Rb cell to saturate each absorption line, providing a Doppler-free peak of width $\approx$ 6 MHz. The photodiode signal,

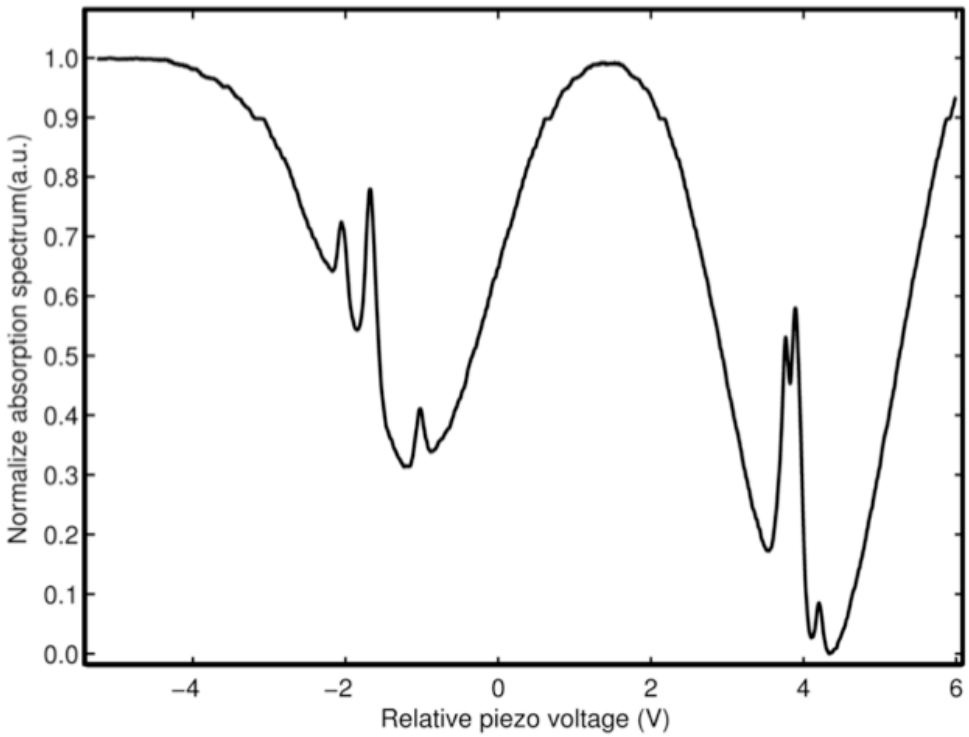

Figure 4.15: The absorption spectrum of Rb-gas. On the left-hand side are the contributions from ^{87}Rb and on the right hand side are those from ^{85}Rb.

and thus the amplitude modulation caused by the laser light's passage through the rubidium, allowed for dither locking.

4.6.1.2. Dither-locking to ^{87}Rb

Dither locking allows for the output frequency of a laser to be stabilised by acting as a frequency-dependent converter. This then produces an error signal which can be used to lock the laser. The dither locking method is dependent on the modulation of a known signal, which is picked up by the photodetector at the end of the Rb cell. Low amplitude modulation leads to a small voltage change across the piezo, and so a frequency modulation across the Rb absorption spectrum allows for a scan of the absorption lines present. The frequency modulation must be very small (on the order of a MHz), though, to ensure low noise.

This ramp is applied across the PZT, which sweeps the operating wavelength of the laser diode to probe the Rb cell and find the absorption peaks present. By locating the absorption associated with the D_2 transition we can set this as a zero point, and, when locked, the PZT corrects for any wavelength change in the laser

diode if it drifts away from the selected point, as well as changing the length of the external cavity to allow for the standing-wave mode associated with that wavelength change. Once the peak is located and centred the amplitude of the periodic PZT variation would be reduced to 0 V to lock the laser output to this position. A much lower amplitude 7.46 kHz modulation is permanently applied to the PZT, which is used (via the demodulation mixer) to provide the feedback signal used for locking. The combination of mixer and low-pass filter (see Figure 4.14) serves to differentiate the absorption peak, providing a steep voltage transition from + to − across the absorption feature: a steep crossing point at the desired value.

4.6.2. Supercontinuum generation

CEO stabilisation using a ^{87}Rb reference requires the Yb:fibre comb to be spectrally broadened to provide a wavelength component at 780.2 nm. The short pulse durations and high average power of the Yb:fibre system allow it to be efficiently broadened using a PCF specifically designed for supercontinuum generation of input light at 1030 nm to test for an octave-spanning supercontinuum (necessary for f-2f referencing). The 1.5-m silica PCF was made by NKT Photonics, with a core diameter of 3.7 μm and NA of 0.25. It was designed for a zero-dispersion wavelength of 975 ± 15 nm, and had a nonlinear coefficient of 18 W·km^{-1}. The fibre had FC/PC-connectorised ends for easy implementation. The light was coupled into the fibre (using a ThorLabs C340TME-B f = 4.5 mm lens) with 570 mW of power and was emitted from the other end with 430 mW, indicating a 75% coupling efficiency.

Initially a model was generated based on work by John Dudley [14] introduced in Chapter 1. In Figure 4.16 a visual representation of the broadening over the 1.5-metre length of fibre can be seen using the parameters as follow: $\gamma = 0.018$; $L = 1.5$ m; $P_{av} = 400$ mW; $\Delta\tau_P = 123$ fs; and $f_{rep} = 375$ MHz.

The PCF-broadened spectrum (Figure 4.17) showed strong Raman pulse generation at higher wavelengths, and was capable of providing a full octave. f-2f referencing was attempted, but was unsuccessful, possibly due to poor spectral coherence across the octave, and another method was needed. As the power per comb mode was high due to the high pulse repetition frequency of the Yb:fibre system it

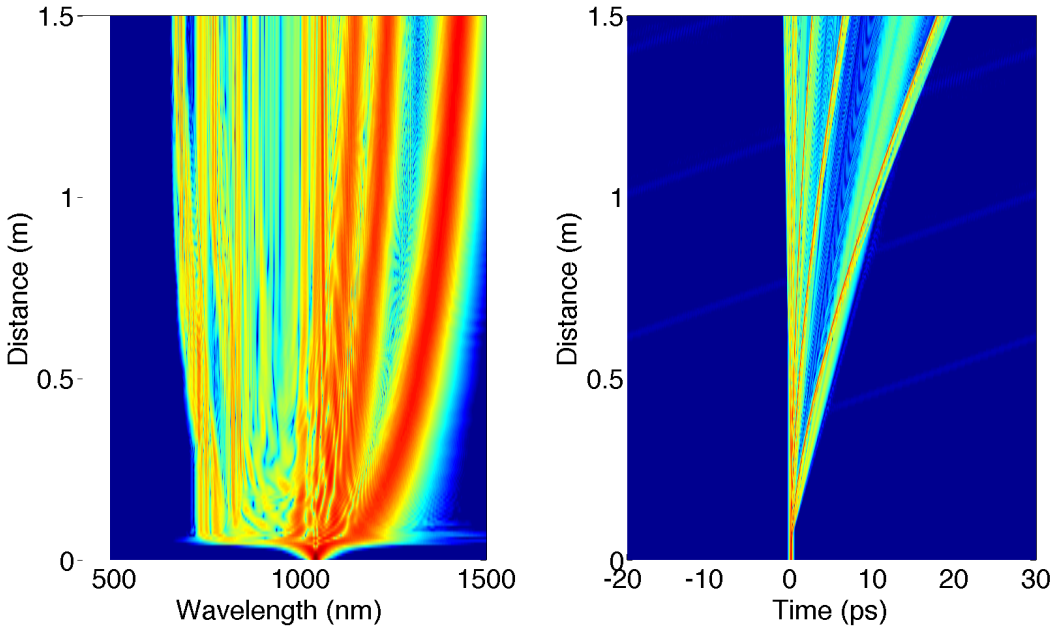

Figure 4.16: The predicted spectral (left) and temporal (right) broadening of the pulses from the 375-MHz Yb:fibre laser as they pass through a 1.5-m PCF. The extent of the broadening can be seen to form a supercontinuum from 700-1450 nm.

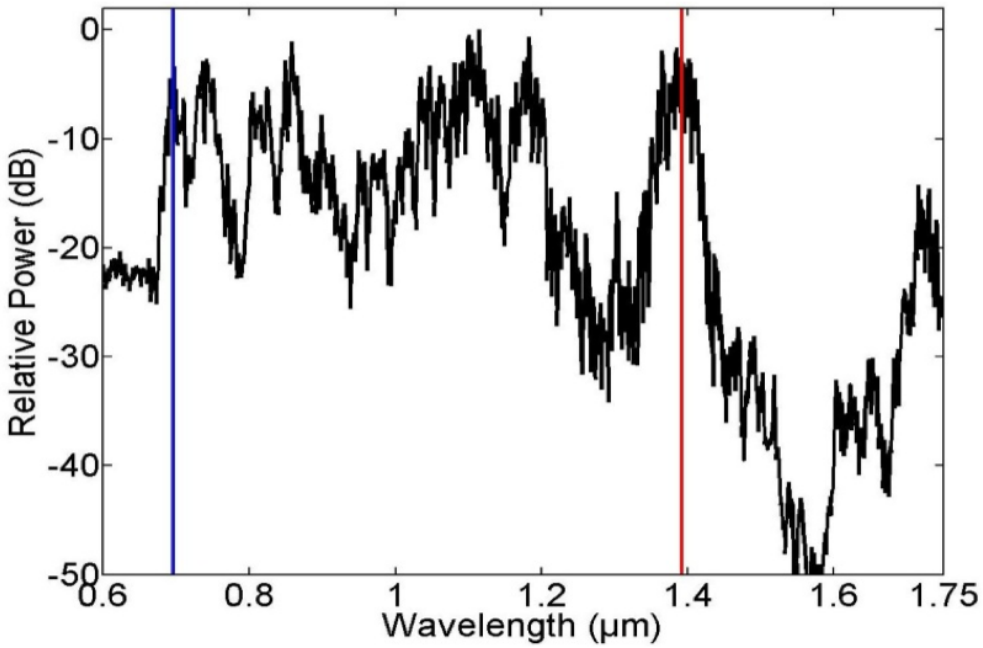

Figure 4.17: The optical spectrum from the mode-locked fibre laser after passing through a 1.5-m PCF. The vertical blue line shows a peak at 696 nm and the red shows one at its harmonic: 1392 nm. [118].

was thought that direct referencing would be possible.

To test the viability of direct referencing a common-PCF arrangement was constructed (Figure 4.18) to allow for optimal modematching between the Yb:fibre and

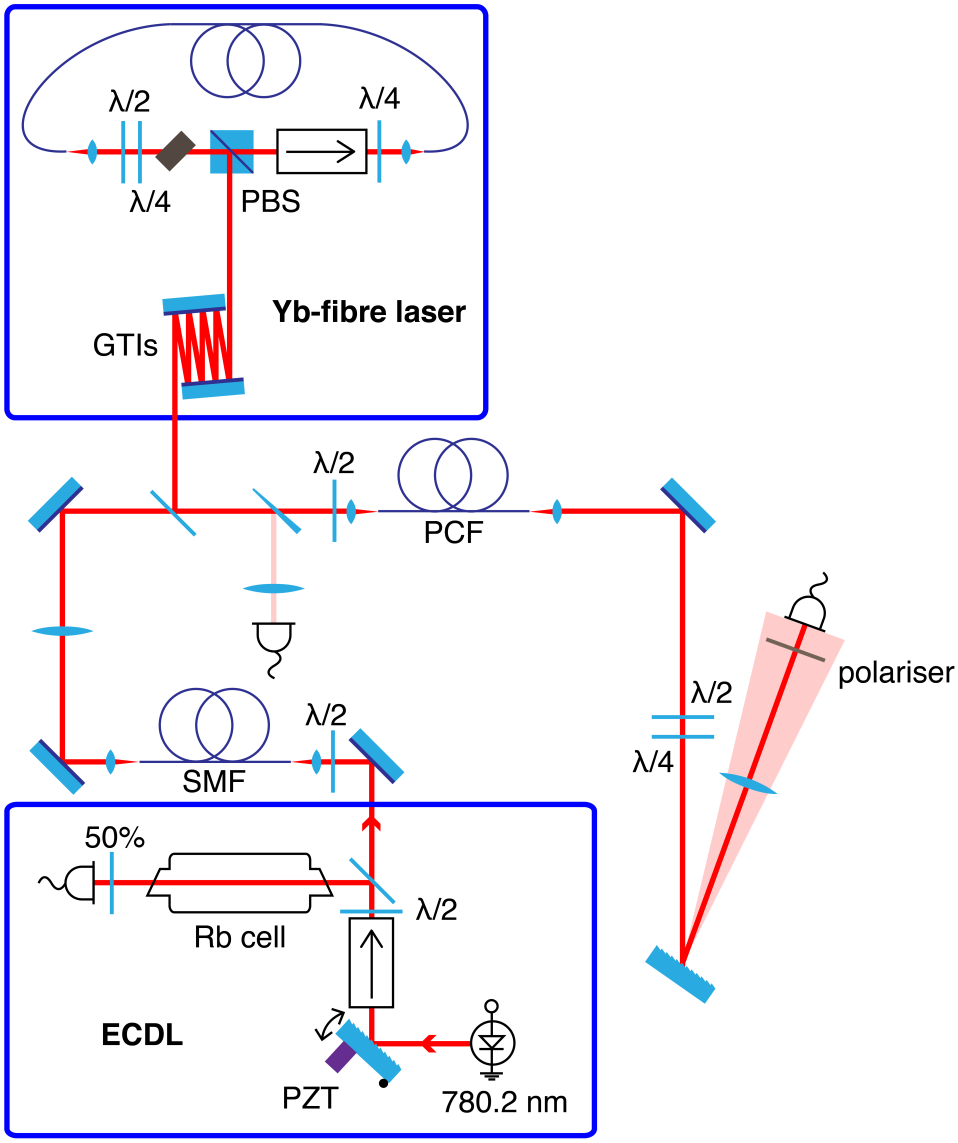

Figure 4.18: To improve the SNR of the direct comparison between comb modes near 780.2 nm and the ECDL reference a common-path arrangement through a PCF was built. Light from the Yb:fibre and SMF output of the ECDL were combined and collimated into a PCF, from which the light was directed onto a diffraction grating, through a lens to further spatially separate the modes, and onto an avalanche photodiode (APD).

ECDL beams, thus improving the possible signal-to-noise ratio (SNR). Light from the ECDL was coupled into a single-mode fibre (SMF) to create a Gaussian spatial mode and to allow for easy delivery of the beam. The spectra were seen to overlap, and no change to the ECDL signal from the PCF was seen. These data are shown in Figure 4.19, showing the spectra of the Yb:fibre laser after compression, after spectral broadening through the PCF, the spectrum of the ECDL output and mixed signals, and, finally, the spectrum of the signal at the image plane of the

monochromator.

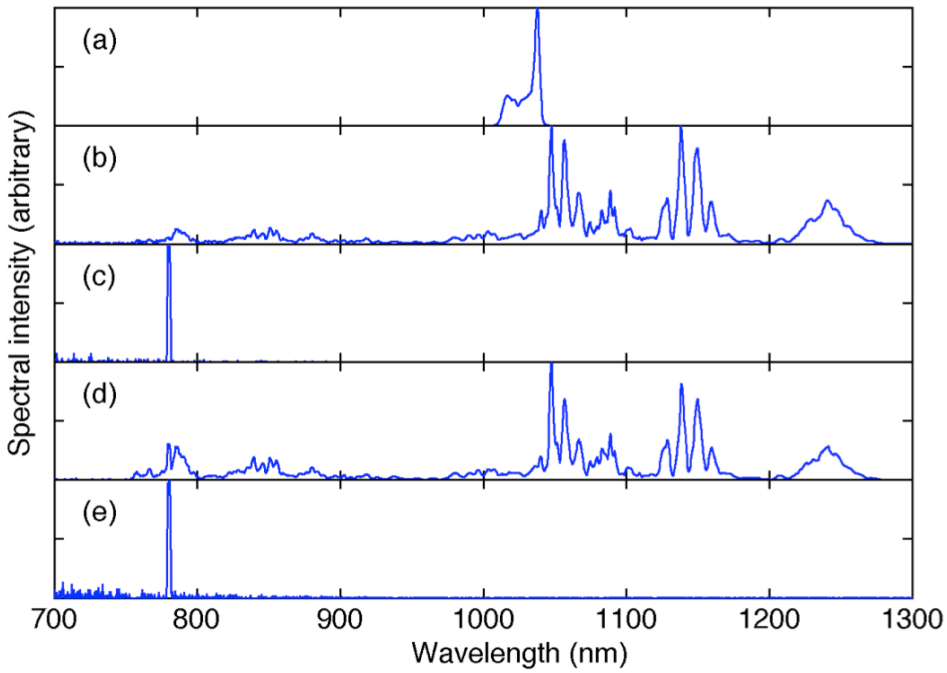

Figure 4.19: (a)Yb:fibre laser spectrum after dispersion management; (b) supercontinuum generated by passage of Yb:fibre light through 1.5-m PCF; (c) spectrum of Rb-locked ECDL; (d) combined spectra of Yb:fibre laser and ECDL after combination in PCF showing no change to ECDL wavelength; (e) Combined and spectrally-filtered spectra of Yb:fibre laser and ECDL at the focal plane of the monochromator. All intensity scales are normalised and linear.

A beat signal was acquired from the interaction between both ECDL and fibre laser, but with very low amplitude and great movement across its frequency.

4.6.3. Monochromator construction

4.6.3.1. Monochromator design

In an effort to improve the signal-to-noise ratio (SNR) of the beat between the Yb:fibre laser and ECDL reference a monochromator was constructed to spatially separate the comb modes and isolate those closest to 780 nm. To design the monochromator such that a useable signal may be seen ($>$ 20 dB) a theoretical model calculating the efficiency of mode separation and noise characteristics of the future monochromator using the grating equation was made. With the characteristics in Table 4.3 the monochromator was expected to have a resolution of 0.14 nm (limited to 0.16 nm experimentally due to the slit size: the diameter of the APD). The relative powers of both comb and ECDL were 20 μW (measured by 200 μm

pinhole), implying a power per mode of 10 nW and an optimal SNR of 23 dB.

Diffraction order "m"	1
λ (metres)	0.00000078
Grating line density "a"	1800 lines/mm
θ_i	45°
Diameter of incident beam	3 mm
Lens focal length (metres)	0.5
Slit diameter (metres)	0.000205

Table 4.3: The characteristics of the assembled monochromator.

4.6.3.2. Implementation

The monochromator was constructed such that combined light from the PCF would travel through quarter-wave and half-wave plates – optimising the polarisation – to land on a diffraction grating in a near-Littrow configuration. This was to improve the reflected power from the diffraction grating, but meant that the beam could not be expanded as would normally be the case. The first-order diffracted light would then travel 500 mm before passing through a 500-mm-focal-length plano-convex lens. The diffracted light would then travel a further 500 mm to be imaged on to the surface of an APD (Becker and Hickl APM-400) with a 0.042 mm^2 active area ($\approx$200-μm diameter).

In order for the best possible SNR the light from both ECDL and Yb:fibre comb had to be collinear with good mode matching. This was accomplished by the common-PCF arrangement discussed earlier. The resultant RF spectrum showing the repetition rate and beat signal is shown in Figure 4.20. The repetition frequency of the laser at 375 MHz and the two sidebands at $\pm$99 MHz are seen in the main figure, while the inset shows the beat, itself.

4.6.4. Intracavity filter control of the carrier-envelope offset frequency

Several methods requiring a significant effort were attempted to control the CEO-beat signal between the ECDL and Yb:fibre before arriving at intracavity filter control. First was direct current control of the pump lasers, which was found to change the nonlinear component of the refractive index in the Yb:fibre too quickly, thus changing the pulse repetition frequency of the laser too quickly for the f_{rep}-locking

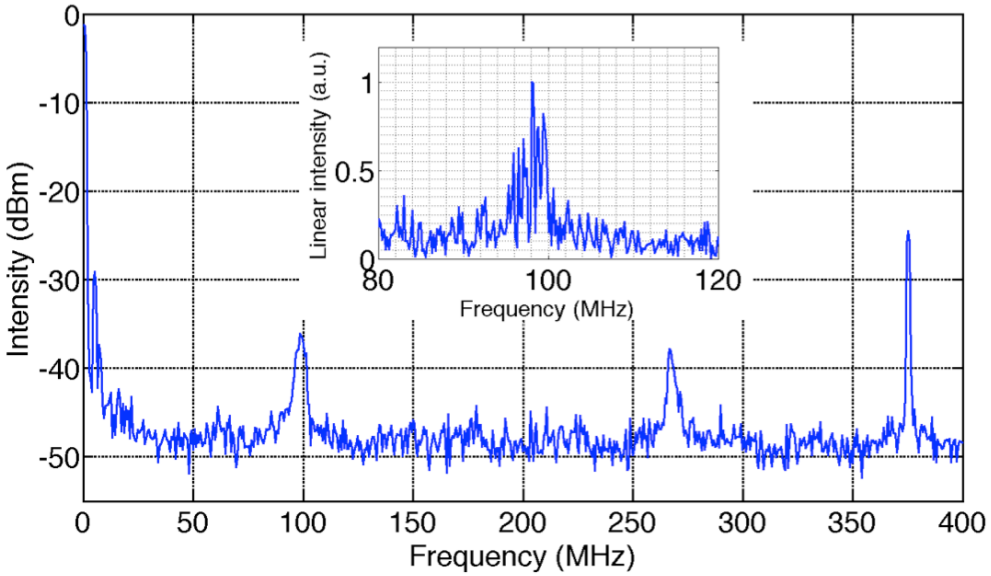

Figure 4.20: The heterodyne signal recorded with Yb:fibre laser rep-rate locked but without f_{CEO} stabilisation. The signal at 375 MHz is f_{rep} and those are 99 MHz and 276 MHz are the beats between the ECDL and spectrally-nearby Yb:fibre modes. Inset is the Fourier transform of the time-domain data sampled over 4.1 μs.

loop to maintain stability. A feed-forward locking system based on an acoustooptic modulator changing the frequency of the comb light was then attempted. Due to the angular change inherent to acoustooptic modulation of the laser light it was unfeasible due to the spatial mismatch of the two beams. Finally a direct method of control over the intracavity optical frequency was implemented: control of the angle of the intracavity filter by use of a galvanometer motor.

The galvanometer motor chosen had a change of 0.98° per Volt, which would allow for a great deal of intracavity change with very little applied voltage. In order to drive the motor a feedback loop was constructed (Figure 4.21) using the 20-dB beat signal from the monochromator. The heterodyne signal was filtered with a 200-MHz low-pass filter to remove the second beat signal and f_{rep} and, thus, to ensure visibility of only one peak. It was then amplified with a 40-dB, high-gain amplifier before passing into a digital oscilloscope and arbitrary waveform generator (TiePie Handyscope HS5), the oscilloscope operating with 12-bit acquisition at a sampling rate of 500 MS/s and the waveform generator at 14-bit depth. The acquired signal was then delivered to a PC for analysis. The program written to control the CEO beat performed a Fourier transform of the incoming waveform and elementary

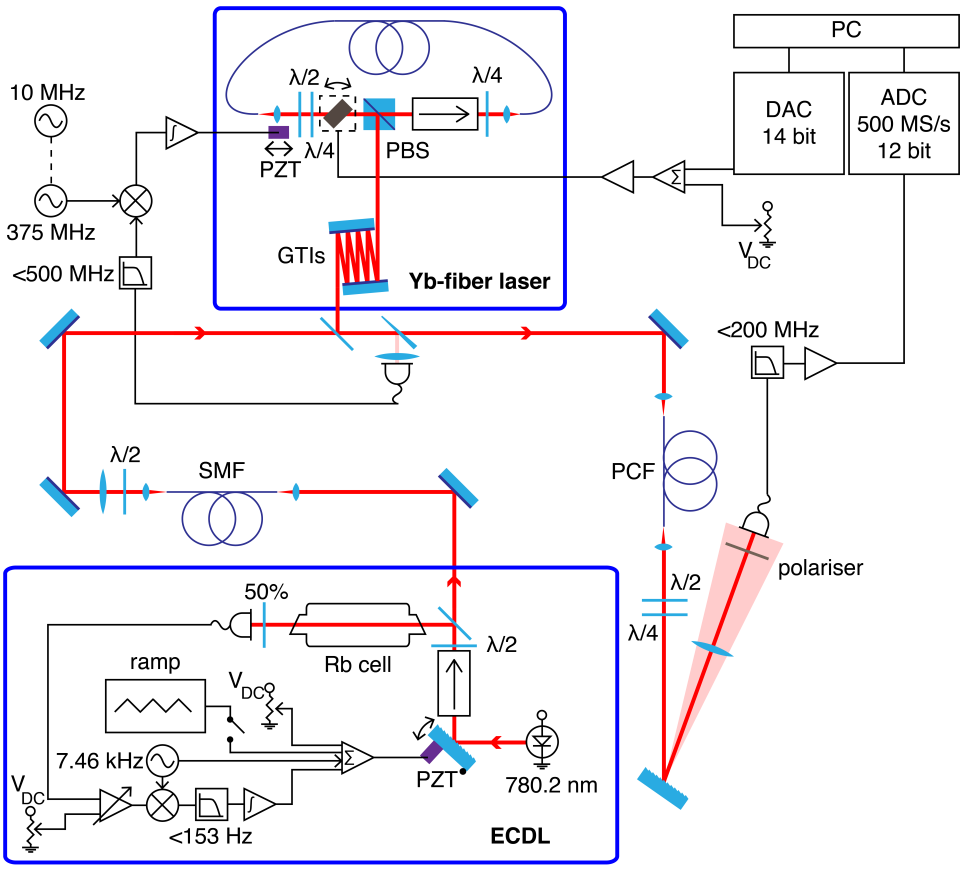

Figure 4.21: The beams from both the Yb:fibre laser and ECDL are made collinear, passed through a the PCF, and directed into the monochromator. The diffracted light is then imaged on to the active area of an avalanche photodetector. The signal is filtered and amplified before passing into an analogue-to-digital converter, into a PC for error control, and through a digital-to-analogue converter as output. It then passed through a summing amplifier with a DC-offset before passing through a further amplifier and driving the galvanometer motor.

peak detection. The peak was compared against a setpoint (75 MHz) to create an error signal which could be used for PID control of the intracavity filter. A flowchart showing the method of control is presented in Figure 4.22. The resultant correction voltage was passed through the arbitrary waveform generator (operating as a variable DC supply), through a summing amplifier with an added DC voltage to bring the galvanometer motor to the centre of its travel, through a further amplifier and to the motor.

The method was a success: f_{CEO} could be controlled and the laser continued to operate stably. Years of work had finally led to the achievement of the aims of the project. The long-term stability of the frequency can be seen in Figure 4.23, which shows the frequency fluctuations of the beat frequency relative to its mean.

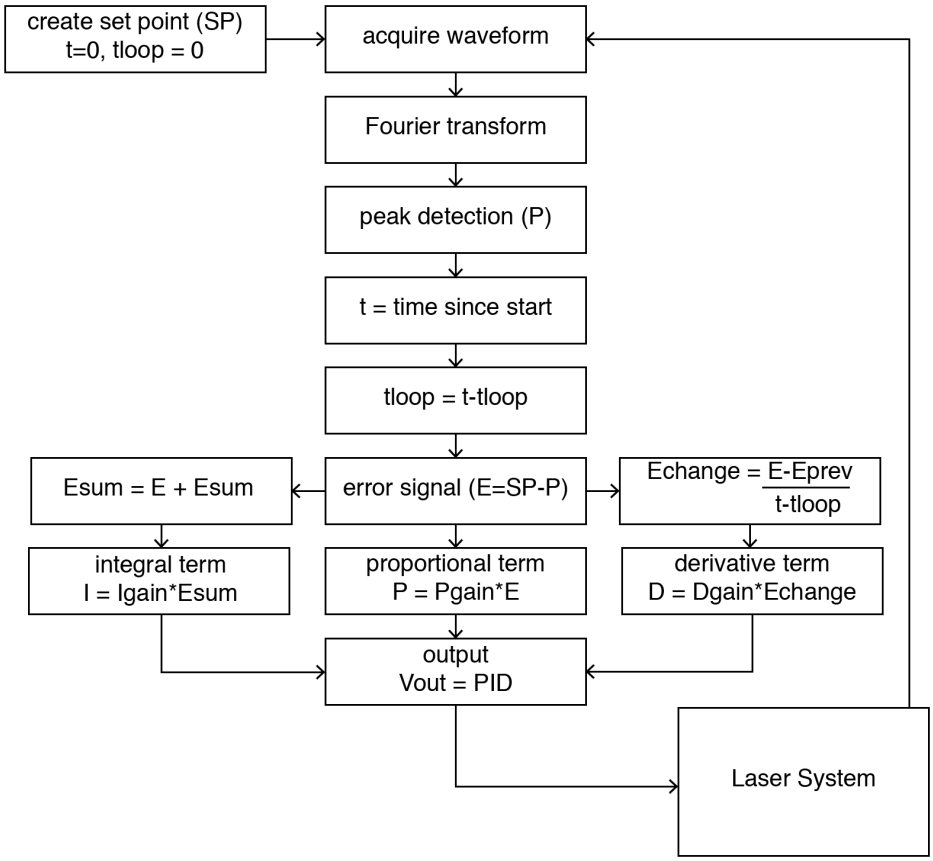

Figure 4.22: A flowchart detailing the steps taken by the beat-control program implemented through MatLab. An acquired waveform had a Fourier transform performed, the frequency at which the peak of the RF spectrum resides was measured (P), and further compared against a pre-defined setpoint (SP) to create an error signal (E). The time since the beginning of control was then recorded (t) and a following derivation of the loop time (tloop) performed. The error signal was then conditioned according to PID control: a proportional term, an integral term (summing up the error terms since the beginning of the loop), and a derivative term (showing the change in error signal between loops) were combined into a final output voltage applied to the galvanometer motor controlling the intracavity filter.

f_{rep} was locked for both measurements, and the comb-offset control was either off (blue) or on (green). The periodic nature of the change in the unlocked signal can be understood as temperature fluctuations in the lab due to the air-conditioning system that, when the locking loop was engaged, the comb offset could be held near a defined set point stably for at least 60 minutes. The RMS deviation of this measurement was 236 kHz and the Allan variance was 235 kHz. A table of the data for the different observations times can be seen in Table 4.4

Unfortunately this success came with a caveat: there was added noise from the control method. The system also had a hard limit of control due to the speed

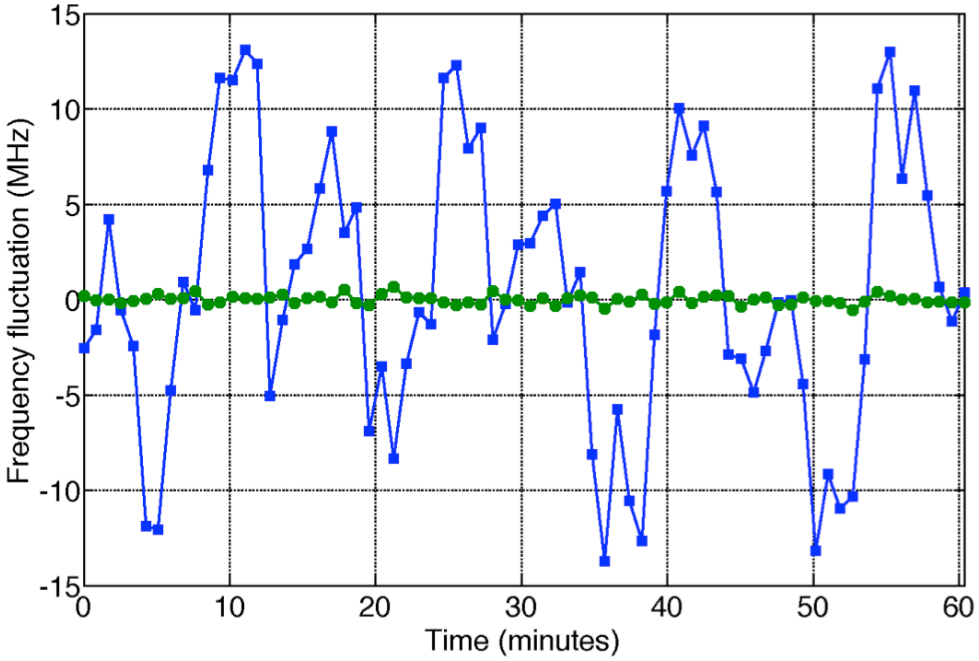

Figure 4.23: The long-term stability of the CEO-beat signal in terms of frequency fluctuations with regard to its mean. f_{rep} was locked for both, and the comb-offset control was either off (blue) or on (green). The periodicity of the unlocked signal is likely to be caused by the temperature changes in the lab associated with the air-conditioning cycle.

Gate Time	RMS unlocked	Allan var. unlocked	RMS locked	Allan var. locked
100 ms	7996.69 kHz	2282.06 kHz	3164.10 kHz	2490.35 kHz
200 ms	6989.91 kHz	1871.35 kHz	2102.27 kHz	1876.11 kHz
500 ms	5238.54 kHz	4241.78 kHz	2270.28 kHz	2157.32 kHz
1 s	1304.14 kHz	1015.26 kHz	1988.64 kHz	1938.25 kHz
2 s	1476.17 kHz	710.859 kHz	2012.59 kHz	2012.15 kHz
5 s	1771.79 kHz	775.969 kHz	1201.84 kHz	1227.09 kHz
10 s	3475.72 kHz	1383.43 kHz	989.765 kHz	911.961 kHz
20 s	4538.10 kHz	2023.69 kHz	646.148 kHz	575.724 kHz
50 s	7019.58 kHz	3856.72 kHz	441.273 kHz	264.254 kHz

Table 4.4: RMS deviation and Allan variance of comb-offset beat at differing observation times with the lock loop both on and off.

limitations of the software: the control loop had a bandwidth of 70 Hz.

4.7. Noise characterisation of the fully-stabilised comb

The stability of the lock signal was measured by counting the heterodyne beat frequency at increasing averaging times of 0.1, 0.2, 0.5, 1, 2, 5, 10, 20, and 50 seconds over many samples. In Figure 4.24 the calculated RMS deviation and Allan variance at each gate time can be seen. All data were acquired with f_{rep} stabilised

and locked, but comparing the locked and unlocked CEO-stabilisation.

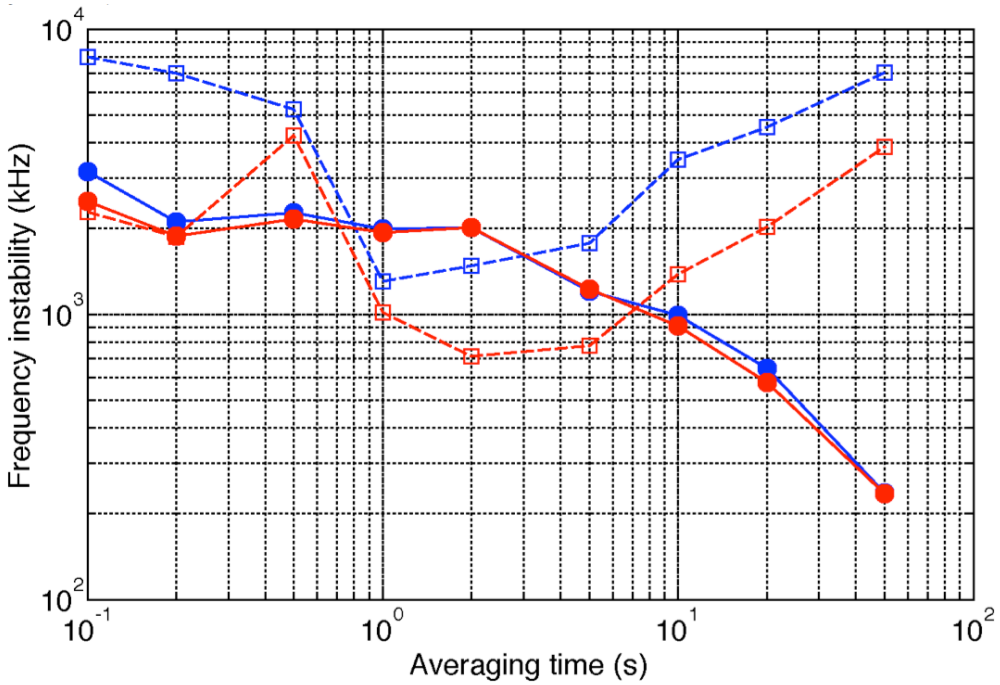

Figure 4.24: The RMS deviation (blue) and Allan variance (red) of the comb-offset beat signal with stabilisation both off (open markers) and on (filled markers). The unlocked minimum at centre is a result of the rapid-scale jitter of the control method. All data were recorded as Yb:fibre laser was repetition-rate stabilised.

The data show an expected drop in noise, thus better stability, at longer averaging times. Below 3 seconds the stability is lower, however, and this can be understood as an additive noise term created by 100-μrad variations in mains power applied to the galvanometer motor, which create a modulation of the beat signal (very visible at low observation times) with a frequency of 50 Hz. Due to the angular sensitivity of the galvanometer motor to voltage, these variations are amplified much more than might otherwise be necessary by using other methods. This noise will be minimised or eliminated entirely through the implementation of different tuning methods such as PZT, which require a greater voltage for angular change, and are therefore less susceptible to these noise terms.

4.8. Conclusions

I have presented a new method for stabilising the offset frequency of a Yb:fibre laser operating at 1030 nm by using an optical frequency standard at 780.2 nm. The locked system, using a galvanometer motor for intracavity filter control, exhibited

an Allan variance of 235 kHz for a 50-s averaging time and remained stably locked for >60 minutes with an RMS deviation of 236 kHz, corresponding to 3.9 mrad of f_{rep}. This stability is similar to the linewidth of the ECDL reference. The system was able to remain locked for long times due to the broad capture range and tunability of f_{CEO}, and while the control loop bandwidth was limited by the long loop times it could easily be improved for future work through the implementation of a hardware-based control system (such as a field-programmable gate array, or FPGA). Similarly, by replacing the galvanometer motor with a PZT the noise of the system is expected to decrease greatly.

Given more time the fibre laser's low pulse repetition frequency – relative to those of the two Yb:KYW lasers – could have been surmounted through spectral filtering of the intracavity modes. This would have had the knock-on effect of decreasing peak laser power, though, and would have required a greater laser output or amplification. Furthermore, greater pump power could have led to a spectrally-coherent supercontinuum, allowing for $f - 2f$ comparison and further stabilisation to the Rb standard.

5. Conclusions

This chapter first reviews the highlights and key findings from the experimental work undertaken and presented in this thesis and the conclusions regarding the results gathered from that work. I will then discuss the promise of the Yb^{3+}-based laser systems presented in this thesis for future frequency comb applications, analysing the successes of the Yb^{3+}:fibre system stabilised to the ^{87}Rb-referenced ECDL, and providing a discussion of future work expected to lead to further performance improvements. I will also discuss the viability of Yb^{3+} sources for frequency comb generation.

5.1. Experimental results and conclusions

In Chapter 2 work on a 1-GHz Yb^{3+}:$KY(WO_4)_2$ laser was presented, demonstrating the design, construction, and characteristics of the system. The spectral bandwidth of the mode-locked system was measured to be 3.8 nm, the pulse duration was 278 fs, and the average output power was 770 mW, corresponding to an optical-to-optical efficiency of 61% and a slope efficiency of 67%. This efficiency was the highest efficiency seen for Yb:KYW lasers up to that point. The noise characteristics were acquired using a relative intensity noise measurement showing a fluctuation of less than 1% at observation times above 1 second.

Efforts were made to broaden the pulsed light to span an octave for self-referenced comb stabilisation, but broadening via a PCF proved to be insufficient as a bandwidth of only 400 nm was possible.

Chapter 3 chronicled the continuation of work on Yb:KYW systems at a reduced pulse repetition frequency of 666 MHz, chosen in an attempt to increase the peak pulse power by 50% thereby enabling a broader supercontinuum. This new system had an average power of 750 mW and a spectral bandwidth of 5 nm, the latter due to the greater self-phase modulation in this higher-peak-power system. The pulse

duration from this system was also shorter, as expected, at 215 fs. As the system was shown to be an improvement in terms of power over its predecessor, work to lock the pulse repetition frequency was undertaken.

The locking loop worked, and a series of RIN measurements were taken to characterise the noise of this new system. A large series of sub-200-Hz noise spikes were seen, indicating a strong dependence on ambient factors. Isolation with respect to temperature and air currents proved to immediately lower the noise floor, but spikes were still present where they had been, leading to a revelation regarding the vibrational qualities of the cantilever arms used in the construction of the Yb:KYW laser. By damping the fundamental vibrational mode with a mass placed at the centre of the cantilever the lowest-possible vibrational mode was one with a node at the mirror-end of the cantilever. This modification led to a substantial improvement, however the long-term stability of the repetition frequency locking loop proved to be insufficient for frequency comb use.

Finally, in Chapter 4 a move to Yb:fibre lasers was made due to the stability and broad bandwidth of these systems. Work on characterising the system and compressing the laser output pulses was presented. Measurements of the laser pulse durations with regard to the extracavity GDD were made, and an optimal operating point of -18000 fs^2 was found. The pulses at their shortest were 123 fs with an average power after the compression system of 580 mW. Steps to lock the pulse repetition frequency of this system were taken, and due to the robust optomechanical nature of the Yb:fibre laser, locking was found to be very stable, with an instability of only 3.3×10^{-11} over 50 seconds.

The procedures to stabilise the Yb:fibre laser comb modes using a ^{87}Rb-locked external reference laser were then discussed. The design and construction of the ^{87}Rb-referenced ECDL were introduced before describing the supercontinuum generation obtained using the laser. Due to issues of spectral coherence in the broadened signal f-2f referencing proved to be impossible, and so a direct reference to the 780.2-nm Rb standard was pursued. By collinearising the Yb:fibre supercontinuum and the Rb-ECDL output a heterodyne beat signal was acquired via a monochromator

and sidebands were seen. Using a digital, computer-interfaced oscilloscope it was possible to control this beat frequency by use of a galvanometer motor coupled to the intracavity filter.

Noise characteristics of this locked system were analysed over varying observation times from 100 ms to 50 s. It was found that the RMS deviation of this CEO-frequency stabilised system was 236 kHz and the Allan deviation was 235 kHz with a locking loop that remained in-lock for longer than an hour.

5.2. Future developments for Yb^{3+}-doped laser systems

The chief difficulties in fully utilising Yb^{3+}-based lasers arose from pulse durations just slightly too long and peak powers just too low to allow for spectrally-coherent octave-spanning supercontinua to be obtained. This can, and has, been circumvented through the implementation of a direct frequency reference to an absolute optical standard in the form of ^{87}Rb, a method that not only eschews the complexity of an f-2f system, but also the size of the overall apparatus. This may be alleviated soon as pump diodes improve, higher pumping powers will lead to greater output powers and, thus, pulse durations short enough and optical spectra broad enough to allow for coherent supercontinuum generation. There are also myriad issues in a high-repetition-rate free-space system in general: increased sensitivity to pulse repetition frequency change, spacing to include all of the optics necessary for stable mode-locked laser generation, and decreased peak power. The first is mitigated by effective locking systems, while the second can be improved by using small-scale optomechanics, and the third through more effective pumping.

Further noise terms arose during repetition-rate locking through the home-built amplifier, though many were mitigated through environmental shielding and the inclusion of components intended to reduce noise through filtering. Other terms arose due to the large connection loops created in the lab acting as antennae, though these were improved over time as noise sources were identified one by one.

The Yb^{3+}:fibre laser was found to be the most promising for referenced comb generation. The broad spectrum and ability for very short pulse durations to be obtained after compression make it a good candidate for supercontinuum generation,

though the need for post-laser compression adds a level of complexity unnecessary in using Yb^{3+}:$KY(WO_4)_2$ lasers. Furthermore, all is not lost for Yb^{3+}:$KY(WO_4)_2$ systems: there is still a need for femtosecond laser sources in the 1-μm range for applications as diverse as hydrocarbon spectroscopy, micromachining, and astronomy, and the possibility for short pulse generation – possibly mediated by external cavity pulse compression [92] – from lasers bearing repetition rates impossible to achieve in a fibre laser without having to attempt the noise-inducing high-harmonic mode locking is too promising to ignore.

Bibliography

[1] T. W. Hänsch, "Nobel Lecture: Passion for precision," *Reviews of Modern Physics*, vol. 78, pp. 1297–1309, Nov. 2006.

[2] R. W. Fox, S. A. Diddams, A. Bartels, and L. W. Hollberg, "Optical frequency measurements with the global positioning system: tests with an iodine-stabilized He-Ne laser.," *Applied Optics*, vol. 44, pp. 113–120, Jan. 2005.

[3] N. V. Kuleshov, A. A. Lagatsky, V. G. Shcherbitsky, V. P. Mikhailov, E. Heumann, T. Jensen, A. Diening, and G. Huber, "CW laser performance of Yb and Er, Yb doped tungstates," *Applied Physics B: Lasers and Optics*, vol. 64, no. 4, pp. 409–413, 1997.

[4] T. P. Lamour, L. Kornaszewski, J. H. Sun, and D. T. Reid, "Yb:fiber-laser-pumped high-energy picosecond optical parametric oscillator," *Optics Express*, vol. 17, no. 16, pp. 14229–14234, 2009.

[5] S. Pekarek, C. Fiebig, M. C. Stumpf, A. E. H. Oehler, K. Paschke, G. Erbert, T. Südmeyer, and U. Keller, "Diode-pumped gigahertz femtosecond Yb:KGW laser with a peak power of 3.9 kW," *Optics Express*, vol. 18, pp. 16320–16326, July 2010.

[6] A. A. Lagatsky, F. Fusari, S. Calvez, V. E. Kisel, N. V. Kuleshov, C. T. A. Brown, M. D. Dawson, and W. Sibbett, "Passive mode locking of a Tm,Ho:$KY(WO_4)_2$ laser around 2 m," *Optics Letters*, vol. 34, pp. 2587–2589, Aug. 2009.

[7] L.-J. Chen, A. J. Benedick, J. R. Birge, M. Y. Sander, and F. X. Kärtner, "Octave-spanning, dual-output 2.166 GHz Ti:sapphire laser," *Optics Express*, vol. 16, pp. 20699–20705, Nov. 2008.

[8] A. Bartels, D. C. Heinecke, and S. A. Diddams, "Passively mode-locked 10 GHz femtosecond Ti:sapphire laser," *Optics Letters*, vol. 33, pp. 1905–1907, Aug. 2008.

[9] G. H. C. New, "The generation of ultrashort laser pulses," *Reports on Progress in Physics*, vol. 46, pp. 877–971, 1983.

[10] A. E. Siegman, *Lasers*. Mill Valley, CA: University Science Books, 1986.

[11] J. M. Dudley and J. R. Taylor, *Supercontinuum generation in optical fibers*. Cambridge: Cambridge University Press, 2010.

[12] I. Newton, *Opticks: or a treatise of the reflections, refractions, inflections and colours of light*. Prince's-Arms in St. Paul's Church-Yard, London: W. and J. Innys, printers to the Royal Society, 1718.

[13] J. Lægsgaard, "Mode profile dispersion in the generalised nonlinear Schrödinger equation," *Optics Express*, vol. 15, no. 24, pp. 16110–16123, 2007.

[14] J. M. Dudley, G. Genty, and S. Coen, "Supercontinuum generation in photonic crystal fiber," *Reviews of Modern Physics*, vol. 78, pp. 1135–1184, Oct. 2006.

[15] R. Thomson, C. Leburn, and D. T. Reid, *Ultrafast Nonlinear Optics*. Scottish Graduate Series, Springer, 2013.

[16] K. W. DeLong, R. Trebino, J. Hunter, and W. E. White, "Frequency-resolved optical gating with the use of second-harmonic generation," *Journal of the Optical Society of America B*, vol. 11, pp. 2206–2215, Nov. 1994.

[17] C. Iaconis and I. A. Walmsley, "Self-referencing spectral interferometry for measuring ultrashort optical pulses," *IEEE Journal of Quantum Electronics*, vol. 35, pp. 1–9, Mar. 1999.

[18] D. W. Allan, "Statistics of atomic frequency standards," *Proceedings of the IEEE*, vol. 54, no. 2, pp. 221–230, 1966.

[19] P. F. Moulton, "Spectroscopic and laser characteristics of Ti:Al_2O_3," *Journal of the Optical Society of America B*, vol. 3, pp. 125–138, Sept. 2002.

[20] P. Albers, E. Stark, and G. Huber, "Continuous-wave laser operation and quantum efficiency of titanium-doped sapphire," *Journal of the Optical Society of America B*, vol. 3, no. 1, pp. 134–139, 1986.

[21] P. Brockman, C. H. Bair, J. C. Barnes, R. V. Hess, and E. V. Browell, "Pulsed injection control of a titanium-doped sapphire laser," *Optics Letters*, vol. 11, pp. 712–714, Nov. 1986.

[22] U. Keller, W. H. Knox, and H. Roskos, "Coupled-cavity resonant passive mode-locked Ti:sapphire laser," *Optics Letters*, vol. 15, pp. 1377–1379, Dec. 1990.

[23] D. E. Spence, P. N. Kean, and W. Sibbett, "60-fsec pulse generation from a self-mode-locked Ti:sapphire laser," *Optics Letters*, vol. 16, pp. 42–44, Jan. 1991.

[24] C. Spielmann, F. Krausz, T. Brabec, E. Wintner, and A. J. Schmidt, "Femtosecond pulse generation from a synchronously pumped Ti:sapphire laser," *Optics Letters*, vol. 16, pp. 1180–1182, Aug. 1991.

[25] D. E. Spence, J. M. Evans, W. E. Sleat, and W. Sibbett, "Regeneratively initiated self-mode-locked Ti:sapphire laser," *Optics Letters*, vol. 16, pp. 1762–1764, Nov. 1991.

[26] T. Brabec, C. Spielmann, P. F. Curley, and F. Krausz, "Kerr lens mode locking," *Optics Letters*, vol. 17, pp. 1292–1294, Sept. 1992.

[27] M. T. Asaki, C.-P. Huang, D. Garvey, J. Zhou, H. C. Kapteyn, and M. M. Murnane, "Generation of 11-fs pulses from a self-mode-locked Ti:sapphire laser," *Optics Letters*, vol. 18, pp. 1–3, June 1993.

[28] J. F. Pinto, L. Esterowitz, G. H. Rosenblatt, M. Kokta, and D. Peressini, "Improved Ti:sapphire laser performance with new high figure of merit crystals," *IEEE Journal of Quantum Electronics*, vol. 30, no. 11, pp. 2612–2616, 1994.

[29] A. Stingl, R. Szipőcs, M. Lenzner, C. Spielmann, and F. Krausz, "Sub-10-fs mirror-dispersion-controlled Ti:sapphire laser," *Optics Letters*, vol. 20, no. 6, pp. 602–604, 1995.

[30] G. N. Gibson, B. E. Bouma, R. Klank, and F. Gibson, "Electro-optically cavity-dumped ultrashort-pulse Ti:sapphire oscillator," *Optics Letters*, vol. 21, no. 14, pp. 1055–1057, 1996.

[31] S. H. Cho, B. E. Bouma, E. P. Ippen, and J. G. Fujimoto, "Low-repetition-rate high-peak-power Kerr-lens mode-locked $TiAl_2O_3$ laser with a multiple-pass cavity," *Optics Letters*, vol. 24, no. 6, pp. 417–419, 1999.

[32] T. Udem, J. Reichert, R. Holzwarth, and T. W. Hänsch, "Absolute optical frequency measurement of the Cesium D_1 line with a mode-locked laser," *Physical Review Letters*, vol. 82, pp. 3568–3571, May 1999.

[33] T. Udem, J. Reichert, R. Holzwarth, and T. W. Hänsch, "Accurate measurement of large optical frequency differences with a mode-locked laser," *Optics Letters*, vol. 24, pp. 881–883, July 1999.

[34] S. A. Diddams, D. J. Jones, L.-S. Ma, S. T. Cundiff, and J. L. Hall, "Optical frequency measurement across a 104-THz gap with a femtosecond laser frequency comb," *Optics Letters*, vol. 25, pp. 186–188, Feb. 2000.

[35] D. J. Jones, S. A. Diddams, J. K. Ranka, A. Stentz, R. S. Windeler, J. L. Hall, and S. T. Cundiff, "Carrier-envelope phase control of femtosecond mode-locked lasers and direct optical frequency synthesis," *Science*, vol. 288, pp. 635–639, Apr. 2000.

[36] R. Holzwarth, T. Udem, T. W. Hänsch, J. C. Knight, S. Wada, and P. S. J. Russell, "Optical frequency synthesizer for precision spectroscopy," *Physical Review Letters*, vol. 85, pp. 2264–2267, Sept. 2000.

[37] T. M. Fortier, D. J. Jones, J. Ye, S. T. Cundiff, and R. S. Windeler, "Long-term carrier-envelope phase coherence," *Optics Letters*, vol. 27, pp. 1436–1438, Aug. 2002.

[38] T. M. Fortier, D. J. Jones, J. Ye, and S. T. Cundiff, "Highly phase stable mode-locked lasers," *IEEE Journal of Selected Topics in Quantum Electronics*, vol. 9, pp. 1002–1010, July 2003.

[39] L. Matos, D. Kleppner, O. Kuzucu, T. R. Schibli, J. Kim, E. P. Ippen, and F. X. Kaertner, "Direct frequency comb generation from an octave-spanning, prismless Ti:sapphire laser," *Optics Letters*, vol. 29, pp. 1683–1685, July 2004.

[40] T. M. Fortier, Y. Le Coq, J. E. Stalnaker, D. Ortega, S. A. Diddams, C. W. Oates, and L. W. Hollberg, "Kilohertz-resolution spectroscopy of cold atoms with an optical frequency comb," *Physical Review Letters*, vol. 97, pp. 1–4, Oct. 2006.

[41] I. Matsushima, H. Yashiro, and T. Tomie, "10 kHz 40 W Ti:sapphire regenerative ring amplifier," *Optics Letters*, vol. 31, no. 13, pp. 2066–2068, 2006.

[42] J. H. Sun, B. J. S. Gale, and D. T. Reid, "Coherent synthesis using carrier-envelope phase-controlled pulses from a dual-color femtosecond optical parametric oscillator," *Optics Letters*, vol. 32, pp. 1396–1398, Apr. 2007.

[43] J. H. Sun, B. J. S. Gale, and D. T. Reid, "Composite frequency comb spanning 0.4-2.4 μm from a phase-controlled femtosecond Ti:sapphire laser and synchronously pumped optical parametric oscillator," *Optics Letters*, vol. 32, pp. 1414–1416, Apr. 2007.

[44] A. Bartels, R. Gebs, M. S. Kirchner, and S. A. Diddams, "Spectrally resolved optical frequency comb from a self-referenced 5 GHz femtosecond laser," *Optics Letters*, vol. 32, pp. 2553–2555, Aug. 2007.

[45] G. T. Nogueira, B. Xu, Y. Coello, M. Dantus, and F. C. Cruz, "Broadband 2.12 GHz Ti:sapphire laser compressed to 5.9 femtoseconds using MIIPS," *Optics Express*, vol. 16, no. 14, pp. 10033–10038, 2008.

[46] A. Bartels, D. C. Heinecke, and S. A. Diddams, "Passively mode-locked 10 GHz femtosecond Ti:sapphire laser," *Optics Letters*, vol. 33, no. 16, pp. 1905–1907, 2008.

[47] P. W. Roth, A. J. Maclean, D. Burns, and A. J. Kemp, "Directly diode-laser-pumped Ti:sapphire laser," *Optics Letters*, vol. 34, no. 21, pp. 3334–3336, 2009.

[48] P. W. Roth, A. J. Maclean, D. Burns, and A. J. Kemp, "Direct diode-laser pumping of a mode-locked Ti:sapphire laser," *Optics Letters*, vol. 36, no. 2, pp. 304–306, 2011.

[49] Y. Romanyuk, *Liquid-phase epitaxy of doped KY(WO$_4$)$_2$ lasers for waveguide lasers*. PhD thesis, École Polytechnique Fédérale de Lausanne, Lausanne, Switzerland, 2006.

[50] N. V. Kuleshov, A. A. Lagatsky, A. V. Podlipensky, V. P. Mikhailov, and G. Huber, "Pulsed laser operation of Yb-doped KY(WO$_4$)$_2$ and KGd(WO$_4$)$_2$," *Optics Letters*, vol. 22, pp. 1317–1319, Sept. 1997.

[51] P. Lacovara, H. K. Choi, C. A. Wang, R. L. Aggarwal, and T. Y. Fan, "Room-temperature diode-pumped Yb:YAG laser," *Optics Letters*, vol. 16, pp. 1069–1071, July 1991.

[52] X. Mateos, R. Solé, J. Gavaldà, M. Aguiló, J. Massons, and F. Diaz, "Crystal growth, optical and spectroscopic characterisation of monoclinic KY(WO$_4$)$_2$ co-doped with Er^{3+} and Yb^{3+}," *Optical Materials*, vol. 28, pp. 423–431, June 2006.

[53] M. C. Pujol, M. A. Bursukova, F. F. Güell, X. Mateos, R. Solé, J. Gavaldà, M. Aguiló, J. Massons, F. Diaz, P. Klopp, U. Griebner, and V. Petrov, "Growth, optical characterization, and laser operation of a stoichiometric crystal KYb(WO$_4$)$_2$," *Physical Review B*, vol. 65, pp. 1–11, Apr. 2002.

[54] G. Wang and Z. Luo, "Crystal growth of KY(WO$_4$)$_2$: Er^{3+}, Yb^{3+}," *Journal of Crystal Growth*, vol. 116, pp. 505–506, Feb. 1992.

[55] A. S. Kumaran, A. L. Chandru, S. M. Babu, and M. Ichimura, "Growth and characterization of pure and doped KY(WO$_4$)$_2$ crystals," *Journal of Crystal Growth*, vol. 275, pp. e1901–e1905, Feb. 2005.

[56] Sangeeta, D. G. Desai, A. K. Singh, and S. C. Sabharwal, "Growth and characterization of $KY(WO_4)_2$ crystals," *Journal of Crystal Growth*, vol. 310, pp. 2815–2819, May 2008.

[57] A. S. Kumaran, S. M. Babu, S. Ganesamoorthy, I. Bhaumik, and A. K. Karnal, "Crystal growth and characterization of $KY(WO_4)_2$ and $KGd(WO_4)_2$ for laser applications," *Journal of Crystal Growth*, vol. 292, pp. 368–372, July 2006.

[58] H.-H. Liu, J. Nees, and G. Mourou, "Diode-pumped Kerr-lens mode-locked Yb:$KY(WO_4)_2$ laser," *Optics Letters*, vol. 26, pp. 1723–1725, Nov. 2001.

[59] A. A. Lagatsky, N. V. Kuleshov, and V. P. Mikhailov, "Diode-pumped CW lasing of Yb:KYW and Yb:KGW," *Optics Communications*, vol. 165, pp. 71–75, July 1999.

[60] P. Klopp, V. Petrov, U. Griebner, and G. Erbert, "Passively mode-locked Yb:KYW laser pumped by a tapered diode laser," *Optics Express*, vol. 10, pp. 108–113, Jan. 2002.

[61] F. Brunner, T. Südmeyer, E. Innerhofer, F. Morier-Genoud, R. Paschotta, V. E. Kisel, V. G. Shcherbitsky, N. V. Kuleshov, J. Gao, K. Contag, A. Giesen, and U. Keller, "240-fs pulses with 22-W average power from a mode-locked thin-disk Yb:$KY(WO_4)_2$ laser," *Optics Letters*, vol. 27, pp. 1162–1164, July 2002.

[62] A. S. Grabtchikov, A. N. Kuzmin, V. A. Lisinetskii, V. A. Orlovich, A. A. Demidovich, M. B. Danailov, H. J. Eichler, A. Bednarkiewicz, W. Strek, and A. N. Titov, "Laser operation and Raman self-frequency conversion in Yb:KYW microchip laser," *Applied Physics B: Lasers and Optics*, vol. 75, pp. 795–797, Nov. 2002.

[63] A. A. Lagatsky, E. U. Rafailov, C. G. Leburn, C. T. A. Brown, N. Xiang, O. G. Okhotnikov, and W. Sibbett, "Highly efficient femtosecond Yb:KYW laser pumped by single narrow-stripe laser diode," *Electronics Letters*, vol. 39, pp. 1108–1110, July 2003.

[64] A. A. Lagatsky, C. T. A. Brown, and W. Sibbett, "Highly efficient and low threshold diode-pumped Kerr-lens mode-locked Yb:KYW laser," *Optics Express*, vol. 12, pp. 3928–3933, Aug. 2004.

[65] G. Paunescu, J. Hein, and R. Sauerbrey, "100-fs diode-pumped Yb:KGW mode-locked laser," *Applied Physics B: Lasers and Optics*, vol. 79, pp. 555–558, June 2004.

[66] A. Aznar, R. Solé, M. Aguiló, F. Diaz, U. Griebner, R. Grunwald, and V. Petrov, "Growth, optical characterization, and laser operation of epitaxial Yb:$KY(WO_4)_2$/ $KY(WO_4)_2$ composites with monoclinic structure," *Applied Physics Letters*, vol. 85, pp. 4313–4315, Nov. 2004.

[67] A. Killi, A. Steinmann, J. Dörring, U. Morgner, M. J. Lederer, D. Kopf, and C. Fallnich, "High-peak-power pulses from a cavity-dumped Yb:$KY(WO_4)_2$ oscillator," *Optics Letters*, vol. 30, pp. 1891–1893, July 2005.

[68] M. Hildebrandt, U. Bünting, U. Kosch, D. Haussmann, T. Levy, M. Krause, O. Müller, U. Bartuch, and W. Viöl, "Diode-pumped Yb:KYW thin-disk laser operation with wavelength tuning to small quantum defects," *Optics Communications*, vol. 259, no. 2, pp. 796–798, 2006.

[69] A. A. Lagatsky, A. M. Malyarevich, V. G. Savitski, M. S. Gaponenko, K. V. Yumashev, A. A. Zhilin, C. T. A. Brown, and W. Sibbett, "PbS quantum-dot-doped glass for efficient passive mode locking in a cw Yb:KYW laser," *IEEE Photonics Technology Letters*, vol. 18, pp. 259–261, Jan. 2006.

[70] M. Jacquemet, F. Druon, F. Balembois, and P. Georges, "Single-frequency operation of diode-pumped Yb:KYW at 1003.4 nm and 501.7 nm by intracavity second harmonic generation," *Applied Physics B: Lasers and Optics*, vol. 85, pp. 69–72, May 2006.

[71] B. Jacobsson, J. E. Hellström, V. Pasiskevicius, and F. Laurell, "Widely tunable Yb:KYW laser with a volume Bragg grating," *Optics Express*, vol. 15, pp. 1003–1010, Jan. 2007.

[72] Y. Kalisky, O. Kalisky, U. Rachum, G. Boulon, and A. Brenier, "Comparative performance of passively q-switched diode-pumped Yb^{3+}-doped tungstate and garnet lasers using Cr^{4+}:YAG saturable absorber," *IEEE Journal of Selected Topics in Quantum Electronics*, vol. 13, pp. 502–510, May 2007.

[73] G. Palmer, M. Siegel, A. Steinmann, and U. Morgner, "Microjoule pulses from a passively mode-locked Yb:$KY(WO_4)_2$ thin-disk oscillator with cavity dumping," *Optics Letters*, vol. 32, pp. 1593–1595, June 2007.

[74] A. A. Lagatsky, F. M. Bain, C. T. A. Brown, W. Sibbett, D. A. Livshits, G. Erbert, and E. U. Rafailov, "Low-loss quantum-dot-based saturable absorber for efficient femtosecond pulse generation," *Applied Physics Letters*, vol. 91, p. 231111, Dec. 2007.

[75] S. A. Meyer, J. A. Squier, and S. A. Diddams, "Diode-pumped Yb:KYW femtosecond laser frequency comb with stabilized carrier-envelope offset frequency," *The European Physical Journal D*, vol. 48, pp. 19–26, Jan. 2008.

[76] S. Yamazoe, M. Katou, and T. Kasamatsu, "Ultra-compact laser-diode-pumped femtosecond solid-state laser," *Fujifilm Research and Development*, vol. 54, pp. 48–52, 2009.

[77] K. Seger, B. Jacobsson, V. Pasiskevicius, and F. Laurell, "Tunable Yb:KYW laser using a transversely chirped volume Bragg grating," *Optics Express*, vol. 17, pp. 2341–2347, Feb. 2009.

[78] P. Wasylczyk, P. Wnuk, and C. Radzewicz, "Passively modelocked, diode-pumped Yb:KYW femtosecond oscillator with 1 GHz repetition rate," *Optics Express*, vol. 17, pp. 5630–5635, Mar. 2009.

[79] P. Wasylczyk and C. Radzewicz, "Design and alignment criteria for a simple, robust, diode-pumped femtosecond Yb:KYW oscillator," *Laser Physics*, vol. 19, pp. 129–133, Aug. 2009.

[80] S. Pekarek, C. Fiebig, M. C. Stumpf, A. E. H. Oehler, K. Paschke, G. Erbert, T. Südmeyer, and U. Keller, "First SESAM-Modelocked Yb:KGW Femtosec-

ond Oscillator Operating at 1 GHz Repetition Rate," in *Conference on Lasers and Electro-Optics/Quantum Electronics and Laser Science Conference*, pp. 1–4, Department of Physics, Institute of Quantum Electronics, ETH Zurich, 8093 Zurich, Switzerland, 2010.

[81] M. Siegel, A. Guandalini, and J. Aus der Au, "High repetition rate cavity-dumped Yb:KYW femtosecond oscillator," in *Conference on Lasers and Electro-Optics/Quantum Electronics and Laser Science Conference*, High Q Laser Innovation GmbH, Feldgut 9, 6830 Rankweil, Austria, 2010.

[82] S. Yamazoe, M. Katou, T. Adachi, and T. Kasamatsu, "Palm-top-size, 1.5 kW peak-power, and femtosecond (160 fs) diode-pumped mode-locked Yb^{3+}:$KY(WO_4)_2$ solid-state laser with a semiconductor saturable absorber mirror," *Optics Letters*, vol. 35, pp. 748–750, Feb. 2010.

[83] G.-H. Kim, U. Kang, D. Heo, V. E. Yashin, A. V. Kulik, E. G. Sall, and S. A. Chizhov, "Femtosecond oscillator on Yb:KYW crystal pumped by laser diode with fiber output," *Optics and Spectroscopy*, vol. 108, pp. 819–823, May 2010.

[84] A. A. Demidovich, A. N. Kuzmin, G. I. Ryabtsev, M. B. Danailov, W. Strek, and A. N. Titov, "Influence of Yb concentration on Yb:KYW laser properties," *Journal of Alloys and Compounds*, vol. 300-301, pp. 238–241, Mar. 2000.

[85] A. A. Lagatsky, E. U. Rafailov, A. R. Sarmani, C. T. A. Brown, W. Sibbett, L. Ming, and P. G. R. Smith, "Efficient femtosecond green-light source with a diode-pumped mode-locked Yb^{3+}:$KY(WO_4)_2$ laser," *Optics Letters*, vol. 30, pp. 1144–1146, May 2005.

[86] J. E. Hellström, S. Bjurshagen, V. Pasiskevicius, J. Liu, V. Petrov, and U. Griebner, "Efficient Yb:KGW lasers end-pumped by high-power diode bars," *Applied Physics B: Lasers and Optics*, vol. 83, pp. 235–239, Mar. 2006.

[87] G. R. Holtom, "Mode-locked Yb:KGW laser longitudinally pumped by polarization-coupled diode bars," *Optics Letters*, vol. 31, pp. 2719–2721, Aug. 2006.

[88] A. A. Lagatsky, F. Bain, C. T. A. Brown, W. Sibbett, D. A. Livshits, G. Erbert, and E. U. Rafailov, "Diode-pumped femtosecond Yb:KYW laser incorporating a quantum-dot saturable absorber," in *Conference on Lasers and Electro-Optics/Quantum Electronics and Laser Science Conference*, pp. 1–2, J.F. Allen Physics Research Laboratories, School of Physics and Astronomy, University of St. Andrews, St. Andrews, KY16 9SS, Scotland, UK, 2008.

[89] W. W. Rigrod, "Laser Mirror Transmissivity Optimization in High Power Optical Cavities," *Applied Optics*, vol. 7, p. 2325, July 1968.

[90] T. C. Schratwieser, C. G. Leburn, and D. T. Reid, "Highly efficient 1 GHz repetition-frequency femtosecond Yb^{3+}:$KY(WO_4)_2$ laser," *Optics Letters*, vol. 37, pp. 1133–1135, Mar. 2012.

[91] W. H. Press, S. A. Teukolsky, W. T. Vetterling, and B. P. Flannery, *Numerical recipes*. Cambridge: Cambridge University Press, third ed., 2007.

[92] S. Pekarek, T. Südmeyer, S. Lecomte, S. Kundermann, J. M. Dudley, and U. Keller, "Self-referenceable frequency comb from a gigahertz diode-pumped solid-state laser," *Optics Express*, vol. 19, pp. 16491–16497, Aug. 2011.

[93] M. Hofer, M. H. Ober, F. Haberl, and M. E. Fermann, "Characterization of ultrashort pulse formation in passively mode-locked fiber lasers," *IEEE Journal of Quantum Electronics*, vol. 28, pp. 720–728, Mar. 1992.

[94] J. W. Arkwright, P. Elango, G. R. Atkins, T. Whitbread, and M. J. F. Digonnet, "Experimental and theoretical analysis of the resonant nonlinearity in Ytterbium-doped fiber," *Journal of Lightwave Technology*, vol. 16, pp. 798–806, May 1998.

[95] K. S. Abedin, J. T. Gopinath, L. A. Jiang, M. E. Grein, H. A. Haus, and E. P. Ippen, "Self-stabilized passive, harmonically mode-locked stretched-pulse erbium fiber ring laser," *Optics Letters*, vol. 27, pp. 1758–1760, Oct. 2002.

[96] J. Rauschenberger, T. Fortier, D. Jones, J. Ye, and S. T. Cundiff, "Control of the frequency comb from a mode-locked Erbium-doped fiber laser: Errata.," *Optics Express*, vol. 11, p. 1345, June 2003.

[97] O. G. Okhotnikov, L. A. Gomes, N. Xiang, T. Jouhti, and A. B. Grudinin, "Mode-locked ytterbium fiber laser tunable in the 980–1070-nm spectral range," *Optics Letters*, vol. 28, pp. 1–3, Sept. 2003.

[98] B. R. Washburn, S. A. Diddams, N. R. Newbury, J. W. Nicholson, M. F. Yan, and C. G. Jørgensen, "Phase-locked, erbium-fiber-laser-based frequency comb in the near infrared.," *Optics Letters*, vol. 29, pp. 250–252, Feb. 2004.

[99] L. Orsila, L. A. Gomes, N. Xiang, T. Jouhti, and O. G. Okhotnikov, "Mode-locked Ytterbium fiber lasers," *Applied Optics*, vol. 43, pp. 1902–1906, Mar. 2004.

[100] S. Zhou, D. G. Ouzounov, and F. W. Wise, "Passive harmonic mode-locking of a soliton Yb fiber laser at repetition rates to 1.5 GHz," *Optics Letters*, vol. 31, pp. 1–3, Jan. 2006.

[101] A. Chong, W. H. Renninger, and F. W. Wise, "All-normal-dispersion femtosecond fiber laser with pulse energy above 20 nJ," *Optics Letters*, vol. 32, pp. 2408–2410, Aug. 2007.

[102] P. Pal, W. H. Knox, I. Hartl, and M. E. Fermann, "Self referenced Yb-fiber-laser frequency comb using a dispersion micromanaged tapered holey fiber," *Optics Express*, vol. 15, pp. 12161–12166, Sept. 2007.

[103] I. Hartl, T. R. Schibli, A. Marcinkevicius, D. C. Yost, D. D. Hudson, M. E. Fermann, and J. Ye, "Cavity-enhanced similariton Yb-fiber laser frequency comb: $3x10^{14}W/cm^2$ peak intensity at 136 MHz," *Optics Letters*, vol. 32, pp. 2870–2872, Sept. 2007.

[104] S. Kivistö, R. Herda, and O. G. Okhotnikov, "Electronically tunable Yb-doped mode-locked fiber laser," *IEEE Photonics Technology Letters*, vol. 20, pp. 51–53, Jan. 2008.

[105] A. Chong, W. H. Renninger, and F. W. Wise, "Properties of normal-dispersion femtosecond fiber lasers," *Journal of the Optical Society of America B*, vol. 25, pp. 140–148, Feb. 2008.

[106] R. Herda and O. G. Okhotnikov, "Mode-locked Yb-doped fiber laser with external compression to 89 fs in normal dispersion fiber," *Applied Optics*, vol. 47, pp. 1182–1186, Mar. 2008.

[107] X. Zhou, D. Yoshitomi, Y. Kobayashi, and K. Torizuka, "Generation of 28-fs pulses from a mode-locked ytterbium fiber oscillator," *Optics Express*, vol. 16, pp. 7055–7059, May 2008.

[108] D. A. Braje, L. W. Hollberg, and S. A. Diddams, "Brillouin-enhanced hyperparametric generation of an optical frequency comb in a monolithic highly nonlinear fiber cavity pumped by a cw laser," *Physical Review Letters*, vol. 102, pp. 1–4, May 2009.

[109] M. Schultz, H. Karow, D. Wandt, U. Morgner, and D. Kracht, "Ytterbium femtosecond fiber laser without dispersion compensation tunable from 1015 nm to 1050 nm," *Optics Communications*, vol. 282, pp. 2567–2570, July 2009.

[110] T. Wilken, P. Vilar-Welter, T. W. Hänsch, T. Udem, T. Steinmetz, and R. Holzwarth, "High repetition rate, tunable femtosecond Yb-fiber laser," in *CLEO/QELS 2010*, pp. 1–2, Max-Planck-Institut für Quantenoptik, Hans Kopfermann Str. 1, 85748 Garching, Germany, Dec. 2009.

[111] Y.-J. Kim, Y. Kim, B. J. Chun, S. Hyun, and S.-W. Kim, "All-fiber-based optical frequency generation from an Er-doped fiber femtosecond laser," *Optics Express*, vol. 17, pp. 10939–10945, June 2009.

[112] G. Sobon, K. Krzempek, P. Kaczmarek, K. M. Abramski, and M. Nikodem, "10 GHz passive harmonic mode-locking in Er–Yb double-clad fiber laser," *Optics Communications*, vol. 284, pp. 4203–4206, Aug. 2011.

[113] D. C. Hanna, R. M. Percival, I. R. Perry, R. G. Smart, P. J. Suni, and A. C. Tropper, "An ytterbium-doped monomode fibre laser: broadly tunable opera-

tion from 1.010 μm to 1.162 μm and three-level operation at 974 nm," *Journal of Modern Optics*, vol. 37, no. 4, pp. 517–525, 1990.

[114] H. M. Pask, R. J. Carman, D. C. Hanna, A. C. Tropper, C. J. Mackechnie, P. R. Barber, and J. M. Dawes, "Ytterbium-doped silica fiber lasers: versatile sources for the 1-1.2 μm region," *IEEE Journal of Selected Topics in Quantum Electronics*, vol. 1, no. 1, pp. 2–13, 1995.

[115] Alhazen, *De Aspectibus*. None, ca. 1000 CE.

[116] R. Herda and O. G. Okhotnikov, "Dispersion compensation-free fiber laser mode-locked and stabilized by high-contrast saturable absorber mirror," *IEEE Journal of Quantum Electronics*, vol. 40, pp. 893–899, July 2004.

[117] A. Chong, J. R. Buckley, W. H. Renninger, and F. W. Wise, "All-normal-dispersion femtosecond fiber laser," *Optics Express*, vol. 14, pp. 10095–10100, Oct. 2006.

[118] C. Farrell, K. A. Serrels, T. R. Lundquist, P. Vedagarbha, and D. T. Reid, "Octave-spanning super-continuum from a silica photonic crystal fiber pumped by a 386 MHz Yb:fiber laser," *Optics Letters*, vol. 37, pp. 1778–1780, May 2012.

[119] J. Ye, S. Swartz, P. Jungner, and J. L. Hall, "Hyperfine structure and absolute frequency of the ^{87}Rb $5P_{3/2}$ state.," *Optics Letters*, vol. 21, pp. 1280–1282, Aug. 1996.